NONLINEAR BEAM MECHANICS

NONLINEAR BEAM MECHANICS

Proefschrift

ter verkrijging van de graad van doctor
aan de Technische Universiteit Delft,
op gezag van de Rector Magnificus prof. ir. K. C. A. M. Luyben,
voorzitter van het College voor Promoties,
in het openbaar te verdedigen op donderdag 8 november 2012 om 12:30 uur

door

Hidde Jelger Robbert WESTRA

natuurkundig ingenieur
geboren te Assen.

Dit proefschrift is goedgekeurd door de promotor:

Prof. dr. ir. H. S. J. van der Zant

Samenstelling promotiecommissie:

Rector Magnificus,	voorzitter
Prof. dr. ir. H. S. J. van der Zant,	Technische Universiteit Delft, promotor
Prof. dr. ir. H. W. Zandbergen	Technische Universiteit Delft
Prof. dr. ir. F. van Keulen,	Technische Universiteit Delft
Prof. dr. ir. J. W. M. Frenken,	Universiteit Leiden
Prof. dr. R. Lifshitz,	Tel Aviv University
dr. ir. P. G. Steeneken,	NXP Semiconductors
dr. ir. W. J. Venstra,	Technische Universiteit Delft

Dr. ir. W. .J. Venstra heeft als begeleider in belangrijke mate aan de totstandkoming van het proefschrift bijgedragen.

Keywords: MEMS, nonlinear dynamics, modal interactions, nanomechanical devices

Printed by: Gildeprint Drukkerijen - Enschede

Front & Back: Optical microscopy image of a series of cantilevers (photo by Charlotte Duynstee)

Casimir PhD Series, Delft-Leiden 2012-26

ISBN 978-90-8593-133-1

An electronic version of this dissertation is available at
http://repository.tudelft.nl/.

CONTENTS

1

INTRODUCTION

1

1.1 MICROMECHANICS

MECHANICS is one of the most intensively studied fields in physics and classical mechanics is a first-year course every physics student takes. The field is very broad, as everything around us is in motion, for example: a kid on a swing, the moon, quantum mechanics. In this Thesis, I focus on classical mechanics, where a rigid body deforms under the influence of a force. For the rigid body, I consider a simple geometric shape, a beam either clamped on two sides to a solid support (clamped-clamped) or just on one side (cantilever). The beam is allowed to deform and deflect under the influence of the force.

Following the trend to downscale electronic devices, mechanical devices are also entering the micro- and even nanometer regime [1]. To read out the motion of a mechanical device, for example a beam, it has to be coupled to an electronic circuit. These systems are the so-called micro-electromechanical systems (MEMS) and they find commercial application in accelerometers, gyroscopes, mass sensing, pressure sensing, band-pass filters and scanning probe microscopy. Downscaling these devices reduces cost and lowers energy consumption. The ultimate limit for downscaling is reached in nano-electromechanical devices (NEMS) consisting of carbon nanotubes or graphene sheets [2–4].

Figure 1.1 gives four examples of NEMS applications. One of these applications is mass sensing. In Fig. 1.1(a) a scanning electron micrograph (SEM) of clamped-clamped resonator beams is shown [5]. The material underneath the beams is completely etched away providing access from the bottom. With an inkjet printer, different polymers can be used to coat the backside of these beams. In this way they are functionalized, meaning that it has become sensitive to a certain substance. When the substance adheres to the polymer surface, effectively the added mass or change in stress results in a change in resonance frequency. This change in mass is measured as a change in resonance frequency of the beam. Resonance-based sensing is widely applied and recently has achieved the single-proton resolution [8]. The resonance frequency of the beam is mathematically described as: $f_0 = \sqrt{k/m_0}$, where k is the spring constant and m_0 is the mass of the resonator. The change in resonance frequency is related to the change in mass (assuming there is no change in the spring constant): $\Delta f = -(f_0/2m_0)\Delta m$ [9]. When the mass and resonance frequency of the resonator are known, the added mass can be calculated. By downscaling the beam, smaller masses can be detected as the prefactor f_0/m_0 increases. Starting with a smaller resonator mass allows smaller masses to be detected. Using carbon nanotubes as resonators, masses down to a yoctogram 10^{-24}g can be detected [8, 10, 11].

Another application of MEMS is in electrical circuits, where a mechanical oscillator is used as a clock [12]. Nowadays, most clocks in consumer electronics are

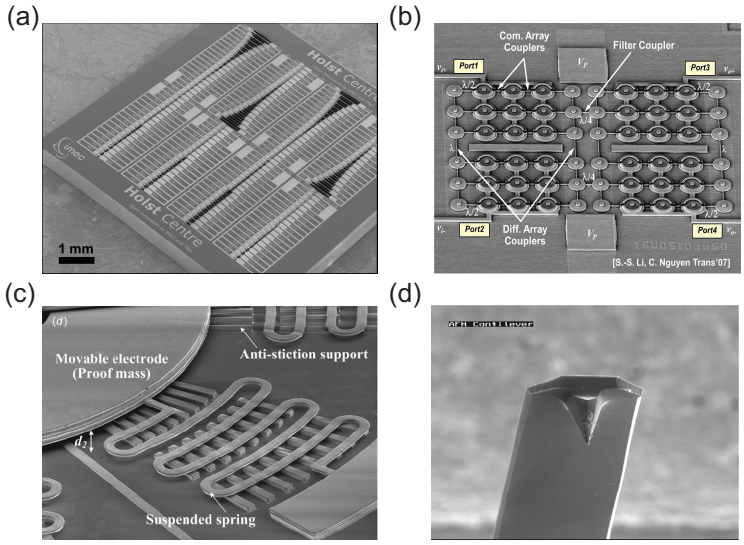

FIGURE 1.1: Scanning electron micrographs (SEMs) of four examples, where MEMS are used in applications. (a) Chip with an array of clamped-clamped beams with an integrated piezo-actuator used for gas sensing [5]. (b) Mechanical frequency filter consisting of 128 radial mode disks [6]. (c) Part of an accelerometer with a suspended proof mass connected via springs [7]. (d) AFM cantilever with a tip to scan surfaces.

made from quartz crystal oscillators, which are very stable and have high quality factors. A disadvantage of these crystals is that they are fairly big and with the continuous downscaling of electronics are relatively taking up more and more space. Moreover, quartz crystals cannot be integrated into CMOS. Since microprocessors need an appropriate time-keeping component a separate quartz crystal needs to be provided. One option to solve this problem is the use of MEMS as clocks [13]. However, until now the high phase noise noise of MEMS oscillators prohibits this. MEMS can also be used as analogue frequency filters [Fig. 1.1(b)], bit-storage (volatile and non-volatile) [14–16], idler frequency generation (sum or difference of two other frequencies) [17] and for logical operations [18]. This opens prospects for mechanical information processing, e.g. in situations where the device is operated in harsh conditions where electronics stop working due to dopant diffusion. For example by using silicon carbide MEMS higher operating temperature can be achieved [19].

Other practical applications involving MEMS are found in accelerometers and

gyroscopes [7, 20]. Figure 1.1(c) shows a part of such an accelerometer, where a proof mass is connected to a rigid wall via springs. The MEMS accelerometer measures the acceleration of a suspended proof mass by monitoring the capacitance between the proof mass and a rigid electrode. Using clever designs, the accelerometer can be sensitive to accelerations along three axes [21]. These MEMS accelerometers are found in, for example, airbag sensors and smart-phones [1].

The final application of MEMS I will discuss, is the Atomic Force Microscope (AFM). The AFM was invented by Binnig, Quate and Gerber in 1986 and is nowadays standard equipment in any nano-science laboratory [22]. The AFM is primarily used for surface imaging and force spectroscopy. The AFM consists of a mechanical element, a cantilever with a sharp tip at the end, see Fig. 1.1(d), and an optical detector to read out the cantilever displacement. For imaging, the tip is scanned across the surface and the displacement of the cantilever is measured. This displacement is a measure for the force between the tip and the sample. The AFM can be used in contact mode and in tapping mode. In contact mode the cantilever tip is in contact with the sample surface and the static displacement of the cantilever is measured. In tapping mode, the cantilever is weakly driven near its resonance frequency and the change in resonance frequency due to the force between the tip and sample is detected. Both methods can be used to image the surface topology of a sample. The AFM can also be used for force spectroscopy where the cantilever is pressed into the sample and a force-distance curve is measured, which for example can be used to measure the bending rigidity of graphene [23].

MEMS are used over a wide range of applications, each benefiting from the mechanics at the micro- and nanometer size. With technology progressing, it will be possible to integrate NEMS in our daily-used electronics. Whether it is as an electronic nose which can smell the smallest amount of drugs, or gyroscopes for consumer electronics, NEMS and MEMS will continue to contribute to technological innovations.

1.2 NONLINEAR DYNAMICS

Nonlinear behavior is typically avoided in MEMS applications as engineers in general prefer linear input-output relations that are easy to predict and control. However, in small-scale mechanics nonlinear behavior is omnipresent and enables new applications that cannot be achieved with linear systems. Nonlinearity enables new applications such as sensitive force measurements [**?**], stabilization of frequency and phase [24], storage and modification of digital information [16]. Moreover, nonlinearity gives ultimately limits the damping and couples the modes [25,

[1] See for example http://invensense.com/mems/handhelds.html

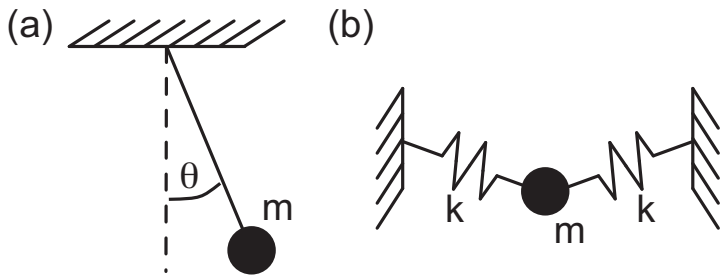

FIGURE 1.2: Examples of nonlinearities in mechanics. (a) A pendulum swinging under the influence of gravity. (b) A mass connected with two springs to two walls.

26], which can be used for new detector schemes that are potentially quantum limited. In order to understand these mechanisms, some knowledge about nonlinear dynamics is required.

Nonlinear dynamics is an interdisciplinary research field based on nonlinear differential or difference equations [27, 28]. There are many examples of nonlinear dynamics in mechanical systems [29]. One of the most illustrative is a pendulum, shown in Fig. 1.2(a). The pendulum with a mass m and length L moves under the influence of gravity. Its motion can be described by one coordinate, the angle with the vertical, θ. The equation of motion can be written as

$$\frac{\mathrm{d}^2\theta}{\mathrm{d}t^2} + \frac{g}{L}\sin(\theta) = 0, \tag{1.1}$$

where the local gravitational constant is g. This is a nonlinear differential equation, as the restoring force is nonlinear in the angle θ. The sine can be expanded around $\theta = 0$ using $\sin(\theta) = \theta - \frac{1}{6}\theta^3 + \ldots$. Inserting this into the equation of motion gives

$$\frac{\mathrm{d}^2\theta}{\mathrm{d}t^2} + \frac{g}{L}\theta - \frac{g}{6L}\theta^3 = 0. \tag{1.2}$$

The first two terms in this equation are linear in θ and the last term is the nonlinear part. For small amplitudes, the nonlinear terms can safely be ignored and the linear equation describes the motion of the pendulum. The linear equation results in a harmonic oscillations around $\theta = 0$. For large angles, the restoring force becomes smaller which is reflected by a cubic term in θ with a negative sign. The problem of the nonlinear pendulum can also be solved exactly. The angular frequency of the

pendulum now depends on the amplitude of the motion: at high amplitudes, the swinging frequency is smaller.

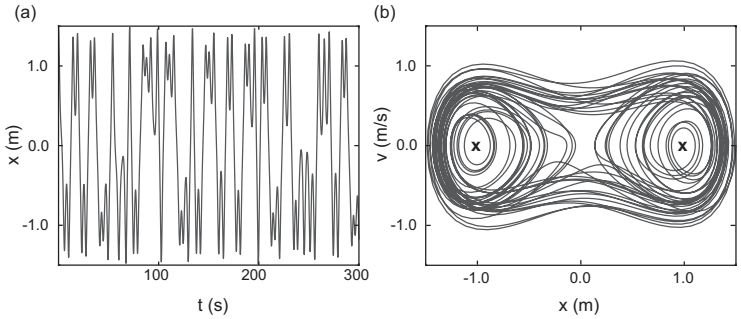

FIGURE 1.3: Simulation of the mass-spring system, with parameters $m = 1$kg, $k = 0.6$ N/m, $d = -1.0$ m, $L = 1.0$ m, $F = 0.25$ N, $b = 0.1$ kg/s and $\Omega = 1.1$ rad^{-1} Hz. (a) Position of the mass versus time. (b) Phase plot of the motion. The attractors are marked by a **x**.

Another example resembling the nonlinearities occurring in the dynamics of beams is a mass clamped to two walls via two identical springs as in Fig. 1.2(b). The potential energy of the mass is $V(x) = k(\sqrt{L^2 + x^2} - (L - d))^2$, where k is the spring constant, L is the un-stretched length of a spring and d the amount of stretching ($d > 0$) or compression ($d < 0$) of the spring when the mass is aligned horizontally with the springs. From the potential, the equation of motion can be derived using an approximation for the square root:

$$m\frac{\mathrm{d}^2x}{\mathrm{d}t^2} + 2kd\frac{x}{L} + k(L-d)\frac{x^3}{L^3} + \gamma\frac{\mathrm{d}x}{\mathrm{d}t} = F\sin(\Omega t). \tag{1.3}$$

A term is added to account for the damping of the system (damping rate γ) and an external driving force can be applied to the mass-spring system (drive force F at frequency Ω). If the springs are compressed when the springs are aligned along the horizontal, i.e. $d < 0$, the mass has two options: to move to a stable position above or underneath the horizontal. This phenomenon is called Euler-buckling [15, 30, 31] and a widely used large-scale example is the compression of a plastic teaspoon. At a critical pressure the teaspoon will buckle. The critical pressure at which this buckling occurs is called a bifurcation point. Before the critical point there is one stable solution, and after this point there are three solutions: two stable ($x = \pm 1$m) and one unstable ($x = 0$m) solution. Equation 1.3 can be solved numerically in the bistable regime ($b < d_{\mathrm{cr}} < 0$) and the result is shown in Fig. 1.3. We plot the distance from the horizontal x as a function of time and observe two stable amplitudes at

$x = 1$ and -1. There are switches between these amplitudes (Fig. 1.3(a)). If we plot the phase-diagram, the position and velocity on the axis we obtain Fig. 1.3(b). The stable points, where the mass is oscillating around are called the attractors of the system, indicated in Fig. 1.3(b) by the two crosses.

1.3 THESIS OUTLINE

This thesis deals with the nonlinear dynamics of clamped-clamped and single-clamped microbeams, which are elementary mechanical structures that form the building blocks of many top-down and bottom-up fabricated NEMS. The beams are fabricated from silicon or silicon nitride and their motion is detected using optical deflection, magnetomotive and piezo-electric readout schemes. **Chapter 2** presents the basic framework of nonlinear mechanics. We start with a description of the linear regime and proceed towards a description of modal interactions via the nonlinearity in clamped-clamped beams. The following chapters consist of published and submitted journal articles. The nonlinear dynamics of a cantilever is described in **Chapter 3**, showing mechanical stiffening and bifurcation. An example application is the implementation of a mechanical bit. In the bistable regime, noise can be used to switch from one stable amplitude to the other. In **Chapter 4**, this noise-induced switching in a microcantilever is discussed. Besides changing the oscillation of the mode itself, the oscillation of other modes is also affected. Such modal interactions are theoretically and experimentally studied in **Chapter 5** for the clamped-clamped beam and in **Chapter 6** for the cantilever. Although the nonlinearity has a different origin for the two cases, the resulting dynamic behavior is very similar. A consequence of the mode coupling is the ability to tune the Q factor of a microcantilever using two mechanical modes. A higher mode is used as a pump mode to tune the Q factor of the probe mode as is shown in **Chapter 7**. Finally, the interaction between a parametrically excited mode and a directly-driven mode of a clamped-clamped beam is investigated in **Chapter 8**.

REFERENCES

[1] K. L. Ekinci and M. L. Roukes, *Nanoectromechanical systems*, Rev. Sci. Instrum. **76**, 061101 (2005).

[2] S. Sapmaz, Y. M. Blanter, L. Gurevich, and H. S. J. .van der Zant, *Carbon nanotubes as nanoelectromechanical systems*, Phys. Rev. B **67**, 235414 (2003).

[3] A. K. Hüttel, G. A. Steele, B. Witkamp, M. Poot, L. P. Kouwenhoven, and H. S. J. van der Zant, *Carbon Nanotubes as Ultrahigh Quality Factor Mechanical Resonators*, Nano Lett. **9**, 2547 (2009).

[4] J. S. Bunch, A. M. van der Zande, S. S. Verbridge, I. W. Frank, D. M. Tanenbaum, J. M. Parpia, H. G. Craighead, and P. L. McEuen, *Electromechanical Resonators from Graphene Sheets*, Science **315**, 490 (2007).

[5] D. M. Karabacak, S. H. Brongersma, and M. Crego-Calama, *Enhanced sensitivity volatile detection with low power integrated micromechanical resonators*, Lab Chip **10**, 1976 (2010).

[6] S.-S. Li, Y.-W. Lin, Z. Ren, and C.-C. Nguyen, *An MSI Micromechanical Differential Disk-Array Filter*, Solid-State Sensors, Actuators and Microsystems Conference, 2007. pp. 307 –311 (2007).

[7] Z. Yang, B. Zhu, W. Chen, G. Ding, H. Wang, and X. Zhao, *Fabrication and characterization of a multidirectional-sensitive contact-enhanced inertial microswitch with a electrophoretic flexible composite fixed electrode*, J. Micromech. Microeng. **22**, 045006 (2012).

[8] J. Chaste, A. Eichle, J. Moser, G. Ceballos, R. Rurali, and A. Bachtold, *A nanomechanical mass sensor with yoctogram resolution*, Nature Nanotechnol. **7**, 301 (2012).

[9] J. K., Kwanpyo Kim, and Z. A., *An atomic-resolution nanomechanical mass sensor*, Nature Nanotechnol. **3**, 533 (2008), 10.1038/nnano.2008.200.

[10] H.-Y. Chiu, P. Hung, H. W. C. Postma, and M. Bockrath, *Atomic-Scale Mass Sensing Using Carbon Nanotube Resonators*, Nano Lett. **8**, 4342 (2008).

[11] Y. T. Yang, C. Callegari, X. L. Feng, K. L. Ekinci, and M. L. Roukes, *Zeptogram-Scale Nanomechanical Mass Sensing*, Nano Lett. **6**, 583 (2006).

[12] C. Lam, *A review of the recent development of MEMS and crystal oscillators and their impacts on the frequency control products industry*, Proc. IEEE Ultrasonics Symp. pp. 694 –704 (2008).

[13] C.-C. Nguyen and R. Howe, *An integrated CMOS micromechanical resonator high-Q oscillator*, Solid-State Circuits, IEEE Journal of **34**, 440 (1999), ISSN 0018-9200.

[14] W. J. Venstra, H. J. R. Westra, and van der Zant HSJ, *Mechanical stiffening, bistability, and bit operations in a microcantilever*, Appl. Phys. Lett. **97**, 193107 (2010).

[15] D. Roodenburg, J. W. Spronck, H. S. J. van der Zant, and W. J. Venstra, *Buckling beam micromechanical memory with on-chip readout*, Appl. Phys. Lett. **94**, 183501 (pages 3) (2009).

[16] I. Mahboob and H. Yamaguchi, *Bit storage and bit flip operations in an electromechanical oscillator*, Nature Nanotech. **3**, 275 (2008).

[17] I. Mahboob, Q. Wilmart, K. Nishiguchi, A. Fujiwara, and H. Yamaguchi, *Wideband idler generation in a GaAs electromechanical resonator*, Phys. Rev. B **84**, 113411 (2011).

[18] I. Mahboob, E. Flurin, K. Nishiguchi, A. Fujiwara, and H. Yamaguchi, *Interconnect-free parallel logic circuits in a single mechanical resonators*, Nat. Commun. **2**, 198 (2011).

[19] M. Mehregany, C. Zorman, N. Rajan, and C. H. Wu, *Silicon carbide MEMS for harsh environments*, Proceedings of the IEEE **86**, 1594 (1998), ISSN 0018-9219.

[20] S. Alper and T. Akin, *A Single-Crystal Silicon Symmetrical and Decoupled MEMS Gyroscope on an Insulating Substrate*, J. Microelectromech. Syst. **14**, 707 (2005).

[21] H. Qu, D. Fang, and H. Xie, *A single-crystal silicon 3-axis CMOS-MEMS accelerometer*, IEEE Sensors J. **2**, 661 (2004).

[22] G. Binnig, C. F. Quate, and C. Gerber, *Atomic Force Microscope*, Phys. Rev. Lett. **56**, 930 (1986).

[23] M. Poot and H. S. J. van der Zant, *Nanomechanical properties of few-layer graphene membranes*, Appl. Phys. Lett. **92**, 063111 (2008).

[24] D. Antonio, D. H. Zanette, and D. Lopez, *Frequency stabilization in nonlinear micromechanical oscillators*, Nat. Commun. **3**, 806 (2012).

[25] A. W. Barnard, V. Sazonova, A. M. van der Zande, and P. L. McEuen, *Entropic spectral broadening in carbon nanotube resonators* (2011), , arXiv:1110.1517v1.

[26] M. I. Dykman, *Fluctuating nonlinear oscillators* (Oxford University Press, 2012).

[27] S. H. Strogatz, *Nonlinear dynamics and chaos* (Westview Press, 1994).

[28] A. H. Nayfeh and D. T. Mook, *Nonlinear oscillations* (Wiley, 1995).

[29] R. Lifshitz and M. C. Cross, *Nonlinear dynamics of nanomechanical and micromechanical resonators* (Wiley, Meinheim, 2008), vol. 1, chap. 1, pp. 1–52.

[30] E. Zeeman, in *Structural Stability, the Theory of Catastrophes, and Applications in the Sciences*, edited by P. Hilton (Springer Berlin / Heidelberg, 1976), vol. 525 of *Lecture Notes in Mathematics*, pp. 373–395.

[31] L. Golubović, D. Moldovan, and A. Peredera, *Dynamics of the Euler Buckling Instability*, Phys. Rev. Lett. **81**, 3387 (1998).

2

NONLINEAR MECHANICS AND MODAL INTERACTIONS

The influence of nonlinear terms in the equation of motion of a clamped-clamped beam or cantilever is presented. We consider a micromechanical beam and start with a description of its linear behavior. Then, the nonlinearity is introduced in the equation of motion and a method is presented, which solves the nonlinear differential equations. We show how the nonlinearity couples the vibrational modes in a clamped-clamped micromechanical beam.

2.1 INTRODUCTION

RESEARCHERS have been studying mechanics for a long time. It dates back to the ancient Greek with Aristotle and his *Mechanica*, describing the principles behind a lever and scale. Much later in 1687, Sir Isaac Newton wrote his *Principia Mathematica*, discussing gravity and the foundation of mechanics. So if the physics and its corresponding mathematical framework are known for decades, why would one still want to study the mechanics of a system as simple as a beam supported at one or both ends? To answer this question, I will first introduce two recent developments in science: the downscaling of mechanics into the nano- and micrometer regime and the interest in solving (coupled) nonlinear differential equations.

With the rise of silicon-based fabrication techniques for designing on-chip electrical circuits, 'mechanical circuits' have now also made the step towards the micro- and even nanometer scale. Micro- and nanomechanical systems (MEMS and NEMS) are used in on-chip sensor schemes as mass or force sensors. For example, MEMS are used to detect small masses or concentration down to single atom resolution [1–4]. Also, atomic force microscopes rely on microcantilevers, which transduce forces at the atomic scale to a measurable signal [5].

In mathematics, nonlinear dynamics have been studied extensively, since exciting phenomena like bifurcations, period doubling and chaotic behavior arise from the equations. In many cases, the analytic solution is not available. With the recent increase in computing power, solving the corresponding nonlinear differential equations numerically is now possible in a reasonable time span. However, examples of physical model systems which can be described with these equations are not numerous. One system is a mechanical system, where the dynamics is limited by a nonlinearity. The motion of small-scale mechanics occurs at short timescales and this allows detailed experimental studies of the nonlinear mechanics, Surprisingly, in basic structures, like cantilever and clamped-clamped beams, the nonlinearity is not well-studied. However, interesting dynamics can be observed in the nonlinear regime [6, 7]. Moreover, their easy fabrication makes them excellent model systems.

In this Chapter, we give an overview of the combination of nonlinear dynamics and nonlinear interactions in single-clamped beams (cantilevers) and clamped-clamped beams. Starting with the linear description of these systems, the equations of motion will be extended with the nonlinear terms. Finally, we will add the nonlinear interactions between the different modes and conclude with an outlook of the research field.

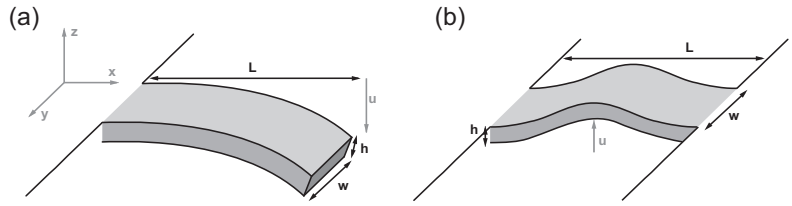

FIGURE 2.1: (a) Cantilever geometry, where a beam is clamped at one side, with dimensions length (L), width (w) and height (h) and displacement u. (b) Clamped-clamped geometry.

2.2 LINEAR BEHAVIOR

We start the description of the linear behavior of cantilevers and clamped-clamped beams by considering the flexural modes of a beam. Schematics of the cantilever and clamped-clamped geometry and its coordinate system is given in Fig. 2.1(a) and 2.1(b). For a beam with length L, width w and height h, the dynamic behavior is described by the dynamic Euler-Bernoulli equation [1]:

$$D\frac{\partial^4 \tilde{u}(x,t)}{\partial x^4} + \rho w h \frac{\partial^2 \tilde{u}(x,t)}{\partial t^2} = q(x,t), \tag{2.1}$$

where D denotes the bending rigidity, t is the time, ρ the density of the beam, and q is the distributed load. The bending rigidity can be written as $D = EI_y$, where E is the Young's modulus of the material and I_y is the second moment of inertia and for a rectangular beam is given by $I_y = wh^3/12$.

Equation 2.1 can be simplified by applying the Galerkin procedure, where we write the solution in the form $\tilde{u}(x,t) = \xi_i(x)u(t)$. Here $u(t)$ is the time-dependent part, and $\xi_i(x)$ is the shape of mode i, with orthonormalization $\int_0^L \xi_i \xi_j \mathrm{d}x = \delta_{ij}$. We assume that the load q is homogeneous over the beam length, $q(x,t) = q(t)$ and that the beam is oscillating with the frequency ω. If $q = 0$, the spatial part of the solutions of Eq. 2.1 is then written as

$$\frac{\mathrm{d}^4 \xi(x)}{\mathrm{d}x^4} = \beta^4 \xi(x), \tag{2.2}$$

where $\beta^4 = \frac{\rho w h \omega^2}{D}$. Equation 2.2 can be solved if the boundary conditions for the beam are known. For the cantilever, the boundary conditions are given by: $\xi(0) = \xi'(0) = \xi''(L) = \xi'''(L) = 0$, where the primes denote differentiation to x. For the

[1] A derivation of the Euler-Bernoulli equation for beams can be found in Ref. [8]

clamped-clamped geometry, the boundary conditions are given by $\xi(0) = \xi'(0) = \xi(L) = \xi'(L) = 0$. The solution of Eq. 2.2 for the two geometries is given by

$$\cos(\beta L)\cosh(\beta L) = \begin{cases} -1 & \text{cantilever} \\ +1 & \text{clamped-clamped beam} \end{cases} \tag{2.3}$$

For the cantilever, the values of β corresponding to the first three modes are given by: $\beta_i L$ = 1.875, 4.694 and 7.855. For the clamped-clamped beam, these are $\beta_i L$ = 0, 4.730, 7.853 and 10.996 for mode $i = 1,2$ and 3. With these values, the mode shapes of the beam can be calculated. The first mode of the cantilever and clamped-clamped beam are sketched in Fig. 2.1.

Considering only one mode, its dynamic behavior is described by the time-dependent part of Eq. 2.1 (multiplied by the length L):

$$m\frac{\mathrm{d}^2u(t)}{\mathrm{d}t^2} + \gamma\frac{\mathrm{d}u(t)}{\mathrm{d}t} + ku = F, \tag{2.4}$$

where we added a term with $\gamma\dot{u}(t)$, which accounts for the damping of the beam motion. The spring constant is given by $k = \beta^4\frac{Ewh^3L}{12}$ and the mass is m. The beam is driven by a force F. For the force, we will consider two experimental situations, one where the mechanical beam is driven by thermal noise and an other where the beam is driven by a harmonic force. We note that Eq. 2.4 has the form of a damped driven harmonic oscillator and the motion of the beam can be described by a particle in a quadratic potential. When the particle is displaced from the equilibrium position, the spring constant (the bending rigidity) will exert a force towards the equilibrium position. This is illustrated in Fig. 2.2(a). Depending on the damping, the particle will oscillate in the well or the motion will be damped out.

The spectral density of the thermal driving force is given by

$$S_F(\omega) = 4k_BTm\gamma, \tag{2.5}$$

where k_B is Boltzmann's constant and T is the temperature. ω_0 is the resonance frequency given by $\sqrt{k/m}$, and the quality factor is $Q = m\omega_0/\gamma$. The quality factor or Q factor of a mechanical system is high if there is little damping. From the fluctuation-dissipation theory, it follows that the amount of kinetic and potential energy is provided by the thermal energy and is given by

$$\frac{1}{2}k_BT = \frac{1}{2}k\langle x\rangle^2 = \frac{1}{2}m\langle v\rangle^2. \tag{2.6}$$

The dynamics of a cantilever with a Q factor of 50 driven by a thermal noise at room temperature (T = 300 K), can be simulated by integrating Eq. 2.4 with a stochastic

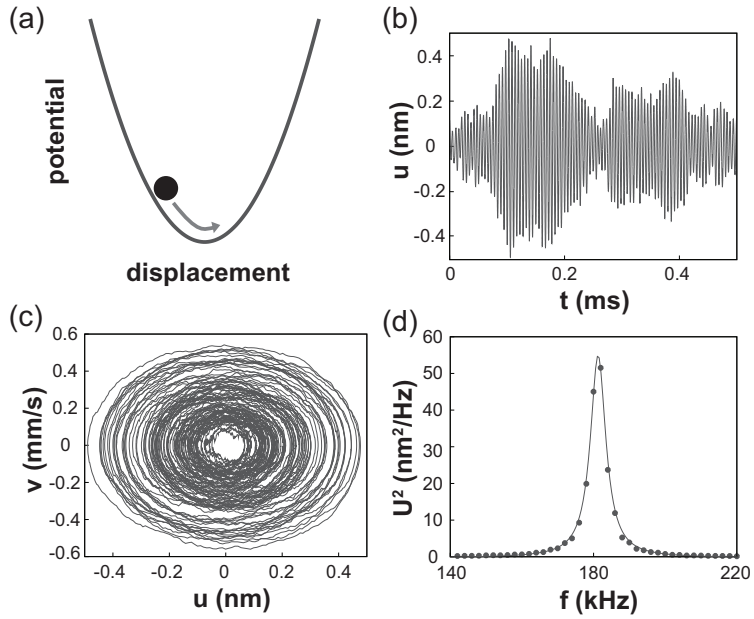

FIGURE 2.2: (a) The cantilever motion described by the motion of a particle in a harmonic potential. (b) Simulated time trace of a silicon nitride cantilever (E = 250 GPa, ρ = 3100 kg m^{-3}) displacement u with dimensions $L \times w \times h = 40 \times 8 \times 0.2$ μm^3. (c) Phase-space representation of the cantilever motion. (d) Fast Fourier Transform of the displacement (circles) with a Lorentzian fit (solid line), showing the resonance peak.

force (Fig. 2.2). A 4th-order Runge-Kutta integration method with fixed time-steps is used. The first mode of the cantilever resonator with dimensions mentioned in the caption of Fig. 2.2 is simulated for 0.5 ms. Figure 2.2(b) shows a time trace of the resonator displacement, showing a oscillation with an amplitude changing over time. It is convenient to represent the motion in a plot with position and velocity on the axes. In Fig. 2.2(c) this phase-space representation of the time trace is given, showing a circular trajectories in phase space around (0,0). The resonator is oscillating around its equilibrium position, but has never zero velocity at zero displacement. Finally, Fig. 2.2(d) shows the Fast Fourier Transform (FFT) of 100 simulated time traces (circles). The peak in the spectrum at 181 kHz corresponds to the resonance frequency of the fundamental cantilever mode and the peak shape can be fitted with a Lorentzian function. This becomes apparent when Eq. 2.4 is

solved in the frequency domain (with a harmonic driving force $F = F_0 \cos(\omega t)$):

$$|U(\omega)| = \frac{F_0}{m} \frac{1}{\sqrt{(\omega_0^2 - \omega^2)^2 + \omega_0^2 \omega^2 / Q^2}}, \tag{2.7}$$

which for high Q factors ($Q \gg 1$), results in a Lorentzian line shape. By integration of the PSD over the resonator band, the energy is obtained. In this case this is the thermal energy.

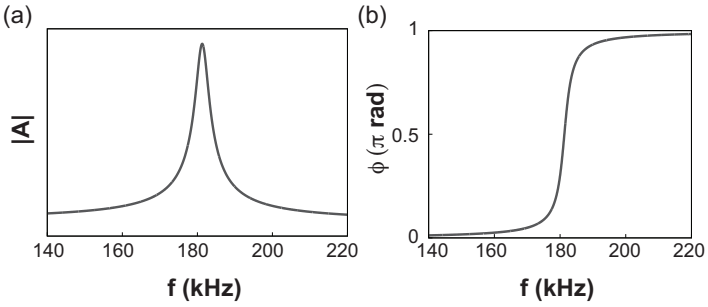

FIGURE 2.3: Simulated driven frequency responses of the same cantilever as in Fig. 2.2. (a) Amplitude and (b) phase response of the resonator.

When an periodic force is exerted on the resonator ($F = F_0 \cos(\omega t)$), the beam can be driven on resonance. Now, the resonator has a fixed phase with respect to the one of the driving frequency [$U = |U| \cos(\omega t - \phi)$]. The amplitude-frequency relation is the same as Eq. 2.7, and the phase-frequency relation is given by

$$\phi(\omega) = \tan^{-1}\left(\frac{\omega_0 \omega}{Q(\omega_0^2 - \omega^2)}\right). \tag{2.8}$$

The amplitude and phase of the same cantilever as in Fig. 2.2 are given in Fig. 2.3. The amplitude response shows the resonance peak and the phase shifts over π radians when crossing the resonance.

2.3 ORIGIN OF THE NONLINEARITY

From Eq. 2.7 it follows that the amplitude of the displacement increases linearly with the force. For small applied forces this is an accurate description, but for larger forces, unphysical displacements which are larger than the beam length can

occur. A larger restoring force is necessary to describe the beam motion at large amplitudes. The harmonic oscillator potential can be extended with higher powers in the displacement: $V(u) = \sum_n C_n u^n$ with constants C_n. The odd powers with displacement however result in a symmetry-breaking potential: the potential is different depending on which side of the equilibrium the beam is. In many cases this is unphysical and in this Thesis we neglect these terms. The next even power with displacement in the harmonic potential is u^4, which results in a u^3 term in the equation of motion. This is known as the Duffing nonlinearity and it turns out that this term is non-negligible for large displacements and is used to describe the nonlinear dynamics of beam motion. The origin of this nonlinear behavior depends on the boundary conditions and is thus different for a clamped-clamped beam compared to that for a cantilever. In this Thesis, we focus on the nonlinearity arising from the mechanics. Nonlinearities arising from electrostatics, single electron tunneling are discussed in Ref. [9] We will thoroughly discuss the origin of the Duffing nonlinearity in the clamped-clamped beam, and mention how nonlinearity affects the cantilever dynamics.

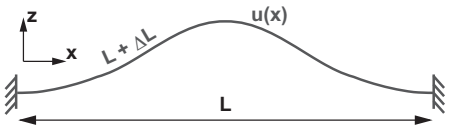

FIGURE 2.4: Schematic of a clamped-clamped beam which is extended with an extra length ΔL.

For large displacements of a clamped-clamped beam with length L, the beam extends by a small amount ΔL, as can be seen in Fig. 2.4. The extension leads to tensioning in the beam and the spring constant is depending on the amplitude $k(u) = k_0 + k_3 u^3$. This spring constant is then used in the equation of motion. To calculate k_3 for a clamped-clamped beam, we start by writing the total length of the beam as [10]:

$$L + \Delta L = \int_0^L \sqrt{1 + \left(\frac{\partial \tilde{u}(x)}{\partial x}\right)^2}. \tag{2.9}$$

The square root can be Taylor-expanded and the extra length is

$$\Delta L = \frac{1}{2}\int_0^L \left(\frac{\partial \tilde{u}(x)}{\partial x}\right)^2 \mathrm{d}x. \tag{2.10}$$

The lengthening of the beam induces tension in the beam. This tension (stress

force) related to this extra length is written as

$$T = \frac{Ewh}{2L}\int_0^L \left(\frac{\partial \tilde{u}(x)}{\partial x}\right)^2 \mathrm{d}x. \tag{2.11}$$

Incorporating this force in the equation of motion gives a nonlinear differential equation

$$D\frac{\partial^4 \tilde{u}(x,t)}{\partial x^4} + \rho wh\frac{\partial^2 \tilde{u}(x,t)}{\partial t^2} - \left(\frac{Ewh}{2L}\int_0^L \left(\frac{\partial \tilde{u}(x)}{\partial x}\right)^2 \mathrm{d}x\right)\frac{\partial^2 \tilde{u}(x,t)}{\partial x^2} = q(x,t). \tag{2.12}$$

From this equation, the tension term can already be identified as a Duffing nonlinearity since it has a $\tilde{u}^3$ dependence. Equation 2.12 can be evaluated by first evaluating the homogeneous part of the differential equation, which is Eq. 2.2. This equation gives the linear mode shapes and resonance frequencies for mode i of the oscillation. Focussing on one resonance mode, $\tilde{u}(x,t) = \xi_i(x)u(t)$, the time-dependent part of Eq. 2.12 can be written as [9]

$$\frac{\mathrm{d}^2 u}{\mathrm{d}t^2} + \frac{\omega_i}{Q}\frac{\mathrm{d}u}{\mathrm{d}t} + \omega_i^2 u + \frac{I_i^2 E}{2L^4\rho}u^3 = c_i\frac{q}{\rho wh}cos(\Omega t), \tag{2.13}$$

where the value of the integral $I_i = L\int_0^L \frac{\mathrm{d}^2\xi_i}{\mathrm{d}x^2}\xi_i \mathrm{d}x$ for the first three modes is 12.3, 46.1 and 98.9 respectively. $c_i = \frac{1}{L}\int_0^L \xi_i \mathrm{d}x$ is 0.83, 0 and 0.36 for the first three modes, and $\omega_i = \frac{\beta_i^2}{L^2}\sqrt{\frac{D}{\rho wh}}$ is the resonance frequency. Note that $\int_0^L \xi_i\xi_j \mathrm{d}x = L\delta_{ij}$.

In Eq. 2.13, the well-known Duffing equation can be recognized, which also describes the current-phase relation in Josephson junctions. The equation is written in the frequency domain by inserting $u = ae^{i\Omega t}$:

$$\Omega^2 a - \omega_i^2 a + i\frac{\omega_i\Omega}{Q}a + \frac{I_i^2 E}{2L^4\rho}a^3 = c_i\frac{q_i}{\rho A}. \tag{2.14}$$

This equation needs to be solved self-consistently. The amplitude and phase response of the displacement can be calculated from Eq. 2.14 and can be found in e.g. Ref. [6]. Considering the first mode of a clamped-clamped beam with dimensions mentioned in the caption of Fig. 2.2, the frequency responses are calculated for different values of the drive strength q in Fig. 2.5, where the amplitude response is plotted in (a). For low drive strengths, the damped driven harmonic oscillator response is found (light gray), but for higher drive strengths the response tilts to the right and deviates from the Lorentzian line shape. Beyond a critical amplitude and for a certain frequency span, equation 2.14 has three solutions: two stable ones (at

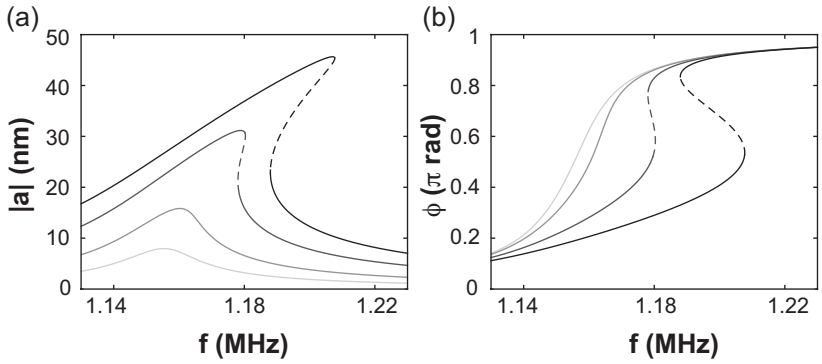

FIGURE 2.5: (a) Amplitude response of the Duffing equation for a clamped-clamped beam with properties mentioned in the caption of Fig. 2.2 for drive strengths 50 (light gray), 100, 200 and 300 (black) μN/m. (b) Phase responses for the same drive strengths q. Dotted lines indicate the unstable solutions.

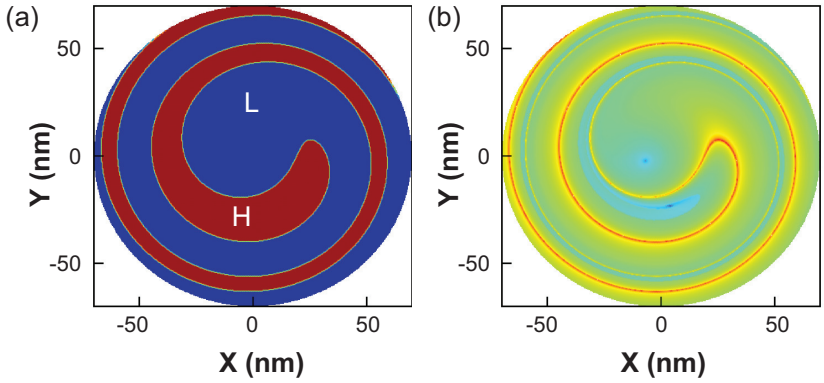

FIGURE 2.6: (a) Basins of attraction of the clamped-clamped beam at $q = 300$ μN and $\Omega = 2\pi \times 1.195$ MHz. Red (blue) indicates that the resonator resides in the high, H (low, L) amplitude state when the resonator is released at the initial conditions (X, Y). (b) Color scale indicates the time it takes for the resonator to end up in one of the basins of attraction. Time increases from blue to red. Along the separatrix (red line), the resonator takes the longest time to end up in one of the attractors.

a high and low amplitude) and one unstable solution [dashed line in Fig. 2.5(a)]. The critical amplitude at which this bistability occurs is $a_c = \frac{2h}{3^{3/4}} \frac{1}{\sqrt{Q}}$ for a beam with rectangular cross section.

In the bistable region, two stable amplitudes (fixed points in phase space) exist. They are called 'attractors' as the beam oscillates around these points, an if there is damping, the system will converge to one of them. One way to solve the Eq. 2.13 is by separating the time scales. We write the position in the form $u(x,t) = A(T)e^{i\omega t} +$ c.c., where c.c. is the complex conjugate and $A(T) = [X(T) + iY(T)]e^{i\omega\sigma/t}$. Here, T is the time-scale for the slow moving amplitude, and $\sigma = 2Q(\Omega/\omega - 1)$ [11]. The Duffing equation in terms of X and Y is

$$\frac{dX}{dt} = -\frac{\omega X}{2} + \frac{\omega\sigma Y}{2} - \frac{3}{2}\frac{\alpha Q}{\omega}(X^2+Y^2)Y, \tag{2.15}$$

$$\frac{dY}{dt} = -\frac{\omega Y}{2} + \frac{\omega\sigma X}{2} + \frac{3}{2}\frac{\alpha Q}{\omega}(X^2+Y^2)X - \frac{\eta q Q}{4\omega}, \tag{2.16}$$

where $\alpha = \frac{I_1^2 E}{2L^4\rho}$ and $\eta = \frac{c_1}{\rho A}$. Figure 2.6 shows the basins of attraction, where the clamped-clamped beam described in Fig. 2.5 are driven in the bistable region. For all possible initial conditions of the resonator in phase space, the final amplitude of the resonator is plotted in Fig. 2.6(a). In this plot, H indicates the high amplitude final state and L the low amplitude final state. This plot predicts the stationary solution at $t \to \infty$ for a range of initial conditions. Figure 2.6(b) plots the time it takes for the resonator to move to one each of these states. If the resonators is prepared on the edge between the two basins, the force will be zero, and the resonator will not move. This boundary is called the separatrix and it represents the unstable stationary points. In practice, fluctuations will cause the resonator to wander away from these metastable points, this results in a fuzzy separatrix.

For cantilevers, the nonlinearity of the beam's motion is similar to the clamped-clamped beam resonator, but it contains some extra nonlinear terms. A derivation of the equation can be found in Ref. [12] and in Chapter 3. The dimensionless equation is given by

$$\ddot{a} + \omega^2 a + \eta\dot{a} + 40.44\delta a^3 + 4.60\delta(a\dot{a}^2 + a^2\ddot{a}) = -0.78l\Omega^2\cos(\Omega t), \tag{2.17}$$

where $\delta = (h/L)^2$ and l the driving strength. The fourth term is recognized as a Duffing term and the fifth term represents other nonlinear terms, specific for a cantilever. The nonlinearity arises from the geometry and inertia. For large displacements, the cantilever effectively becomes shorter: this results in the term cubic in a (fourth term in Eq. 2.17). The fifth term represents nonlinear inertial effects in the cantilever.

2.4 MODAL INTERACTIONS

Thus far, we only considered one resonance mode of a cantilever or clamped-clamped beam resonator. A mechanical resonator has many degrees of freedom,

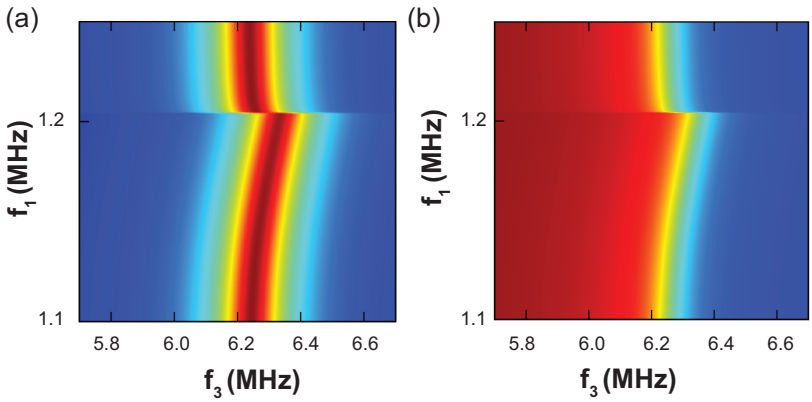

FIGURE 2.7: Nonlinear interactions between the first and third mode of the clamped-clamped beam with properties as in the caption of Fig. 2.2. The third mode is driven in the linear regime at 100 μN/m and the first mode is driven in the nonlinear regime with 700 μN/m. Amplitude (a) and phase (b) response of the third mode (forward sweep) is shown when the first mode is swept from low to high through its nonlinear resonance. The nonlinear response is reflected in the shift in resonance frequency of the third mode.

all of them are provided with at least the thermal energy. In general, such structures are analyzed by assuming the modes are independent and provide an orthogonal basis to describe the motion of the rigid body. However, in this Thesis it is shown that the nonlinearity couples these modes, this coupling is called the nonlinear modal interaction. The coupling originates from the tension in the beam. Intuitively, one can explain the modal interactions by the tension in the beam. The tension from one mode is also experienced by the other modes, and it tunes their resonance frequencies. Mathematically, we write the dimensionless tension in a clamped-clamped beam as

$$T(t) = \frac{\tau}{2} \sum_{i,j=0}^{\infty} u_i(t) u_j(t) I_{ij}, \tag{2.18}$$

where the integral $I_{ij} = \int_0^1 \frac{\mathrm{d}\xi_i}{\mathrm{d}x} \frac{\mathrm{d}\xi_j}{\mathrm{d}x} \mathrm{d}x$ and $\tau = h^2 A / I_y = 12$ for a rectangular beam. The dimensionless displacement u is written as the sum of all modes: $u = \sum_i |a_i| \xi_i \cos(\omega_i t)$.

This is inserted in Eq. 2.18 to obtain the equation of motion of mode i:

$$\sum_{i\neq j>0}\Big\{\Big(\omega_{0,i}^2-\omega_i^2+i\omega_i\omega_{0,i}/Q_i+\frac{\tau}{4}|a_i|^2I_{ii}^2 + \frac{\tau}{4}\Big(|a_j|^2I_{ii}I_{jj}+|a_j|^2I_{ij}^2\Big)\Big)a_i-\int_0^1 F_{\mathrm{ac},i}\xi_i\,\mathrm{d}x\Big\}=0. \tag{2.19}$$

A more detailed discussion of this equation and its consequences can be found in Chapter 5. From this equation, it follows that all flexural modes in a clamped-clamped beam are coupled. Focussing on only two flexural modes, the coupled equations are obtained:

$$\Big\{\omega_{0,1}^2-\omega_1^2+i\omega_1\omega_{0,1}/Q_1+\frac{\tau}{4}\Big(|a_1|^2I_{11}^2 + |a_2|^2I_{22}I_{11}+|a_2|^2I_{12}^2\Big)\Big\}a_1=\int_0^1 F_{\mathrm{ac},1}\xi_1\,\mathrm{d}x, \tag{2.20}$$

$$\Big\{\omega_{0,2}^2-\omega_2^2+i\omega_2\omega_{0,2}/Q_2+\frac{\tau}{4}\Big(|a_2|^2I_{22}^2 + |a_1|^2I_{11}I_{22}+|a_1|^2I_{12}^2\Big)\Big\}a_2=\int_0^1 F_{\mathrm{ac},2}\xi_2\,\mathrm{d}x. \tag{2.21}$$

These two equations can be solved self-consistently. In these equations, there are four variables: the drive frequencies and drive strengths of the two modes. As an example, the equations are worked out for the first and third mode of a clamped-clamped beam. When we consider a homogeneous force along the beam, the even modes are not excited, since the integral on the right hand side of Eqs. 2.20 vanishes. For the third mode, $\beta_3^2=120.9$. Figure 7.2(a) shows the amplitude of the frequency response of the third mode, when the first mode is driven strongly in the nonlinear regime. The resonance frequency of the third mode increases, when the first mode is vibrating strongly. This strong vibration of the first mode causes an extra tension in the beam, which makes the beam stiffer and therefore also increases the resonance frequency of the third mode (and all other modes in the beam). In this way, the nonlinear frequency response of the first mode is reflected in the resonance frequency of the third mode. For small amplitudes, it can be shown that there is a quadratic dependence of the resonance frequency of one mode on the amplitude of another mode. The phase response, shown in Fig. 7.2(b), also shows the shift in resonance frequency.

For a cantilever, the equations for the nonlinear coupling are a bit more elaborate to analytically work out. The full derivation is given in the Appendix A. The principle and consequences of the modal interactions is however similar to the clamped-clamped beam case. However, there is also a coupling between the flex-

ural and torsional modes. An experimental investigation of the nonlinear coupling in cantilevers is discussed in Chapter 6.

2.5 CONCLUSION

Micromechanical resonators provide simple systems in which nonlinear terms in the equation of motion can not be neglected. In general, a force term cubic in the displacement is sufficient to predict the system dynamics. The Duffing equation applies to these systems in the large-vibration regime. It is also shown that the nonlinearity couples the different modes in the beams.

REFERENCES

[1] M. Li, H. X. Tang, and M. L. Roukes, *Ultra-sensitive NEMS-based cantilevers for sensing, scanned probe and very high-frequency applications*, Nature Nanotech. **2**, 114 (2007).

[2] A. K. Naik, M. S. Hanay, W. K. Hiebert, X. L. Feng, and M. L. Roukes, *Towards single-molecule nanomechanical mass spectrometry*, Nature Nanotech. **4**, 445 (2009).

[3] J. K., Kwanpyo Kim, and Z. A., *An atomic-resolution nanomechanical mass sensor*, Nature Nanotechnol. **3**, 533 (2008), 10.1038/nnano.2008.200.

[4] B. Lassagne, D. Garcia-Sanchez, A. Aguasca, and A. Bachtold, *Ultrasensitive Mass Sensing with a Nanotube Electromechanical Resonator*, Nano Lett. **8**, 3735 (2008).

[5] G. Binnig, C. F. Quate, and C. Gerber, *Atomic Force Microscope*, Phys. Rev. Lett. **56**, 930 (1986).

[6] R. Lifshitz and M. Cross, *Nonlinear dynamics of nanomechanical and micromechanical resonators*, Rev. Nonlinear Dyn. Complexity **1**, 1 (2008).

[7] N. Kacem, S. Hentz, D. Pinto, B. Reig, and V. Nguyen, *Nonlinear dynamics of nanomechanical beam resonators: improving the performance of NEMS-based sensors*, Nanotechnology **20**, 275501 (2009).

[8] A. N. Cleland, *Foundations of nanomechanics: from solid-state theory to device applications*. (Springer, 2003).

[9] M. I. Dykman, *Fluctuating nonlinear oscillators* (Oxford University Press, 2012).

[10] L. D. Landau and E. Lifshitz, *Theory of elasticity* (Butterworth Heinemann, 1959).

[11] I. Kozinsky, H. W. ChPostma, O. Kogan, A. Husain, and M. L. Roukes, *Basins of attraction of a nonlinear nanomechanical resonator*, Phys. Rev. Lett. **99**, 207201 (2007).

[12] M. R. M. Crespo da Silva and C. C. Glynn, *Nonlinear Flexural-Flexural-Torsional Dynamics of Inextensional Beams. I. Equations of motion*, J. Struct. Mech. **6**, 437 (1978).

3

NONLINEAR DYNAMICS IN A CANTILEVER

We investigate the nonlinear dynamics of microcantilevers. We demonstrate mechanical stiffening of the frequency response at large amplitudes, originating from the geometric nonlinearity. At strong driving the cantilever amplitude is bistable. We map the bistable regime as a function of drive frequency and amplitude, and suggest several applications for the bistable microcantilever, of which a mechanical memory is demonstrated.

Parts of this chapter have been published in Appl. Phys. Lett. **97** 193107 (2010) [1]

3.1 INTRODUCTION

MICROCANTILEVERS are widely applied as transducers in sensitive instrumentation [2, 3], with scanning probe microscopy as a clear example. Typically, the cantilever is operated in the linear regime, i.e., it is driven by a harmonic force at moderate strength, and its response is modulated by the parameter to be measured. In clamped-clamped mechanical resonators, additional applications have been proposed based on nonlinear behavior. Nonlinearity in clamped-clamped beams is due to the extension of the beam, which results in frequency pulling and bistability at strong driving, and can be described by a Duffing equation [4]. Applications which employ this bistability are, e.g., elementary mechanical computing functions [5, 6]. Since a cantilever beam is clamped only at one side, it can have a nonzero displacement without extending. One would therefore not expect a Duffing-like behavior for a cantilever beam. Nonlinear effects of a different origin have been observed in scanning probe microscopy, due to interactions between the cantilever and its environment. Tip-sample interactions either weaken or stiffen the cantilever response, depending on the strength of the softening Van der Waals forces and electrostatic interactions and the hardening short range interactions [7, 8]. Weakening also occurs when the cantilever is driven by an electrostatic force [9]. Besides nonlinear interactions with the environment, theoretical studies predict *intrinsic* nonlinear behavior of cantilever beams [9–12], but to our knowledge a detailed experimental analysis thereof has not been reported [12, 13].

In this Chapter, we report a detailed experimental analysis on the nonlinear mechanics of microcantilevers. It is shown that a hardening geometric nonlinearity dominates over softening nonlinear inertia, which effectively leads to a stiffening frequency response for the fundamental mode. At large amplitudes, the mechanical stiffening results in frequency pulling and ultimately in intrinsic bistability of the cantilever. We study the bistability in detail by measuring the cantilever response as a function of the frequency and amplitude, and compare the experimental observations with theory. A good agreement is found. We suggest several applications for the bistable cantilever, and as an example we demonstrate that bit operations can be implemented in the bistable cantilever.

3.2 MECHANICAL FREQUENCY STIFFENING

Experiments are performed on thin cantilevers with a rectangular cross section, $w \times h$, fabricated from low-pressure chemical vapor deposited silicon nitride using electron beam lithography and an isotropic reactive ion etching release process. Figure 3.1(a) shows a scanning electron micrograph of a fabricated cantilever. The cantilever is mounted on a piezoactuator and placed in a vacuum chamber at a pressure of $\sim 10^{-4}$ mbar. At this pressure, the cantilever operates in the intrinsic

damping regime. An optical deflection technique is deployed to detect the displacement of the driven cantilever, and the frequency response is measured using a network analyzer, see Fig. 3.1(b).

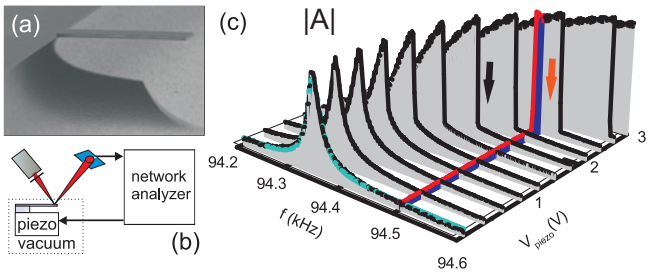

FIGURE 3.1: (a) Scanning electron micrograph of a silicon nitride cantilever; (b) experimental setup; (c) response lines for several drive voltages (forward frequency sweeps). A damped driven harmonic oscillator fit is shown for the weakly driven cantilever. The line at f = 94.5 kHz represents a response line along the (decreasing) drive strength axis. The arrows indicate the switching direction.

Figure 3.1 (c) shows frequency response lines for a weakly and strongly driven cantilever with length L = 40 μm and $w \times h$ = 8 μm × 200 nm. For weak driving the response fits a damped driven harmonic oscillator, with f_0 = 94.35 kHz and $Q \approx 3000$. Figure 3.1(c) also shows the response when driven at increasing strength: the resonance peak shifts to a higher value and the response becomes bistable. It resembles the response of a clamped-clamped beam driven in the nonlinear regime. A more detailed measurement is presented in Figs. 3.2(a) and 3.2(b). Here the magnitude of the resonator response, $|A|$, is depicted (color scale) as a function of the drive frequency and strength. The frequency is swept forward (i.e. from a low to a high frequency, FW) and backward (BW), and after each frequency response measurement the drive strength is increased. Parameters which result in a hysteretic (HY) response are visualized by subtracting forward and backward traces, as shown in Fig. 3.2(c).

The theory of nonlinear oscillations of a cantilever beam due to geometric nonlinearity has been developed in Ref. [10]. Using the extended Hamilton principle the equation of motion for the displacement $\tilde{u}$ has been derived

$$D[\tilde{u}'''' + [\tilde{u}'(\tilde{u}'\tilde{u}'')']'] + \rho w h \ddot{\tilde{u}} + \tilde{\eta}\dot{\tilde{u}} + \frac{1}{2}\rho w h\left(\tilde{u}' \int_L^s \frac{\partial^2}{\partial \tilde{t}^2} \int_0^{s_1} (\tilde{u}')^2 ds_2 ds_1\right)' = \tilde{F}. \quad (3.1)$$

The dots and primes denote differentiation to time $\tilde{t}$ and the arc length s of the cantilever respectively, and D is the bending rigidity, ρ the density, and $\tilde{\eta}$ is the

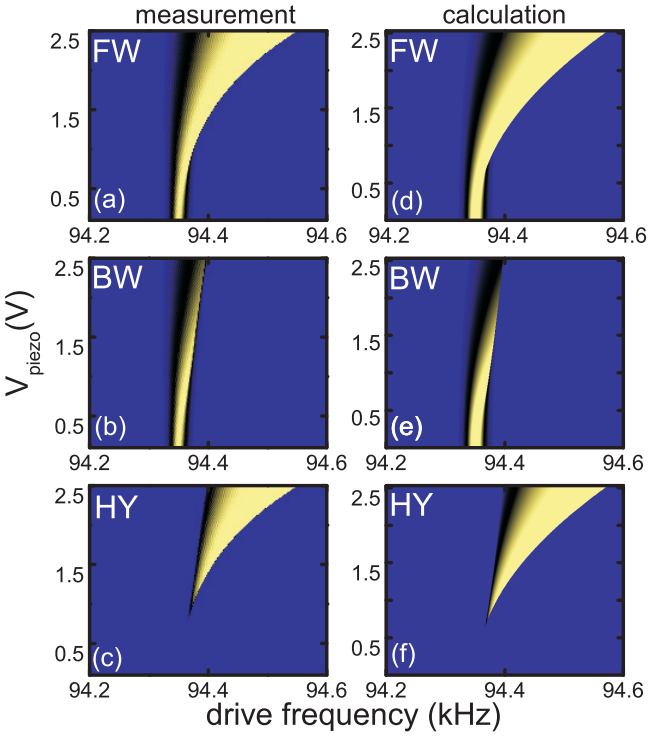

FIGURE 3.2: Frequency pulling and bistability in a cantilever, measurement (left) and calculation by solving Eq. 3.3 (right). The drive frequency is swept from a low to a high value [(a) and (d)] and vice versa [(b) and (e)]. Panels (c) and (f) show the bistable regime, obtained by subtracting the forward from the backward response. As the piezoelectric coupling parameter is not known, the y-axis in the calculations has been scaled to match the experimental values. The color scales (blue to yellow) indicates the amplitude of the motion normalized to the drive strength.

damping parameter. The piezo actuator generates a displacement $U = d_{33} V \cos(\tilde{\Omega} t)$, where V is the drive voltage and d_{33} the piezoelectric coefficient. The resulting load on the cantilever equals $\tilde{F} = \ddot{U} \rho w h = -\tilde{\Omega}^2 \rho w h d_{33} V \cos(\tilde{\Omega} t)$. Equation 3.1 is transformed to a dimensionless form by substituting $u = \tilde{u}/h$, $x = s/L$, $l = d_{33} V/h$, $\eta = \eta' L^4/(D\tau)$ and $\delta = h/L$. The time $\tilde{t}$ and drive frequency $\tilde{\Omega}$ are normalized using $\tau = L^2\sqrt{\rho w h/D}$. Applying the Galerkin procedure [9, 14] for the first mode $[u = a(t)\xi(x)]$ gives

$$\ddot{a} + \omega^2 a + \eta \dot{a} + 40.44\delta a^3 + 4.60\delta(a\dot{a}^2 + a^2\ddot{a}) = -0.78 l \Omega^2 \cos(\Omega t). \qquad (3.2)$$

Here, a is the normalized coordinate, and ω is the dimensionless resonance frequency; for the first mode $\omega = 3.52$. The cubic term in a represents the hardening geometric nonlinearity, and the fifth term represents a nonlinear inertia which softens the frequency response [9]. The values 40.44, 4.60 and 0.78 are obtained by integrating the linear mode shapes, $\xi(x)$ [1]. Equation 3.2 can be evaluated using the method of averaging or the method of multiple scales [11] and the amplitude, A, can be implicitly written as

$$A = \frac{l\Omega^2}{\sqrt{6.57[15.16\delta A^2 - \omega\Omega + \omega^2(1 - 1.15\delta A^2)]^2 + 1.64\eta^2\omega^2}}. \tag{3.3}$$

This equation can be solved self-consistently to obtain the resonator amplitude, which is normalized by the drive strength l to obtain the frequency response. Using the experimentally obtained linear resonance frequency, Q factor and the dimensions as input parameters, the frequency responses are calculated as a function of the drive strength. Figures 3.2(d) and 3.2(e) show the simulated stable solutions, which correspond to the resonator response to a the forward and backward frequency sweep. The model captures the observed behavior well, where the piezoelectric coupling parameter is the only free parameter. Both the calculations and the experiments indicate that the geometric nonlinearity dominates over the inertial nonlinearity. Analyzing Eq. 3.3 in detail shows that the nonlinearity depends on the mode shape, $\xi(x)$, and the aspect ratio, δ. For the fundamental mode, the intrinsic nonlinearity in cantilevers always leads to stiffening of the response [2].

3.3 BIT OPERATIONS

The intrinsic mechanical bistability allows cantilever applications similar to the ones implemented in clamped-clamped resonators. As an example, we demonstrate mechanical bit operations in a cantilever with dimensions $L \times w \times h$ = 30 μm × 8 μm × 150 nm, with a linear resonance frequency f_0 = 193.49 kHz and $Q \approx 5800$ in vacuum. For this cantilever, a measurement of the hysteretic regime is shown in Fig. 3.3 [3]. Bit operations can be performed by modulating the drive frequency or the drive strength –or a combination thereof– across the hysteretic

[1] The integrals involving the modeshapes and their derivatives are evaluated as follows: $\int_0^1 \xi(x)(\xi(x)'(\xi(x)'\xi(x)'')')'\mathrm{d}x = 40.44$, $\int_0^1 \xi(x)\mathrm{d}x = 0.78$ and $\int_0^1 \xi(x)(\xi'(x)\int_0^x \int_1^{x_1} \xi'(x_2)^2 \mathrm{d}x_2 \mathrm{d}x_1)' dx = 4.60$.

[2] For the lowest flexural modes, the prefactors in Eq. (2) are 40.44066, 13418.09, 264384.7, and 19166632 for the geometry, 4.596772, 144.7255, 999.9000, and 3951.323 for the nonlinear inertia, and 0.782992, 0.433936, 0.254430, and 0.181627 for the force. The dimensionless frequencies are 3.516015, 22.03449, 61.69721, and 120.9019.

[3] A different piezo actuator is used in this experiment.

regime. This principle is indicated by the arrows in Fig. 3.3(a). The drive strength is modulated by varying the voltage on the piezo at a fixed frequency, as shown in Fig. 3.3(b). A backwards sweep in the drive strength follows the high-amplitude solution, similar to a forwards sweep in drive frequency. This intuitively becomes clear in Fig. 3.1(c), where the transition from a high to a low amplitude occurs during a backward sweep in the drive strength, as is indicated by the red line. During a forward sweep in the drive strength the resonator follows the low-amplitude stable branch, as with a backward sweep in frequency.

To implement the bit, the cantilever is driven in the bistable regime at f =193.50 kHz and V_{piezo} = 10 mV. To set and reset the cantilever bit, the drive voltage is modulated by 2 mV around the operating point, as indicated by the arrows in Fig. 3.3(b). Starting at low amplitude, "0" in Fig. 3.3(c), a high-amplitude "1" is written by temporary increasing the drive voltage to 12 mV. The cantilever switches to a high vibrational amplitude and remains in this state after the drive voltage is set back to the operating point. Next, the drive strength is lowered to 8 mV which resets the cantilever to a low amplitude oscillation, corresponding to "0".

3.4 DISCUSSION AND CONCLUSION

Bistability of cantilever beams can be used for various purposes besides the mechanical memory application described here. For example, the hysteretic frequency response facilitates the readout of cantilever arrays in dissipative environments by employing the scheme described earlier [15]. Bistability may also open the way to use a cantilever as its own bifurcation amplifier [16–19] in for example scanning probe microscopy, thereby enhancing the sensitivity to external stimuli. Finally, we note that despite scaling with the aspect ratio, δ, the bistable regime is also accessible for single-clamped nanoscale resonators such as carbon nanotubes [20].

In conclusion, we investigated the nonlinear oscillations of microcantilever beams. Mechanical stiffening is observed which results in frequency pulling and bistability. The experiments are in excellent agreement with calculated nonlinear response. Several applications for the bistable cantilever are suggested, of which a mechanical memory is demonstrated.

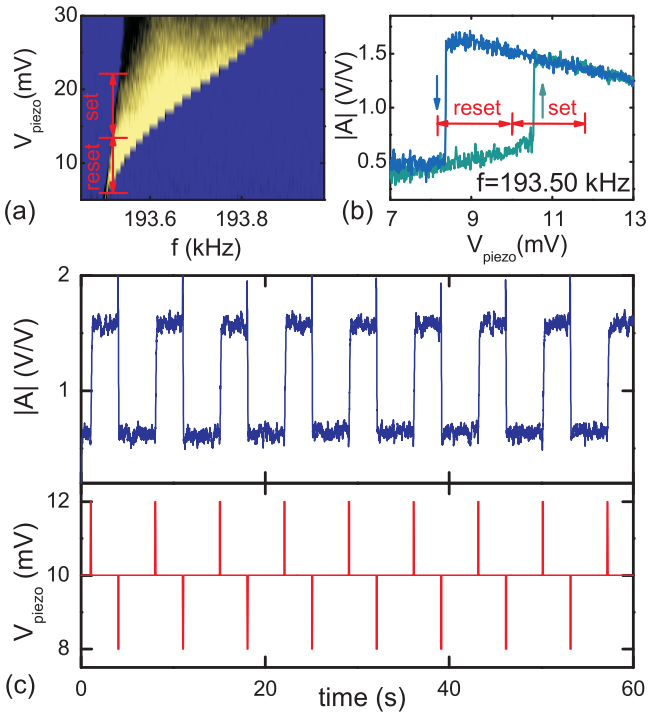

FIGURE 3.3: (a) Hysteretic regime for a 30 μm × 8 μm × 150 nm cantilever. (b) Drive strength sweep at fixed frequency, and indication of the modulation to implement the bit. (c) Mechanical memory in a bistable cantilever beam: drive strength (lower panel) and cantilever response (upper panel).

REFERENCES

[1] W. J. Venstra, H. J. R. Westra, and H. S. J. van der Zant, *Mechanical stiffening, bistability, and bit operations in a microcantilever*, Appl. Phy. Lett. **97**, 193107 (2010).

[2] D. Rugar, R. Budakian, H. Mamin, and B. Chui, *Single spin detection by magnetic resonance force microscopy*, Nature **430**, 329 (2004).

[3] A. C. Bleszynski-Jayich, W. E. Shanks, B. Peaudecerf, E. Ginossar, F. V. Oppen, L. Glazman, and J. G. E. Harris, *Persistent Currents in Normal Metal Rings*, Science **326**, 272 (2009).

[4] I. Kozinsky, H. W. C. Postma, I. Bargatin, and M. L. Roukes, *Tuning nonlinear-*

ity, dynamic range, and frequency of nanomechanical resonators, Appl. Phys. Lett. **88**, 253101 (2006).

[5] R. L. Badzey, G. Zolfagharkhani, A. Gaidarzhy, and P. Mohanty, *A controllable nanomechanical memory element*, Appl. Phys. Lett. **85**, 3587 (2004).

[6] I. Mahboob and H. Yamaguchi, *Bit storage and bit flip operations in an electromechanical oscillator*, Nature Nanotechnol. **3**, 275 (2008).

[7] S. Rutzel, S. Lee, and A. Raman, *Nonlinear dynamics of atomic-force-microscope probes driven in Lennard-Jones potentials*, Proc. R. Soc. London Ser. A **459** (2003).

[8] D. Müller, D. Fotiadis, S. Scheuring, S. Müller, and A. Engel, *Electrostatically balanced subnanometer imaging of biological specimens by atomic force microscope*, Biophys. J. **76**, 1101 (1999).

[9] N. Kacem, J. Arcamone, F. Perez-Murano, and S. Hentz, *Dynamic range enhancement of nonlinear nanomechanical resonant cantilevers for highly sensitive NEMS gas/mass sensor applications*, J. Micromech. Microeng. **20**, 045023 (2010).

[10] M. R. M. Crespo da Silva and C. C. Glynn, *Nonlinear Flexural-Flexural-Torsional Dynamics of Inextensional Beams. I. Equations of motion*, J. Struct. Mech. **6**, 437 (1978).

[11] A. H. Nayfeh and D. T. Mook, *Nonlinear oscillations* (Wiley, 1995).

[12] S. N. Mahmoodi and N. Jalili, *Non-linear vibrations and frequency response analysis of piezoelectrically driven microcantilevers*, Int. J. Non-Linear Mech. **42**, 577 (2007).

[13] T. Ono, Y. Yoshida, Y.-G. Jiang, and M. Esashi, *Noise enhanced sensing of light and magnetic force based on a nonlinear silicon microresonator*, Appl. Phys. Express **1** (2008).

[14] S. Atluri, *Nonlinear Vibrations of a Hinged Beam Including Nonlinear Inertia Effects*, ASME Trans. J. Appl. Mech. **40**, 121 (1973).

[15] W. J. Venstra and H. S. J. van der Zant, *Efficient readout of micromechanical resonator arrays in ambient conditions*, Appl. Phys. Lett. **93**, 234106 (2008).

[16] D. S. Greywall, B. Yurke, P. A. Busch, A. N. Pargellis, and R. L. Willet, *Evading Amplifier Noise In Nonlinear Oscillators*, Phys. Rev. Lett. **72**, 2992 (1994).

[17] I. Siddiqi, R. Vijay, F. Pierre, C. Wilson, M. Metcalfe, C. Rigetti, L. Frunzio, and M. Devoret, *RF-driven Josephson bifurcation amplifier for quantum measurement*, Phys. Rev. Lett. **93**, 207002 (2004).

[18] L. Gammaitoni, P. Hanggi, P. Jung, and F. Marchesoni, *Stochastic resonance*, Rev. Mod. Phys. **70**, 223 (1998).

[19] R. Almog, S. Zaitsev, O. Shtempluck, and E. Buks, *Signal amplification in a nanomechanical Duffing resonator via stochastic resonance*, Appl. Phys. Lett. **90**, 013508 (2007).

[20] S. Perisanu, T. Barois, A. Ayari, P. Poncharal, M. Choueib, S. T. Purcell, and P. Vincent, *Beyond the nonlinear and Duffing regimes in nanomechanics: circularly polarized mechanical resonances of nanocantilevers*, Phys. Rev. B **81**, 165440 (2010).

4

STOCHASTIC SWITCHING

The cantilever is a prototype of a highly compliant mechanical system and plays an instrumental role in nanotechnology, enabling surface microscopy [1, 2], and ultrasensitive force[3, 4] and mass measurements[5, 6]. Here, we report fluctuation-induced transitions between two stable states of a strongly driven microcantilever. Geometric nonlinearity gives rise to an amplitude-dependent resonance frequency and bifurcation occurs beyond a critical point. The cantilever response to weak parametric modulations is amplified by white noise, resulting in an optimum signal-to-noise ratio at finite noise intensity. These findings suggest new detection schemes for cantilever-based instrumentation, where the detection of weak signals is mediated by the noisy environment. For ultrafloppy cantilevers with nanometer-scale dimensions operating at room temperature, a new transduction paradigm emerges that is based on probability distributions and mimics nature.

4.1 INTRODUCTION

ATOMIC force microscopy cantilevers enable imaging and modification of surfaces at the atomic level [1], imaging of electron and nuclear spins [2, 4], and measurement of the unfolding dynamics of single molecules [7]. Cantilevers are also used in solid-state nanofabrication [8, 9] and to dispense liquid volumes at the attoliter scale [10, 11]. Microcantilever-based sensors are promoted as a platform for multiplexed label-free detection of (bio) chemical species, by specific adsorption or individual weighing [3, 5, 6, 12–14]. These applications rely on measurement of the static deflections of the cantilever, or the changes in its response to weak periodic driving.

We study the dynamics of a microcantilever in the large-amplitude limit. The cantilever moves in a dynamic double-well landscape, where vibration states with a low- and a high-amplitude are stable. We show that the presence of noise leads to parametric excitation which enables transitions between the states. A rise and decay of the switching rate is observed when the noise intensity is increased. Close to the onset of spontaneous switching, the sensitivity of the cantilever to a weak excitation is enhanced, and the Signal-to-Noise Ratio (SNR) maximizes at finite noise intensity. This process is referred to as stochastic resonance, and has been reported in biological, physical, and information systems [15].

4.2 EXPERIMENT

Thin cantilevers with a rectangular cross section are fabricated by standard nanofabrication techniques, comprising low-pressure chemical vapor deposition of silicon nitride, patterning by electron beam lithography, and reactive ion etching. Figure 4.1(a) shows the device, with dimensions length × width × height ($L \times w \times h$)= $40 \times 8 \times 0.1\ \mu\text{m}^3$. The cantilever is driven by applying stochastic and harmonic voltages to a piezo actuator, at a pressure of $\sim 10^{-5}$ mbar. Its motion is detected by an optical deflection technique and network and spectrum analysis of the photodiode currents is implemented in a digital signal processor. Figure 4.1(b) shows the experimental setup. The power spectral density (PSD) of the cantilever displacement near the fundamental resonance frequency, $f_0 = 88.9$ kHz, is measured when Gaussian distributed white noise is applied with a spectral amplitude, N_V, varying between 0 and $1.4 \cdot 10^{-3}$ V/$\sqrt{\text{Hz}}$. The effective temperature of the fundamental mode is determined as a function of the applied noise voltage by integrating the PSD of the mechanical displacements (see Sec. 4.5.2). For $N_V > 10^{-4}$ V/$\sqrt{\text{Hz}}$ the applied noise exceeds the thermomechanical fluctuations. As expected, the energy of the mode is then proportional to the squared noise voltage; the calibrated effective temperature of the fundamental mode equals $T_{\text{eff}} = [4.8 \cdot 10^{11}\ \text{V}^{-2}\text{sK}] \cdot N_V^2$.

The nonlinear dynamics of the cantilever driven by a force f at frequency Ω is

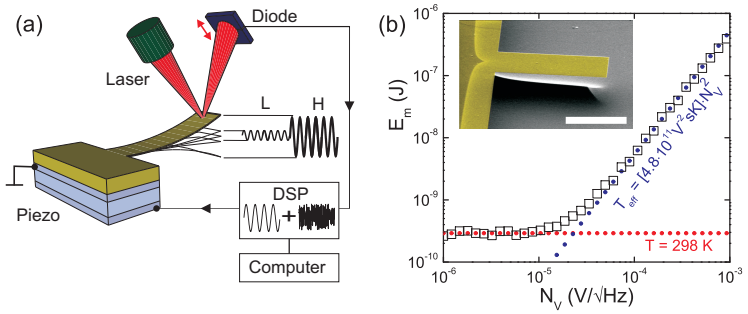

FIGURE 4.1: Setup and thermometry of a noise driven cantilever. (a) Diagram of measurement circuit. The cantilever is driven by stochastic and harmonic voltages generated in the Digital Signal Processor (DSP) and applied to the piezoelectric crystal. Its motion is detected optically. Details on the fabrication and the setup are provided in Supplementary Section 1. At strong driving, two distinct states are stable which correspond to a low (L) and a high (H) vibrational amplitude. (b) Inset: Colorized scanning electron micrograph of a silicon nitride cantilever (scale bar 20 μm). Measured energy $E_m = \int_\omega S_{xx}(\omega')d\omega'$ as a function of the applied noise N_V. When $N_V < 2.5 \cdot 10^{-5}\,V/\sqrt{Hz}$ the energy equals the thermomechanical noise. Increasing N_V yields the quadratic dependence between effective mode temperature and the applied noise voltage according to $T_{eff} = [4.8 \cdot 10^{11} V^{-2} sK] \cdot N_V^2$.

governed by

$$\ddot{a} + \eta\dot{a} + \omega^2 a + 40.44\delta a^3 + 4.60\delta(a\dot{a}^2 + a^2\ddot{a}) = -0.78 f\Omega^2 \cos(\Omega t), \tag{4.1}$$

where a is the scaled displacement, ω is the dimensionless resonance frequency (ω = 3.52) and δ the aspect ratio $(h/L)^2$. The fourth and fifth term represent geometric and inertial nonlinearities of the cantilever, causing the resonance frequency to increase with the vibration amplitude, as is discussed in more detail in Sec. 4.6. Note that in contrast to doubly-clamped beams, where the nonlinearity originates from the displacement-induced tension, a cantilever is clamped on one side and therefore it can displace without extending. This makes the cantilever highly susceptible to thermal fluctuations. At a critical amplitude and frequency, a_{cr} and f_{cr} respectively, a bifurcation occurs [16]. Two stable states coexist beyond this point, represented by motion at a low and a high vibrational amplitude [16–18]. A full map of the parameters that result in a bistable response is given in Sec. 4.6. The drive force fluctuations at finite temperature induce switching, which can be viewed as fluctuation-induced transitions between the attractors in the dynamic double-well[19, 20].

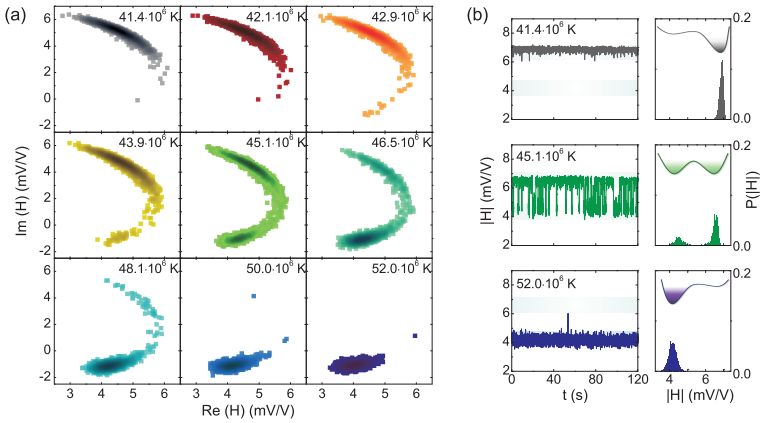

FIGURE 4.2: Stochastic switching of microcantilever motion. (a) Dynamics of the noise-driven microcantilever represented in the complex plane. The cantilever moves from the high to the low-amplitude attractor while increasing the noise power; the corresponding effective temperatures are indicated (upper left to lower right panel). Incoherent transitions occur at intermediate noise levels on the central row. (b) Time domain representation and probability densities (P) of the resonator amplitude response ($|H|$) for selected panels from each row. The shape of the dynamic double-well is sketched in the inset. The central panel represents the symmetric system.

4.3 NOISE-INDUCED SWITCHING

To study the noise-enabled transitions in the dynamic double-well, we prepare the cantilever in the high state and artificially increase its temperature by applying voltage noise to the piezo. Figure 4.2(a) shows the real and the imaginary part of the motion for nine different noise powers, which are expressed in the effective temperature of the fundamental mode. The cantilever is driven at an amplitude $a_d = 2.18a_{cr}$ and a frequency $f_d = 1.00066f_{cr}$. For $T_{\text{eff}} < 41 \cdot 10^6$ K the cantilever resides in the high-amplitude state (upper left panel): no switching is observed within the measurement time (120 s). When the noise intensity is raised, in the subsequent panels, the cantilever occasionally crosses the barrier. At $T_{\text{eff}} = 45 \cdot 10^6$ K, the central panel, the high- and the low-amplitude state are equally probable, and switching occurs through a narrow region in phase space [21]. The switching decays upon further increasing the noise intensity, and at $T_{\text{eff}} = 52 \cdot 10^6$ K the cantilever settles at the low-amplitude state. Figure 4.2(b) shows time traces (left) and histograms (right) of the amplitude response, clearly demonstrating the discrete states of low- and high-amplitude motion, and the transitions between them. The responses correspond to the first, central and the last panel in Fig. 4.2(a).

The transition rates and residence times are plotted in Fig. 4.3. The switching rate, shown in panel (a), rises according to Kramers law [22] upon increasing the noise intensity and maximizes to $\Gamma_{\text{max}} = 1.5\ \text{s}^{-1}$ at $T_{\text{eff}} = 44.9 \cdot 10^6$ K. In contrast to the saturation of the transition rate as is the case for a static double-well, a decay in the transition rate is observed upon increasing the noise level. Apparently, the applied noise presents an additional driving force which shifts the critical driving force a_{cr} to a lower value and makes transitions to the low-amplitude state more probable when the noise is increased. This parametric change becomes evident when the cantilever response to forward and backward frequency sweeps is measured at a low and a high noise intensity. Comparing the responses shown in Figure 3c, two effects are visible: applying noise reduces the hysteresis, as is expected for a double-well energy potential, and as observed in dynamically bistable doubly-clamped beams as well [23]. In addition, the hysteretic regime shifts to a lower frequency and amplitude. This causes the system prepared in a dynamic double-well in the presence of weak fluctuations, as indicated by a white dot in Figure 3c, to become monostable when the noise intensity is increased (see Sec. 4.6). The change in the dynamic double-well parameters due to noise is confirmed by measurements on a different device, discussed in Sec. 4.7. The present experiment indicates that, in contrast to a static double-well energy landscape, the stochastic switching between stable states in the dynamic double-well occurs in a limited regime of noise powers.

Noise-enabled measurements, similar to the ones demonstrated in doubly-

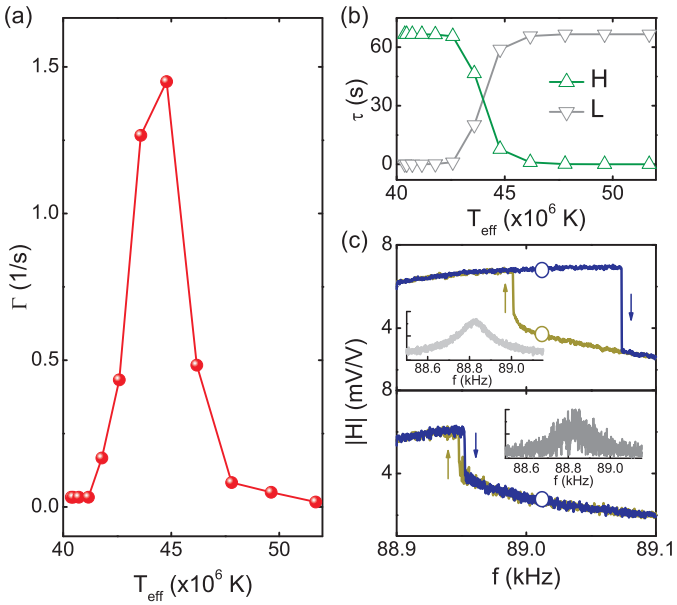

FIGURE 4.3: Transition rates and residence times. (a) Transition rate, Γ, as a function of temperature. (b) Residence time, τ, in the states of high-amplitude (H) and low-amplitude (L) motion. (c) Bistable frequency response lines of the cantilever measured at a low (upper curves) and a high (lower curves) temperature. The insets show the corresponding linear responses. Increasing the temperature affects the double-well: the initially bistable system, marked by the white circle, is monostable at a high noise intensity.

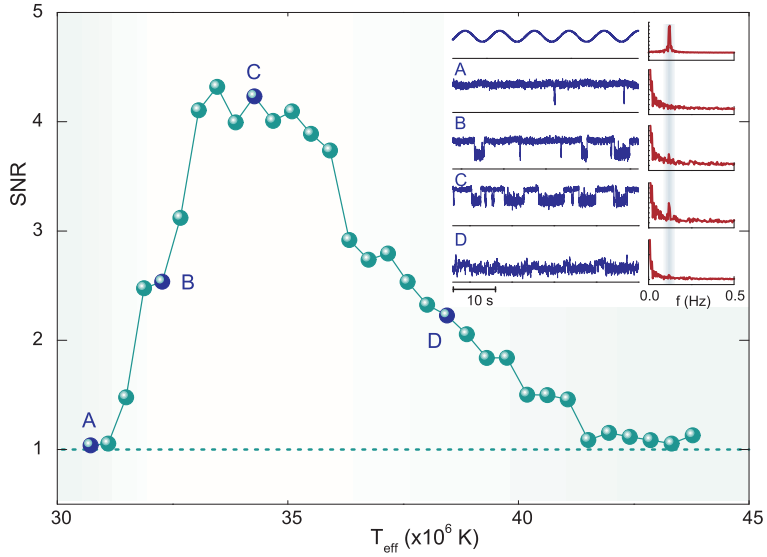

FIGURE 4.4: Noise-enhanced measurement of sub-threshold cantilever excitations. Inset: Top row shows the excitation signal in time (left) and frequency (right) domain. The cantilever response at increasing noise intensity is shown in panels A-D. Main figure: Signal-to-Noise ratio (SNR) as a function of the effective temperature (dotted line: SNR=1).

clamped beams [23–27] are now implemented in cantilevers, which are omnipresent in nanoscience instrumentation. The sensitivity of these instruments is ultimately limited by the thermomechanical fluctuations of the cantilever, and here we demonstrate a scheme that exploits such fluctuations. To demonstrate noise-enabled detection in a cantilever, the cantilever is prepared in a bistable state by driving it at $a_d = 1.5113\, a_{cr}$ and $f_d = 1.0013\, f_{cr}$. The double-well is then parametrically perturbed by a weak and slow sinusoidal amplitude modulation (amplitude 40 mV, period 10 s) of the periodic excitation signal on the piezo. This perturbation mimics, for instance, a small force to be detected by the cantilever-based instrument. Figure 4.4 (inset) shows the excitation voltage in the time and frequency domains (upper panels). Panels A-D show the response for four different noise intensities close to the regime where spontaneous switching occurs; the noise intensity increases from panel A to D. In panel A, the cantilever vibrates in the high state: the modulation of the double-well is too weak to cross the barrier, and only an incidental escape to the low-amplitude state is observed. In panel B, occasional transitions occur, weakly locked to the modulation signal. In C the transitions are synchronized to the modulation. Here, the amplification of the cantilever response by the noise is maximized. Further increasing the temperature shifts the double-well and directs the cantilever to the low state (D). A fast Fourier transform of the detected signals (Fig. 4.4 (inset), right column) clearly reveals the synchronization observed in panel C: the cantilever response peaks at the excitation frequency. The Signal-to-Noise Ratio (SNR) is calculated as [15]

$$\mathrm{SNR} = 2 \cdot \lim_{\Delta\omega \to 0} \int_{\omega-\Delta\omega}^{\omega+\Delta\omega} S(\omega')\mathrm{d}\omega' / N_V^2(\Omega) = \frac{S(\Omega)}{N(\Omega)}, \tag{4.2}$$

where $S(\Omega)$ is the height of the power spectrum peak at the modulation frequency Ω and $N(\Omega)$ is the spectral background. Figure 4.4 shows the SNR as a function of the temperature. A peak is observed at effective temperatures between $33 \cdot 10^6$ K and $35 \cdot 10^6$ K, where the random fluctuations induce coherence between the cantilever motion and the subthreshold excitation. In this experiment the SNR improves by a factor of 4 at the optimum noise level.

4.4 DISCUSSION AND CONCLUSION

The experiments described in this work are carried out at relatively high effective temperatures, obtained by artificially heating the mechanical system. In contrast to doubly-clamped structures such as silicon nitride strings, the amplitude of a cantilever is not restricted by the displacement-induced tension, and this makes large thermomechanical amplitudes possible. The limited dynamic range of NEMS resonators is a widely recognized disadvantage, and methods to enhance it are ac-

tively studied [18, 28, 29]. As the susceptibility of cantilever structures further increases upon scaling down the dimensions, in ultrathin cantilevers the thermal fluctuations will be strong enough to quench the regime of linear motion, leading to a dynamic range approaching zero and intrinsic bistability at room temperature. Clearly, mechanical devices in this regime require new operating paradigms, which involve probabilities and switching rates rather than the deterministic input-output relations of linear and weakly non-linear transducers. The present work demonstrates characteristic aspects of this new class of mechanical systems. At low temperatures, the Wigner function gives important information if the bistable cantilever is in the quantum regime [30].

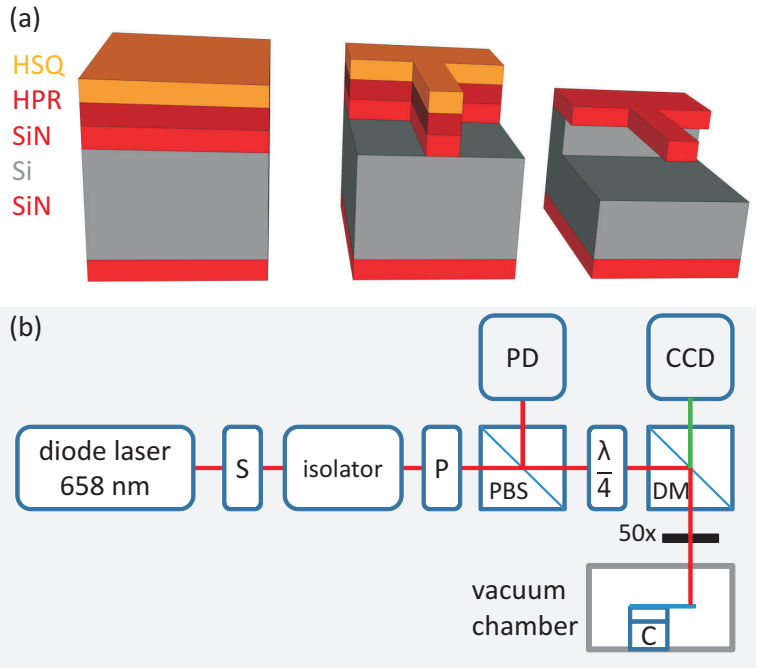

FIGURE 4.5: Experimental details. (a) Cantilever fabrication process. (b) Schematic of the optical deflection setup.

4.5 SUPPLEMENTARY INFORMATION

4.5.1 EXPERIMENTAL DETAILS

Cantilevers are fabricated according to the process shown in Fig. 4.5(a). An 100 nm thick layer of Low-Pressure Chemical Vapour Deposited silicon nitride [31, 32] is deposited on a silicon (1 0 0) wafer. A layer of photoresist is spin-coated (HPR, 0.5 μm), followed by HSQ electron-beam resist (Fox-12, 200 nm). Cantilevers are patterned in the HSQ layer using an electron beam pattern generator (Leica 5000+). The HPR is then anisotropically etched in a reactive ion etcher (LH Z400) using a low-pressure O_2 plasma (20 sccm, 0.3 μbar, 40 W). Subsequently the SiN is etched in a O_2/CHF_3 plasma (2.5 sccm, 50 sccm, 10 μbar) at 50 W, while the HPR serves as an etch mask. The cantilevers are released by under-etching the silicon substrate in an SF_6/O_2 inductively coupled plasma (Alcatel AMS100).

The cantilever motion is detected using the optical deflection technique shown

in Fig. 4.5(b). The collimated output of a diode laser passes a shutter (S), an isolator, a polarizer (P) and a Polarizing Beam Splitter (PBS), and is directed by the Dichroic Mirror (DM) through a microscope objective (NA=0.6, 50 ×, focal distance 11 mm) on the cantilever, which is placed on top of a piezo-electric crystal (C) in a vacuum chamber. The reflection is collected on a split-cell Photo Diode (PD).

Figure 4.6(a) shows the Power Spectral Density (PSD) of the detected voltage when the cantilever is driven by Gaussian distributed white noise. The effective temperature is determined by integrating the PSD over the frequency band of the fundamental mode. Figure 4.6(b) shows network analyzer measurements of the cantilever response driven by a periodic voltage. Clear signatures of a nonlinear response are observed at half the critical drive a_{cr}, and hysteresis and bistability occur when $a > a_{cr}$.

4.5.2 CANTILEVER MECHANICS

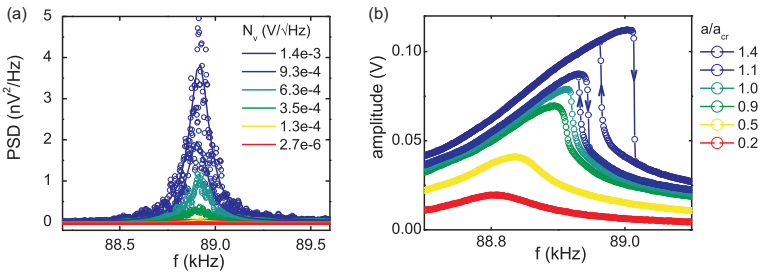

FIGURE 4.6: (a) Power Spectral Density (PSD) of the displacement noise of the 40 μm cantilever driven by broadband Gaussian white noise with a spectral amplitude equal to N_V. The solid lines are the Lorentzian fits from which the effective temperature is calculated. (b) Linear and nonlinear frequency responses of the cantilever driven by a sinusoidal voltage at indicated drive strengths. The arrows indicate the sweep direction. The critical driving amplitude a_{cr} marks the onset of hysteresis.

The theory of nonlinear oscillations of a cantilever beam due to geometric nonlinearity has been developed in Ref. [17]. Using the extended Hamilton principle the equation of motion for the displacement $\tilde{u}$ is written as:

$$D[\tilde{u}'''' + [\tilde{u}'(\tilde{u}'\tilde{u}'')']'] + \rho w h \ddot{\tilde{u}} + \tilde{\eta}\dot{\tilde{u}} + \frac{1}{2}\rho w h\left(\tilde{u}'\int_L^s \frac{\partial^2}{\partial \tilde{t}^2}\int_0^{s_1}(\tilde{u}')^2 ds_2 ds_1\right)' = \tilde{F}. \quad (4.3)$$

The dots and primes denote differentiation to time $\tilde{t}$ and the arc length s of the cantilever respectively; D is the bending rigidity, ρ the density, and $\tilde{\eta}$ is the damping parameter. The piezo actuator generates a displacement $U = d_{33}V\cos(\tilde{\Omega}t)$,

where V is the drive voltage and d_{33} the piezoelectric coefficient. The resulting force on the cantilever equals $\tilde{F} = \ddot{U}\rho wh = -\tilde{\Omega}^2\rho whd_{33}V\cos(\tilde{\Omega}t)$. Equation 4.3 is transformed to a dimensionless form by substituting $u = \tilde{u}/h$, $x = s/L$, $l = d_{33}V/h$, $\eta = \eta' L^4/(D\tau)$ and $\delta = (h/L)^2$. The time $\tilde{t}$ and drive frequency $\tilde{\Omega}$ are scaled using $\tau = L^2\sqrt{\rho wh/D}$. Applying the Galerkin procedure for the first mode ($u = a(t)\xi(x)$) gives

$$\ddot{a} + \omega^2 a + \eta\dot{a} + 40.44\delta a^3 + 4.60\delta(a\dot{a}^2 + a^2\ddot{a}) = -0.78f\Omega^2\cos(\Omega t) \tag{4.4}$$

Here, ω is the dimensionless resonance frequency; for the first mode $\omega = 3.52$. The cubic term in a represents the hardening geometric nonlinearity, and the quadratic term in a represents a nonlinear inertia which softens the frequency response [16, 18]. The nonlinearity is determined by the squared aspect ratio δ. The values 40.44, 4.60 and 0.78 are obtained by integrating the linear mode shapes, $\xi(x)$:

$$\int_0^1 \xi(x)(\xi(x)'(\xi(x)'\xi(x)'')')'\mathrm{d}x = 40.44,$$

$$\int_0^1 \xi(x)\mathrm{d}x = 0.78,$$

$$\int_0^1 \xi(x)(\xi'(x)\int_0^x\int_1^{x_1}\xi'(x_2)^2\mathrm{d}x_2\mathrm{d}x_1)'\mathrm{d}x = 4.60. \tag{4.5}$$

To solve equation 4.4, the fast timescale $(1/\Omega)$ is separated from the slow timescale (Q/Ω). The displacement is written as $a(t) = u_1(t)\cos(\Omega t) + u_2(t)\sin(\Omega t)$ and in-

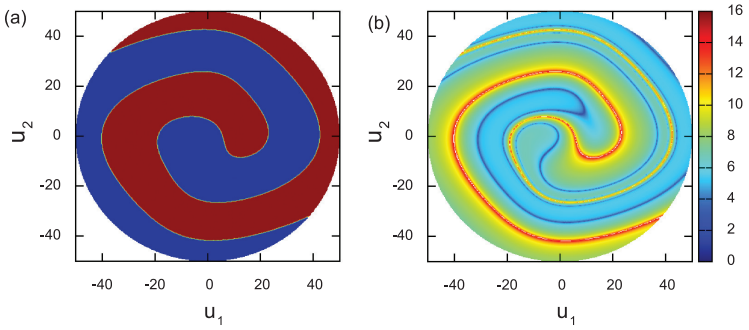

FIGURE 4.7: Basins of attraction of a cantilever, calculated by numerically solving equations (4,5). (a) If the cantilever is prepared with initial conditions in the red area, the motion evolves to the high-amplitude state. Initial conditions in the blue area evolve to the low-amplitude state. The attractors are located at (u_1,u_2) equals (-1.05, 1.05) and (-4.22, 4.87). (b) Traveling time (scaled by Q/ω) to the attractor. Time increases from blue to red; red marks the separatrix.

serted in equation 4.4. All terms moving faster than $1/\Omega$ are neglected. Collecting terms with $\cos(\Omega t)$ and $\sin(\Omega t)$ gives two equations of u_1 and u_2:

$$\dot{u_1} = \frac{1}{2}\left[\frac{\frac{-\omega}{Q}u_1 + \frac{\omega^2}{\Omega}u_2 + \left(\frac{30.33\delta}{\Omega} + 1.15\delta\Omega\right)(u_2^3 + u_1^2 u_2)}{1 + 2.30\delta(u_1^2 + u_2^2)} - \Omega u_2\right], \tag{4.6}$$

$$\dot{u_2} = \frac{1}{2}\left[\frac{\frac{-\omega}{Q}u_2 - \frac{\omega^2}{\Omega}u_1 + \left(\frac{30.33\delta}{\Omega} - 1.15\delta\Omega\right)(u_1^3 + u_1 u_2^2) - 0.78l\Omega}{1 + 2.30\delta(u_1^2 + u_2^2)} + \Omega u_1\right]. \tag{4.7}$$

Similar to the nonlinearity from the displacement-induced tension in doubly-clamped beams, the geometric nonlinearity in a cantilever can lead to a bistable frequency response [16, 33]. At sufficiently strong driving two attractors emerge: depending on the initial conditions the resonator evolves to a state of high or a state of a low-amplitude. Figure 4.7 shows the steady state as a function of the initial conditions (a), and the time it takes to evolve to that state (b). Here, the cantilever is driven at $a = 2.0a_{cr}$ and $f = 1.1f_{cr}$.

4.6 QUENCHING OF THE HYSTERETIC REGIME

The nonlinear equations of motion of the cantilever yield a multi-valued response for a regime of drive strengths and frequencies [16]. For the experimental device, this regime is visualized by measuring frequency response curves at a range of drive strengths, combined in Figure S4 for sweeps at increasing (a) and decreasing (b) frequency. Panel (c) shows the superimposed image, and marks the drive conditions that result in a bistable response. Repeating the experiment at a high effective temperature quenches the hysteretic regime as is shown in Fig. 4.8(d)-(f). Quenching of the hysteresis has been observed before in doubly-clamped nanomechanical resonators at effective temperatures on the order of 10^{10} K [23]. For the floppy cantilever devices in our experiment the hysteresis vanishes at temperatures that are lower by three orders of magnitude. For high noise powers we observe, in addition, a shift of the hysteretic regime. This indicates a noise-induced change to the double-well parameters, and suggests that the noise has a multiplicative character [34]. We note that a monostable state in the high noise limit was also observed in magnetomotive-driven doubly-clamped nanomechanical resonators [24].

4.7 MEASUREMENTS ON A DIFFERENT DEVICE

We conducted experiments on a second device with dimensions $L \times w \times h = 26 \times 8 \times 0.07\ \mu\text{m}^3$ in order to corroborate the results. For this device the resonance frequency and Q factor are $f_0 = 143.6$ kHz, Q_0=1537, and the effective temperature obtained by noise thermometry, cf. Fig 4.1(a), is given by T_{eff}=[$2.7 \cdot 10^{11}$ V^{-2}sK] ·

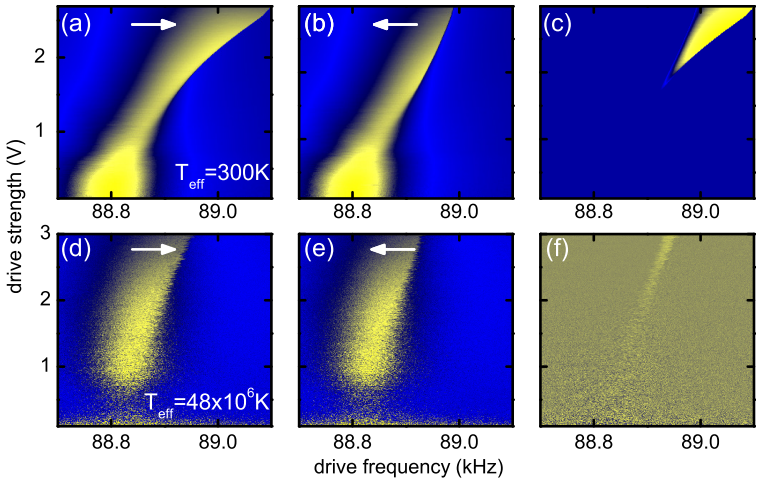

FIGURE 4.8: Maps of the parameter regime for a bistable response, taken at two noise intensities indicated as effective temperatures. Cantilever susceptibility (response magnitude normalized to the drive force) during forward (a) and reverse (b) frequency sweeps (horizontal, fast axis) for increasing drive strength (vertical, slow axis), taken at $T_{\text{eff}} = 300$ K. (c) shows the parameter map that leads to a bistable amplitude and is obtained by superimposing (a) and (b). Bifurcation occurs at the critical driving voltage $a_{cr} = 1.555$ V and frequency $f_{cr} = 88.925$ kHz. (d-f) The same measurement at an effective temperature $T_{\text{eff}} = 48 \times 10^6$ K, showing quenching of the hysteresis and a shift of the bistable regime.

N_V^2. The device is driven in the bistable regime at $a = 1.34 a_{cr}$ and $f = 1.00016 f_{cr}$, closer to the critical point than in the experiment described in the main text. As a result, the hysteretic regime is smaller, and noise-induced switching is observed at noise powers that are lower by two orders of magnitude. Figure 4.9(a) shows time traces and histograms of the cantilever response at three noise intensities, indicated by effective temperatures. For low noise levels, $T_{\text{eff}} < 10^5$ K, the cantilever vibrates in the low-amplitude state and no switching is observed within the time of the experiment (180 s). When the noise intensity is increased, switching occurs and at $T_{\text{eff}} = 27.1 \cdot 10^4$ K the states equally populated. As with the experiment in the main text, further increasing the noise level induces parametric changes to the double-well. At high noise levels the high state becomes more probable, as schematically represented in the insets.

Figure 4.9(b) shows the evolution of the histograms when the applied noise level is increased: in the high-noise limit the low-amplitude state that was initially stable, vanishes. In this case the fluctuations are strong enough to access the unstable state, as is indicated by the schematized double-wells inset in the his-

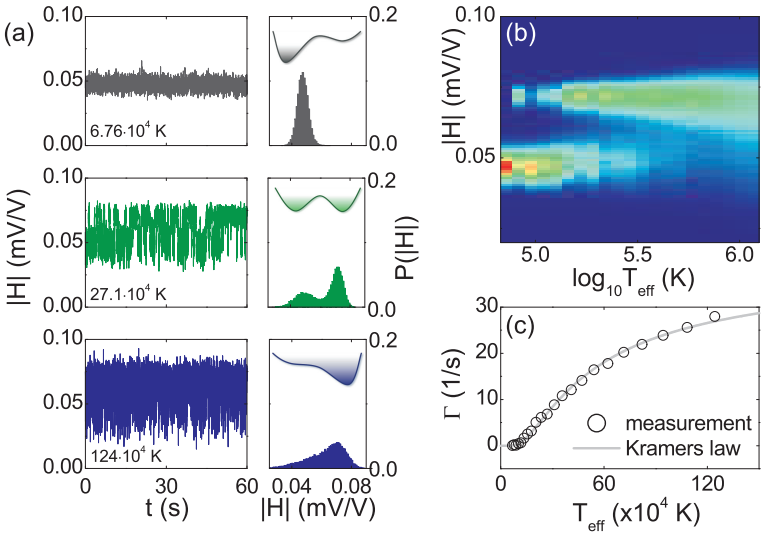

FIGURE 4.9: (a) Stochastic switching of a cantilever with dimensions $L \times w \times h = 26 \times 8 \times 0.07\ \mu\text{m}^3$. (b) Stacked histograms for a range of noise intensities (colorscale: P(|H|)). The transition from the low to the high-amplitude attractor suggests a qualitative change in the symmetry of the dynamic double-well. (c) The switching rate follows Kramers law for diffusion-driven escape.

tograms. As a result, the switching rate does not peak in this parameter regime, but continues to follow Kramers law [22] as is shown in Fig. 4.9(c), and which resembles the initial part of the curve in Fig. 4.3(a) in the main text.

Such behavior is predicted for a dynamic double-well [19], and was observed in doubly-clamped nanomechanical resonators and parametric oscillators [21, 23]. We conclude that in the limit of low noise, Kramers law effectively describes the stochastic switching of cantilever motion, and the switching rate is given by $\Gamma = \Gamma_0 e^{-T_0/T_{\text{eff}}}$, with $\Gamma_0 = 39\ \text{s}^{-1}$ and $T_0 = 4.6 \cdot 10^5\text{K}$ in the present experiment.

REFERENCES

[1] G. Binnig, C. F. Quate, and C. Gerber, *Atomic Force Microscope*, Phys. Rev. Lett. **56**, 930 (1986).

[2] A. C. Bleszynski-Jayich, W. E. Shanks, B. Peaudecerf, E. Ginossar, F. von Oppen, L. Glazman, and J. G. E. Harris, *Persistent Currents in Normal Metal Rings*, Science **326**, 272 (2009).

[3] J. Fritz, M. K. Baller, H. P. Lang, H. Rothuizen, P. Vettiger, E. Meyer, H. J. Guntherodt, C. Gerber, and J. K. Gimzewski, *Translating biomolecular recognition into nanomechanics*, Science **288**, 316 (2000).

[4] D. Rugar, R. Budakian, H. Mamin, and B. Chui, *Single spin detection by magnetic resonance force microscopy*, Nature **430**, 329 (2004).

[5] T. P. Burg, M. Godin, S. M. Knudsen, W. Shen, G. Carlson, J. S. Foster, K. Babcock, and S. R. Manalis, *Weighing of biomolecules, single cells and single nanoparticles in fluid*, Nature **446**, 1066 (2007).

[6] A. Boisen, S. Dohn, S. S. Keller, S. Schmid, and M. Tenje, *Cantilever-like micromechanical sensors*, Rep. Prog. Phys. **74**, 1 (2011).

[7] T. Hugel, M. Rief, M. Seitz, H. E. Gaub, and R. R. Netz, *Highly stretched single polymers: Atomic-force-microscope experiments versus ab-initio theory*, Phys. Rev. Lett. **94**, 048301 (2005).

[8] M. I. Lutwyche, M. Despont, U. Drechsler, U. Durig, W. Haberle, H. Rothuizen, R. Stutz, R. Widmer, G. K. Binnig, and P. Vettiger, *Highly parallel data storage system based on scanning probe arrays.*, Appl. Phys. Lett. **77**, 3299 (2000).

[9] A. Tseng, A. Notargiacomo, and T. Chen, *Nanofabrication by scanning probe microscope lithography: A review*, J. Vac. Sci. Techn. B **23**, 877 (2005).

[10] K. Salaita, Y. Wang, and C. A. Mirkin, *Applications of dip-pen nanolithography*, Nature Nanotechnol. **2**, 145 (2007).

[11] A. B. Braunschweig, F. Huo, and C. A. Mirkin, *Molecular printing*, Nature Chem. **1**, 353 (2009).

[12] R. McKendry, J. Zhang, Y. Arntz, T. Strunz, M. Hegner, H. Lang, M. Baller, U. Certa, E. Meyer, H. J. Guntherodt, et al., *Multiple label-free biodetection and quantitative DNA-binding assays on a nanomechanical cantilever arrays*, Proc. Nat. Acad. Sci. **99**, 9783 (2002).

[13] M. Yue, H. Lin, D. E. Dedrick, S. Satyanarayana, A. Majumdar, A. S. Bedekar, J. W. Jenkins, and S. Sundaram, *A 2-D Microcantilever Array for Multiplexed Biomolecular Analysis*, J. Microelectromech. S. **13**, 290 (2004).

[14] M. Li, E. B. Myers, H. X. Tang, S. J. Aldridge, H. C. McCaig, J. J. Whiting, R. J. Simonson, N. S. Lewis, and M. L. Roukes, *Nanoelectromechanical Resonator Arrays for Ultrafast, Gas-Phase Chromatographic Chemical Analysis*, Nano Lett. **10**, 3899 (2010).

[15] L. Gammaitoni, P. Hanggi, P. Jung, and F. Marchesoni, *Stochastic resonance*, Rev. Mod. Phys. **70**, 223 (1998).

[16] W. J. Venstra, H. J. R. Westra, and van der Zant HSJ, *Mechanical stiffening, bistability, and bit operations in a microcantilever*, Appl. Phys. Lett. **97**, 193107 (2010).

[17] M. R. M. Crespo da Silva and C. C. Glynn, *Nonlinear Flexural-Flexural-Torsional Dynamics of Inextensional Beams. I. Equations of motion*, J. Struct. Mech. **6**, 437 (1978).

[18] N. Kacem, J. Arcamone, F. Perez-Murano, and S. Hentz, *Dynamic range enhancement of nonlinear nanomechanical resonant cantilevers for highly sensitive NEMS gas/mass sensor applications*, J. Micromech. Microeng. **20**, 045023 (2010).

[19] M. I. Dykman and M. A. Krivoglaz, *Theory of fluctuational transitions between stable states of a nonlinear oscillator*, Zh. Eksp. Teor. Fiz **77**, 60 (1979).

[20] M. I. Dykman, *Fluctuating nonlinear oscillators* (Oxford University Press, 2012).

[21] H. B. Chan, M. I. Dykman, and C. Stambaugh, *Paths of Fluctuation Induced Switching*, Phys. Rev. Lett. **100**, 130602 (2008).

[22] H. A. Kramers, *Brownian motion in a field of force and the diffusion model of chemical reactions*, Physica **7**, 284 (1940).

[23] J. Aldridge and A. Cleland, *Noise-Enabled Precision Measurements of a Duffing Nanomechanical Resonator*, Phys. Rev. Lett. **94**, 156403 (2005).

[24] R. Badzey and P. Mohanty, *Coherent signal amplification in bistable nanomechanical oscillators by stochastic resonance*, Nature **437**, 995 (2005).

[25] R. Almog, S. Zaitsev, O. Shtempluck, and E. Buks, *Signal amplification in a nanomechanical Duffing resonator via stochastic resonance*, Appl. Phys. Lett. **90**, 013508 (2007).

[26] D. N. Guerra, T. Dunn, and P. Mohanty, *Signal Amplification by 1/fNoise in Silicon-Based Nanomechanical Resonators*, Nano Lett. **9**, 3096 (2009).

[27] Q. P. Unterreithmeier, T. Faust, and J. P. Kotthaus, *Nonlinear switching dynamics in a nanomechanical resonator*, Phys. Rev. B **81**, 241405 (2010).

[28] I. Kozinsky, H. W. C. Postma, I. Bargatin, and M. L. Roukes, *Tuning nonlinearity, dynamic range, and frequency of nanomechanical resonators*, Appl. Phys. Lett. **88**, 253101 (2006).

[29] H. J. R. Westra, M. Poot, H. S. J. van der Zant, and W. J. Venstra, *Nonlinear modal interactions in clamped-clamped mechanical resonators*, Phys. Rev. Lett. **105**, 117205 (2010).

[30] I. Katz, A. Retzker, R. Straub, and R. Lifshitz, *Signatures for a classical to quantum transition of a driven nonlinear nanomechanical resonator"*, Phys. Rev. Lett. **99**, 040404 (2007).

[31] P. French, P. Sarro, R. Mallee, E. Fakkeldij, and R. Wolffenbuttel, *Optimization of a low-stress silicon nitride process for surface-micromachining applications.*, Sensor Actuat. A - Phys **58**, 149 (1997).

[32] K. Babaei Gavan, E. W. J. M. van der Drift, W. J. Venstra, M. R. Zuiddam, and H. S. J. van der Zant, *Effect of undercut on the resonant behaviour of silicon nitride cantilevers*, J. Micromech. Microeng. **19**, 035003 (2009).

[33] H. J. R. Westra, H. S. J. van der Zant, and W. J. Venstra, *Modal interactions of flexural and torsional vibrations in a microcantilever*, Ultramicroscopy **120**, 41 (2012).

[34] M. Gitterman, *The noisy oscillator: the first hundred years, from Einstein until now* (World Scientific Publishing Company, 2005).

5

MODAL INTERACTIONS IN CLAMPED-CLAMPED RESONATORS

A theoretical and experimental investigation is presented on the intermodal coupling between the flexural vibration modes of a single clamped-clamped beam. Nonlinear coupling allows an arbitrary flexural mode to be used as a self-detector for the amplitude of another mode, presenting a method to measure the energy stored in a specific resonance mode. At strong driving forces, experiments demonstrate complex nonlinear dynamics of the coupled modes. The observed complex dynamics are quantitatively captured by a model based on coupling of the modes via the beam extension; the same mechanism is responsible for the well-known Duffing nonlinearity in clamped-clamped beams.

Parts of this chapter have been published in Phys. Rev. Lett. **105**, 117205 (2010) [1].

5.1 INTRODUCTION

An important topic in nanomechanics is the motion detection of mechanical resonators. Several schemes have been proposed to attain sensitivities near the quantum limit of mechanical motion [2], whereas application-driven research is focussed on on-chip detection [3] and readout of resonator arrays [4]. Central in any detection scheme is the coupling of a mechanical resonator to another system, which transduces the motion into a measurable quantity. Examples of sensitive detectors include a single-electron transistor [5], a microwave cavity [6], or an optical interferometer [7]. A second mechanical resonator can also be used to detect the motion of the resonator [8, 9]. Such a system of coupled resonators has been proposed as a quantum nondemolition detection scheme, in which one resonator is in a quantum state [10]. Coupling between different mechanical resonators is often present in large-scale integrated arrays due to electrostatic [8] and mechanical interaction [9]. Coupling between individual resonators can also lead to complex behavior [11].

In this Chapter, we study the coupling between vibrational modes in a *single* beam resonator. We demonstrate that flexural modes are coupled by the displacement-induced tension in the beam. Using this coupling, the displacement of any mode can be detected by measuring the response of another mode, making otherwise undetectable modes visible. We present a general theoretical framework based on the Euler-Bernoulli equation extended with displacement-induced tension. The model quantitatively describes the complex dynamic behavior observed in the regime where two modes are simultaneously driven nonlinear. The coupling mechanism plays an prominent role in the dynamics of carbon nanotube resonators and resonators under high tension, and should be taken into account when describing such systems accurately.

5.2 MEASURING MODAL INTERACTIONS

Experiments are performed on a single-crystalline silicon beam with dimensions $L \times w \times h = 1000 \times 35 \times 6\ \mu\text{m}^3$ fabricated by patterning a silicon-on-insulator wafer and subsequent wet etching. The resonator is placed in a magnetic field of $B = 2.1$ T and a magnetomotive technique [4, 12] is used to detect the mechanical motion of the beam at room temperature and atmospheric pressure [see Fig. 5.1(a)]. The beam is driven at multiple frequencies by sending alternating currents through a conductive aluminum path, evaporated on top of the resonator. The motion of the beam in the magnetic field generates an electromotive force, which is balanced using a Wheatstone bridge, amplified, and then digitized. The frequency response (amplitude and phase) of the resonator at the two drive frequencies is calculated using a digital signal processor.

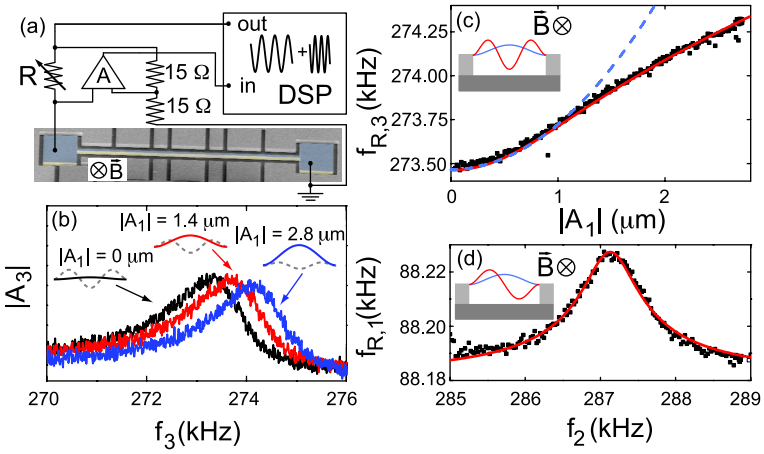

FIGURE 5.1: (a) Setup, with a colored scanning electron micrograph of the resonator beam. DSP is the digital signal processor, R is used to balance the bridge and set to 22 Ω and A is the amplifier. (b) Frequency responses of the third mode (amplitude $|A_3|$) for different drive amplitudes of the first mode $|A_1|$ on resonance. The drive current of mode 3 is I_3 = 1.5 mA. Inset: beam shapes of the first (solid) and third mode (dashed) for increasing amplitude of the first mode. (c) Resonance frequency of mode 3 ($f_{R,3}$) as a function of drive amplitude of $|A_1|$: measurements (black squares) and model (red line). For small drive currents a quadratic dependence is observed (dashed blue line). Inset: schematic of the resonator showing the beam shape of the first (blue) and third (red) mode. (d) On a different device, the resonance frequency of the first mode is used to detect the second mode. Inset: beam shape of the first (blue) and second (red) mode. The error bars are within data markers.

Measurements are conducted on the first and third flexural mode of the beam. In Fig. 5.1(b) the frequency response of the third mode is shown for three different drive amplitudes of the first mode. The resonance frequency of the third mode increases when the amplitude of the first mode $|A_1|$ becomes larger. At the same time the amplitude decreases slightly. The resonance frequency $f_{R,3}$, obtained by fitting a damped driven harmonic oscillator response, is plotted as a function of the drive amplitude of the first mode in Fig. 5.1(c). For small amplitudes $|A_1|$, a quadratic dependence of $f_{R,3}$ on $|A_1|$ is found [dashed line in Fig. 5.1(c)]. A qualitative picture explaining the mode coupling is presented in Figure 5.1(b). When driving the third mode on resonance, the tension in the beam increases as the amplitude of the first mode increases. This results in a higher frequency and a lower amplitude of the third mode.

Using the magnetomotive measurement scheme it is not possible to detect the even resonance modes. However, by exploiting the coupling to detectable odd

modes, their motion is observable. We have detected the motion of the second mode by measuring its influence on the first mode. To drive the second mode, the sample (different device, $h = 10\ \mu$m) is mounted on a piezo actuator and excited at frequencies around the second resonance mode. Off-resonance, no frequency shift of the first mode is observed. When driven at $f_{R,2}$, $f_{R,1}$ shifts to a higher value [Fig. 5.1(d)]. The response of the second mode is obtained by measuring the shift in $f_{R,1}$, whereas a magnetomotive measurement around the same frequency shows no signature of the second mode. For weak piezo driving the frequency shift is proportional to $|A_2|^2$ and a squared damped driven harmonic oscillator function fits the data well with $f_2 = 287$ kHz and $Q = 250$.

5.3 THEORY OF MODAL INTERACTIONS

In order to quantify the coupling between the flexural modes of the beam, an analytical model is developed. First, the equations are derived for the general situation with modes coupled; then we focus on the experimental situation, where only two modes are considered. The Euler-Bernoulli equation including tension $\mathcal{T}$ [13–15] is used as starting point. To simplify the notation, the displacement u is scaled with the beam thickness h, and the coordinate x with the beam length L. A displacement of the beam causes an elongation and increases the tension. The dimensionless tension $T = L^2\mathcal{T}/D$ (D is the bending rigidity) is given by

$$T = T_0 + \frac{\tau}{2}\int_0^1 \left(\frac{\partial u}{\partial x}\right)^2 \mathrm{d}x. \tag{5.1}$$

T_0 is the residual tension in the beam and $\tau = h^2 A/I_y$, with I_y the second moment of inertia and A the cross-section. For a rectangular beam τ equals 12 [16]. The displacement u and dimensionless force $F = L^4\mathcal{F}/Dh$ can be split into a dc and an ac part i.e., $u = u_{dc} + u_{ac}$ and $F = F_{dc} + F_{ac}$. This yields a well-known equation for the static displacement [13–15] and an equation for the ac motion:

$$\ddot{u}_{ac} + \eta\dot{u}_{ac} + \mathscr{L}[u_{ac}] - (T - T_{dc})u''_{ac} - (T - \overline{T} - T_{ac})u''_{dc} = F_{ac}. \tag{5.2}$$

Here, T_{dc} is the residual tension plus the tension from the dc displacement and $\overline{T}$ is the time-averaged tension, which also contains terms proportional to u_{ac}^2. For small ac displacements $\overline{T} \approx T_{dc}$. T_{ac} contains all terms that are linear in u_{ac}. The operator $\mathscr{L}[u]$ is defined as [15]

$$\mathscr{L}[u] = u'''' - T_{dc}u'' - T_{ac}[u]u''_{dc}. \tag{5.3}$$

The first three terms on the left side of Eq. 5.2 determine the linear response of the system. The nonlinearity is introduced with u_{ac}^2 and u_{ac}^3, which occur in the last two terms.

The resonance frequency for infinitesimal small amplitudes $\omega_{0,i}^2$ and the corresponding shape $\xi_i(x)$ of mode i are the eigenvalues and orthonormal eigenfunctions of $\mathscr{L}$ respectively. The ac displacement is expanded in terms of the mode shapes as $u_{\mathrm{ac}} = \sum_{i=1}^{\infty} u_i(t)\xi_i(x)$. The dc displacement is defined as $u_{\mathrm{dc}} \equiv u_0\xi_0(x)$ and $\int_0^1 \xi_i'(x)\xi_j'(x)\mathrm{d}x$ is denoted as I_{ij}. The value of the integral I_{ij} depends only on the shapes of mode i and j and and can be calculated numerically. Using this notation the tension T is

$$T(t) = T_0 + \frac{\tau}{2}\sum_{i,j=0}^{\infty} u_i(t)u_j(t)I_{ij}, \tag{5.4}$$

so that $T_{\mathrm{dc}} = T_0 + \frac{\tau}{2}u_0^2 I_{00}$ and $T_{\mathrm{ac}} = \frac{1}{2}\tau u_0 \sum_{n=1}^{\infty} u_n I_{n0}$. For nonzero amplitudes u_n the tension increases, tuning the resonance frequencies $\omega_{\mathrm{R},i}$ away from $\omega_{0,i}$. The effect of the resonance frequency on its own motion results in a Duffing equation (i.e., the resonance frequency increases with its own amplitude). Based on the same concept, the tuning of the resonance frequency due to the motion of other modes can be envisaged and this coupling is the central theme of this work.

The displacement of a beam, which is driven at frequencies ω_i is written as

$$u(x,t) = \sum_i |a_i|\xi_i(x)\cos(\omega_i t + \angle a_i), \tag{5.5}$$

where the $a_i = A_i/h$ are the complex amplitudes of the mode at ω_i. Substituting Eq. 5.5 into Eq. 5.4 gives an expression for the total tension. The two tension terms in the ac equation are given by

$$T - T_{\mathrm{dc}} = \frac{\tau}{2}\sum_{i>0}\left(\frac{1}{2}|a_i|^2 I_{ii} + \frac{u_0}{2}a_i e^{i\omega_i t}I_{0i} + \text{c.c.}\right) + (T - \overline{T} - T_{\mathrm{ac}}) \tag{5.6}$$

$$T - \overline{T} - T_{\mathrm{ac}} = \frac{\tau}{4}\sum_{i\neq j>0}\left(\frac{1}{2}a_i^2 e^{i2\omega_i t}I_{ii} + a_i a_j^* e^{i(\omega_i-\omega_j)t}I_{ij} + a_i a_j e^{i(\omega_i+\omega_j)t}I_{ij} + \text{c.c.}\right).$$

Here, c.c. stands for the complex conjugate of the term before c.c. in parentheses. The expressions for the tension, Eq. 5.6, are substituted in the equation of motion, Eq. 5.2. The time-averaged equation for the amplitude of mode i driven at frequency ω_i, is then given by

$$\sum_{i\neq j>0}\Big\{\Big(\omega_{0,i}^2 - \omega_i^2 + i\omega_i\omega_{0,i}/Q_i + \frac{\tau}{4}|a_i|^2 I_{ii}^2 + \frac{\tau}{4}\Big(|a_j|^2 I_{ii}I_{jj} + |a_j|^2 I_{ij}^2\Big)\Big)a_i - \int_0^1 F_{\mathrm{ac}}\xi_i \mathrm{d}x\Big\} = 0, \tag{5.7}$$

where $F_{ac} = L^4 \mathscr{F}_{ac}/Dh$ is the dimensionless ac force.So far, the analysis is valid for any flexural resonator. We now focus on the experimental situation where, unlike in buckled beams [14] and string-like resonators [17], the residual tension does not play a significant role, $T_0 = 0$. Moreover, the static displacement $u_0 = 0$, which may not be the case for carbon nanotube resonators [18], where a gate voltage induces a static displacement. We finally assume that the resonances are resolvable: $|\omega_{R,i} - \omega_{R,j}| \gg \omega_{R,i}/Q_i + \omega_{R,j}/Q_j$ for $i \neq j$. The homogeneous force per unit length on the beam is $\mathscr{F}_{ac} = BI$, where I is the current through the resonator.

To compare the model with the data in Fig. 5.1(c), we first extract the experimental values of the parameters. The resonance frequencies for the first and third mode are $f_1 = 48.2$ kHz and $f_3 = 273.4$ kHz, close to the predicted values of 46.1 and 249 kHz for a beam-like resonator. Their Q factors are $Q_1 = 41$ and $Q_3 = 172$. The values of I_{ij} determine the coupling strength: $I_{11} = 12.3$, $I_{33} = 98.9$ and $I_{13} = I_{31} = -9.7$. The average displacement of the modes per unit deflection, $\int_0^1 \xi_i(x)dx$, are 0.83 and 0.36 for mode 1 and 3 respectively. The model is solved numerically by calculating the amplitudes of the two modes self-consistently for the experimental conditions and without any free parameters. The calculated resonance frequency of the third mode as a function of the amplitude of the first mode is shown in Fig. 5.1(c). Excellent agreement is found between the observed frequency shift and the prediction by the model. For large amplitudes, the resonance frequency scales with $|A_1|^{2/3}$, indicating that the beam is in the strong bending regime [13]. For small $|A_1|$, the tuning is quadratic and the third mode can be used to detect the amplitude of the first mode with a sensitivity of 0.18 Hz nm^{-2}, which is determined from the quadratic curve in Fig. 5.1(c).

5.4 COMPLEX NONLINEAR DYNAMICS

To further test the consistency of our model, we study the complex dynamics of the coupled modes. When driving both modes nonlinear, interesting features are observed. In Fig. 5.2(a) the amplitude of the nonlinear first mode is plotted versus the driving frequencies f_1 and f_3. Simultaneously, the amplitude of the third mode is recorded [Fig. 5.2(b)]. The two modes interact with each other as the nonlinear line shape of one mode is reflected in the response of the other mode. Also a frequency response with two peaks, which is clearly different from a Duffing line shape, is observed as illustrated more clearly in Figs. 5.2(e) and 5.2(f). The two peaks arise from the bistable first mode, where two values for the amplitude are possible. These two amplitudes correspond to two values of the tension, which leads to two resonance frequencies of the third mode and to two peaks in its frequency response. The simulation with the parameters as stated above, reproduces all observed features in the amplitude of both modes [Figs. 5.2c) and 5.2(d)]. This

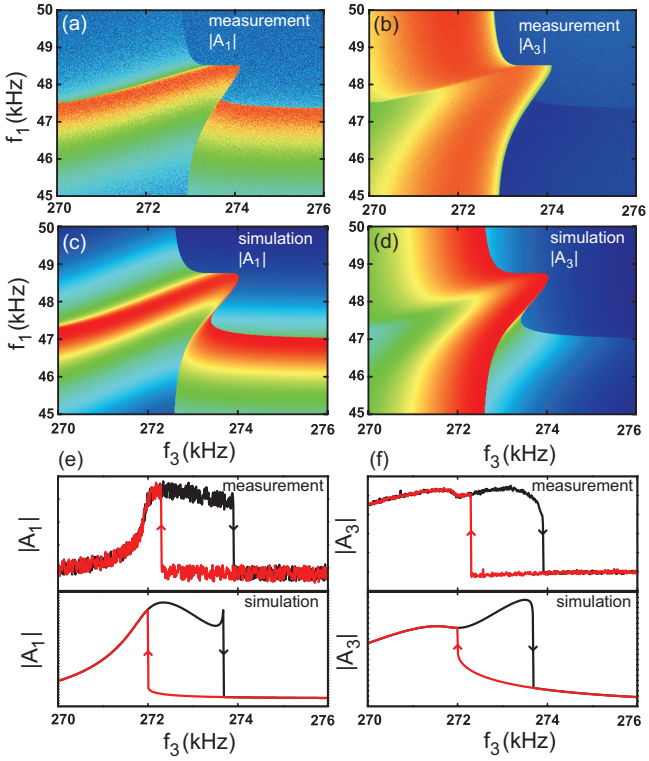

FIGURE 5.2: Frequency-frequency response of the simultaneously driven and detected first and third mode. The drive frequency of the third mode is swept, while driving the first mode at a fixed frequency. After each sweep the frequency of the first mode is increased. The amplitudes $|A_1|$ (a) and $|A_3|$ (b) are recorded. The driving currents are $I_1 = 0.8$ mA and $I_3 = 7.0$ mA. Red indicates a high amplitude and blue corresponds to a low-amplitude response. Simulations are shown in (c) and (d). The frequency response is plotted for the amplitude of mode 1 (e) and mode 3 (f) at $f_1 = 48$ kHz.

indicates that the model captures the coupling mechanism in detail [1].

5.5 DYNAMIC RANGE

An example of how the coupling between the modes can be used in practice is the increase in dynamic range of the mechanical resonator. In small-scale res-

[1] The measured responses show a small deviation from the simulated responses due to crosstalk in the measurement equipment.

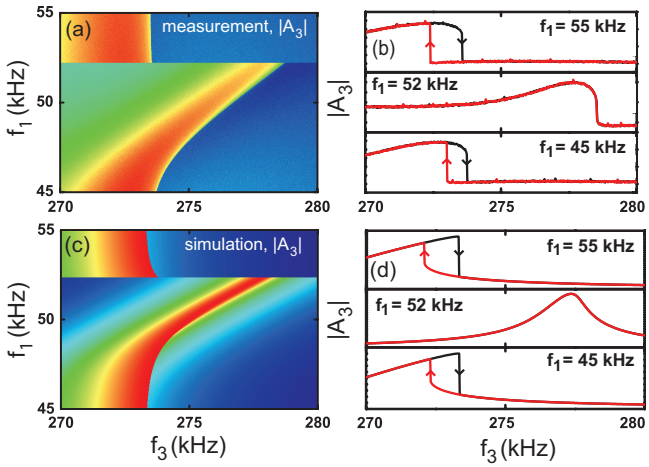

FIGURE 5.3: (a) Frequency-frequency plot for the forward sweep of the third mode. Red indicates a high amplitude and blue corresponds to a low amplitude. On resonance of the first mode, the third mode is linear and off-resonance it is nonlinear. (b) Forward (black lines) and back (red lines) below resonance, on resonance and above resonance, with $f_1 = 45, 52$ and 55 kHz respectively. Driving currents are $I_1 = 2$ mA and $I_3 = 8$ mA. (c) Result of the simulation with parameters extracted from the experiment. (d) Simulated responses for the situation in (b).

onators the dynamic range is limited by the nonlinear response at strong driving amplitudes, which is disadvantageous for many applications [19, 20]. Our analysis and experiments show that there is a way to extend the dynamic range of one mode by driving another mode on resonance at high amplitudes. Figures 5.3(a) and 5.3(c) show the frequency response of the third mode when the frequency of the first mode is swept across its nonlinear resonance. Away from $f_{R,1}$ the third mode shows a Duffing-like response as illustrated in the top and bottom panel of Figs. 5.3(b) and 5.3(d). However, when driving the first mode on resonance (middle panel) the third mode displays a hysteresis-free response. Effectively, the nonlinearity constant in the Duffing equation is decreased, which can be understood as follows: when the third mode enters its resonance, its amplitude increases and the increased tension tunes the resonance frequency of the first mode up. The amplitude of the first mode then drops, reducing the tension and lowering the resonance frequency of the third mode. This feedback mechanism reduces the cubic stiffness of the third mode and makes the third mode linear, thereby increasing the dynamic range.

5.6 DISCUSSION AND CONCLUSION

The presented model applies to any clamped-clamped geometry, ranging from suspended bridges to carbon nanotubes. For nanomechanical devices with high aspect ratios, the flexural rigidity can be neglected and the restoring force originates from the axial rigidity. The energy of the resonator is stored in the beam elongation which couples directly to the ac tension. This increases the coupling between the resonance modes and makes the detection mechanism well-suited for nanowires and nanotubes. Furthermore in nanomechanical devices, significant residual tension (T_0) may be present in the beam. Only the numerical values I_{ij} change in that case. For a resonator with high T_0, the off-diagonal elements $I_{ij} = 0$ and for mode 1 and 3, I_{11} is 9.9 and I_{33} is 88.8. Thus, for a string-like resonator the coupling term in Equation 5.7 remains within the same order of magnitude as in the beam resonator used in the experiment. To quantify the effect of modal interactions in a nanomechanical resonator with tension, we consider the suspended carbon nanotube with a high-quality factor from Ref. [21]. Taken the parameters listed in that paper, we calculate the sensitivity of the third mode to the amplitude of the first mode. We find a value of 1 MHz nm^{-2}, which is more than six orders of magnitude larger than the value found from the dashed line in Fig. 5.1(c).

In conclusion, we have measured the coupling between flexural modes of a clamped-clamped beam resonator by simultaneously driving the beam at multiple frequencies. We observe nonlinear interaction between the modes in the linear regime, and complex dynamics at large driving amplitudes. When describing the motion of a mechanical resonator, it is necessary to include this interaction, since this mechanism divides the available energy over the modes, and plays a role in the energy dissipation in the resonator. A theoretical model is developed, which couples arbitrary flexural modes via the tension. The model is in excellent agreement with the measurements and quantitatively captures the observed complex dynamics. The nonlinear coupling can be used to detect resonance modes that would otherwise be inaccessible by the experiment, to tune the nonlinearity constant, and to increase the dynamic range of micro- and nanomechanical resonators.

REFERENCES

[1] H. J. R. Westra, M. Poot, H. S. J. van der Zant, and W. J. Venstra, *Nonlinear modal interactions in clamped-clamped mechanical resonators*, Phys. Rev. Lett. **105**, 117205 (2010).

[2] K. C. Schwab and M. L. Roukes, *Putting mechanics into quantum mechanics*, Phys. Today **58**, 36 (2005).

[3] M. Li, H. X. Tang, and M. L. Roukes, *Ultra-sensitive NEMS-based cantilevers for sensing, scanned probe and very high-frequency applications*, Nature Nanotech. **2**, 114 (2007).

[4] W. J. Venstra and H. S. J. van der Zant, *Efficient readout of micromechanical resonator arrays in ambient conditions*, Appl. Phys. Lett. **93**, 234106 (2008).

[5] M. LaHaye, O. Buu, B. Camarota, and K. Schwab, *Approaching the quantum limit of a nanomechanical resonator*, Science **304**, 74 (2004).

[6] C. A. Regal, J. D. Teufel, and K. W. Lehnert, *Measuring nanomechanical motion with a microwave cavity interferometer*, Nature Phys. **4**, 555 (2008).

[7] T. Kippenberg and K. Vahala, *Cavity optomechanics: back-action at the mesoscale*, Science **321**, 1172 (2008).

[8] E. Buks and M. L. Roukes, *Electrically tunable collective response in a coupled micromechanical array*, J. of Microelectromech. Syst. **11**, 802 (2002).

[9] R. B. Karabalin, M. C. Cross, and M. L. Roukes, *Nonlinear dynamics and chaos in two coupled nanomechanical resonators*, Phys. Rev. B **79**, 165309 (2009).

[10] D. Santamore, A. Doherty, and M. Cross, *Quantum nondemolition measurement of Fock states of mesoscopic mechanical oscillators*, Phys. Rev. B **70**, 144301 (2004).

[11] R. Lifshitz and M. C. Cross, *Response of parametrically driven nonlinear coupled oscillators with application to micromechanical and nanomechanical resonator arrays*, Phys. Rev. B **67**, 134302 (2003).

[12] B. Yurke, D. Greywall, A. Pargellis, and P. Busch, *Theory of amplifier-noise evasion in oscillator employing a nonlinear resonator*, Phys. Rev. A **51**, 4211 (1995).

[13] S. Sapmaz, Y. M. Blanter, L. Gurevich, and H. S. J. .van der Zant, *Carbon nanotubes as nanoelectromechanical systems*, Phys. Rev. B **67**, 235414 (2003).

[14] A. H. Nayfeh, W. Kreider, and T. Anderson, *Investigation of natural frequencies and mode shapes of buckled beams*, AIAA J. **33**, 1122 (1995).

[15] M. Poot, B. Witkamp, M. A. Otte, and H. S. J. van der Zant, *Modelling suspended carbon nanotube resonators*, Phys. Stat. Sol. B **244**, 4252 (2007).

[16] A. N. Cleland, *Foundations of nanomechanics: from solid-state theory to device applications.* (Springer, 2003).

[17] S. S. Verbridge, H. G. Craighead, and J. M. Parpia, *A megahertz nanomechanical resonator with room temperature quality factor over a million*, Appl. Phys. Lett. **92**, 013112 (2008).

[18] V. Sazonova, Y. Yaish, Handel, Üstünel, D. Roundy, T. A. Arias, and P. L. Mceuen, *A tunable carbon nanotube electromechanical oscillator*, Nature **431**, 284 (2004).

[19] A. Kraus, A. Erbe, R. Blick, G. Corso, and K. Richter, *Parametric frequency tuning of phase-locked nanoelectromechanical resonators*, Appl. Phys. Lett. **79**, 3521 (2001).

[20] H. Postma, I. Kozinsky, A. Husain, and M. Roukes, *Dynamic range of nanotube- and nanowire-based electromechanical systems*, Appl. Phys. Lett. **86**, 223105 (2005).

[21] A. K. Hüttel, G. A. Steele, B. Witkamp, M. Poot, L. P. Kouwenhoven, and H. S. J. van der Zant, *Carbon Nanotubes as Ultrahigh Quality Factor Mechanical Resonators*, Nano Lett. **9**, 2547 (2009).

6

CANTILEVER FLEXURAL-TORSIONAL MODAL INTERACTIONS

The nonlinear interactions between flexural and torsional modes of a microcantilever are experimentally studied. The coupling is demonstrated by measuring the frequency response of one mode, which is sensitive to the motion of another resonance mode. The flexural-flexural, torsional-torsional and flexural-torsional modes are coupled due to nonlinearities, which affect the dynamics at high vibration amplitudes and cause the resonance frequency of one mode to depend on the amplitude of the other modes. We also investigate the nonlinear dynamics of torsional modes, which cause a frequency stiffening of the response. By simultaneously driving another torsional mode in the nonlinear regime, the nonlinear response is tuned from stiffening to weakening. By balancing the positive and negative cubic nonlinearities a linear response is obtained for the strongly driven system. The nonlinear modal interactions play an important role in the dynamics of multi-mode scanning probe microscopes.

Parts of this chapter have been published in Ultramicroscopy **120**, 41–47 (2012) [1].

6.1 INTRODUCTION

The Atomic Force Microscope (AFM) [2] is a crucial instrument in studying nanoscale objects. Various operation schemes are employed, which include the use of different cantilever geometries, higher modes or the torsional mode for imaging [3–6]. The nonlinear tip-sample interactions determine the dynamics in tapping-mode AFM and have been studied in detail [7, 8]. Besides this extrinsic nonlinearity, the intrinsic mechanical nonlinearities determine the dynamics of ultra-flexible microcantilevers at high amplitudes, as shown in a recent study [9]. These nonlinearities result in an amplitude-dependent resonance frequency and couple the vibration modes. In clamped-clamped beams, the nonlinear coupling is provided by the displacement-induced tension [10, 11]. For cantilever beams it was shown that the coupling between the modes can be used to modify the resonance linewidth [12]. In a multi-mode AFM [13, 14], these modal interactions are of importance, since the resonance frequency of one mode depends on the amplitude of the other modes.

In this Chapter, we experimentally demonstrate the intrinsic mechanical coupling between the flexural and torsional modes of a microcantilever. The resonance frequency of one mode depends on the amplitude of the other modes. The flexural modes are coupled via the geometric and inertial nonlinearities. The torsional modes exhibit frequency stiffening at high amplitudes, which originates from torsion warping [15]. Interestingly, the nonlinearity constant of one torsional mode changes sign when another torsional mode is driven at high amplitudes. Finally, the coupling between the torsional and flexural modes is studied.

6.2 EXPERIMENT

Microcantilevers are fabricated by photolithographic patterning of a thin low-pressure chemical vapor deposited silicon nitride (SiN) film. Subsequent reactive ion etching transfers the pattern to the SiN layer, and the cantilevers are released using a wet potassium hydroxide etch, resulting in a undercut-free cantilever. The dimensions are length × width × height ($L \times w \times h$) = $42 \times 8 \times 0.07$ μm^3. These floppy cantilevers allow high amplitudes and thus facilitate the study of nonlinearities. The cantilever is mounted onto a piezo actuator, which is used to excite the cantilever. The cantilevers are placed in vacuum (pressure < 10^{-5} mbar) to eliminate air-damping and to enable large vibration amplitudes, where nonlinear terms in the equation of motion dominate the dynamics. The cantilever motion is detected using a home-made optical deflection setup which resemblances the detection scheme frequently used in scanning probe microscopes. The flexural and torsional vibration modes are detected with a sensitivity of ± 1 pm/$\sqrt{\text{Hz}}$ [16]. A schematic of the measurement setup is shown in Fig. 1(a). The cantilever displacement sig-

nal is measured using either a network (NA) or spectrum analyzer (SA). To drive a second mode, a separate RF source is used.

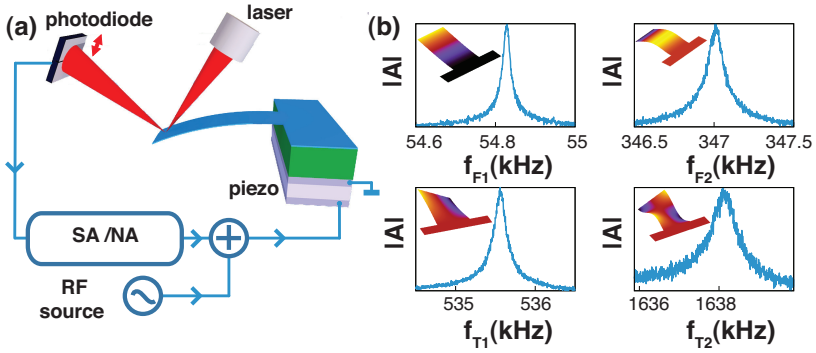

FIGURE 6.1: Measurement setup. (a) Optical deflection setup showing the laser beam, which reflects from the cantilever surface. The spot of the reflected laser beam is modulated in time by a frequency corresponding to the cantilever motion. The cantilever is mounted onto a piezo actuator in vacuum. Network (NA) and spectrum analysis (SA) is performed on the signal from the two-segment photodiode. (b) Frequency responses of the first and second flexural (top panels) and torsional (bottom panels) modes. Inset are the calculated mode shapes from Euler-Bernoulli beam theory.

First, the flexural vibrations are characterized by measuring the cantilever frequency response at different resonance modes. The first flexural mode shown in Fig. 1(b) occurs at 54.8 kHz with a Q-factor of 3000. The resonance frequency of the second mode is 347 kHz ($Q = 3900$), which is 6.33 times higher than the first resonance mode, in agreement with the calculated ratio $f_{R,F2}/f_{R,F1} = 6.27$, following from Euler-Bernoulli beam theory. Not shown is the third flexural mode at 974.9 kHz, with $f_{R,F3}/f_{R,F1} = 17.8$, near the expected ratio of 17.6. This indicates that in the linear regime the cantilever beam is described by the Euler-Bernoulli beam theory. Throughout the manuscript, the subscripts Fi and Ti indicate the frequency span around the i^{th} flexural (F) or torsional (T) resonance mode. The subscript R refers to the resonance frequency of that particular mode.

The torsional modes are characterized by rotating the cantilever over 90 degrees in the setup; the two-segment photodiode is then sensitive to vibrations corresponding to torsional resonance modes [16]. The frequency response of the first two torsional modes is shown in Fig. 1(b). From theory, the ratio between the lowest two resonance frequencies of the torsional modes is 3, which is close to the measured ratio of $f_{R,T2}/f_{R,T1} = 1638\,\text{kHz}/535.4\,\text{kHz} = 3.06$. The Q-factors of the first and second torsional mode are 4300 and 3200 respectively.

At high drive amplitudes, the flexural and torsional modes become nonlinear. The nonlinearity of the flexural modes in a cantilever beam was theoretically studied by Crespo da Silva in 1978 [17, 18]. To include the torsional nonlinearity, the equations of motion are extended (Appendix A). For the flexural and torsional modes, the nonlinearity causes a Duffing-like frequency stiffening when the mode is strongly driven [19, 20] leading to a bistable vibration amplitude. This bifurcation is observed in all modes studied in this paper. These nonlinearities are responsible for the coupling between the flexural-flexural, torsional-torsional and flexural-torsional modes.

6.3 MODAL INTERACTIONS IN A MICROCANTILEVER

We now experimentally demonstrate the coupling between the modes of a microcantilever. We use a two-frequency drive signal to excite two resonance modes of the cantilever simultaneously while we measure the motion of one mode. First, we focus on the interactions between the flexural modes. Then we turn our attention to the torsional modes, starting with the amplitude-dependent resonance frequency of the torsional vibrations, followed by the demonstration of the coupling between the lowest two torsional modes. Finally, the interactions between flexural and torsional modes are discussed.

6.3.1 FLEXURAL-FLEXURAL MODE INTERACTION

To investigate the interactions between the two lowest flexural modes, the thermal motion of the first mode is measured with a spectrum analyzer, while the RF source strongly drives the second mode. The thermal noise spectra of the first mode as a function of the drive frequency of the second mode are shown in Fig. 6.2(a). The color scale represents the power spectral density of the displacement around the resonance frequency of the first mode. A shift of the resonance peak of the first mode is observed as the drive signal at f_{F2} approaches the nonlinear resonance of the second mode. The resonance frequency of the first mode for each drive frequency of the second mode is obtained by fitting the damped-driven harmonic oscillator (DDHO) response. In Fig. 6.2(b), this resonance frequency of the first mode is plotted versus the drive frequency of the second mode. The nonlinear response of the second mode is reflected in the resonance frequency of the first mode where the resonance frequency first increases and then jumps down after the second mode has reached its maximum amplitude, indicated by the arrow. At the maximum amplitude of the second mode, the resonance frequency of the first mode is shifted by several times its linewidth. This experiment shows that the coupling between the flexural modes can introduce significant resonance frequency shifts when multiple modes are excited simultaneously. Moreover, by measuring

the shift in resonance frequency of the first mode the motion of the second mode can be detected. For comparison, the nonlinear response of the direct-driven second mode is shown in the inset of Fig. 6.2(b).

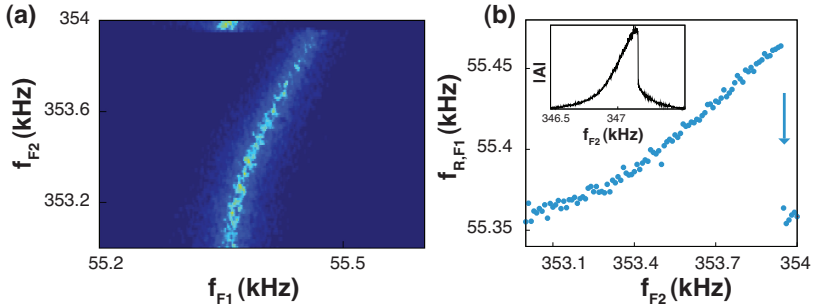

FIGURE 6.2: Flexural-flexural mode interactions. (a) Frequency spectra of the thermal motion of the first flexural mode (f_{F1}), when the second mode is driven through its resonance frequency. Color scale represents the power spectral density of the displacement noise of the first mode. As the peak width remains constant, there is no significant change in the Q-factor. The motion of the second mode tunes the resonance frequency of the first mode. (b) The resonance frequency of the first mode $f_{R,F1}$ versus the drive frequency of the second flexural mode. The nonlinear response of the second mode is reflected in the resonance frequency of the first mode. Inset: the direct measurement of the nonlinear second mode.

6.3.2 TORSIONAL-TORSIONAL MODE INTERACTION

Before turning to the interactions between the torsional vibration modes, we first measure the frequency response of a single torsional mode as a function of the drive strength. Although torsional modes are extensively used in AFMs [3, 21], their nonlinear behavior has not been investigated in detail. To investigate the nonlinearity, we strongly drive the torsional mode. In contrast to the flexural-flexural interactions, where the nonlinearity arises from geometric and inertial effects, in torsional modes, the nonlinearity originates from torsion warping and inertial moments [15]. In Appendix A we discuss the equations of motion including the nonlinearities involved. The amplitude of the first torsional mode with varying drive power is shown in Fig. 6.3(a), with selected frequency responses of the first torsional mode plotted in Fig. 6.3(b). At low driving power, the resonance line shape is a DDHO response, and the cantilever is oscillating in the linear regime. When the power is increased, the frequency response leans towards higher frequencies and the amplitude bifurcates. Close to this critical amplitude (0 dbm) the slope of the frequency response approaches infinity, which may be used to enhance the

sensitivity in torsional mode AFM. A frequency stiffening is observed for the first and second torsional mode.

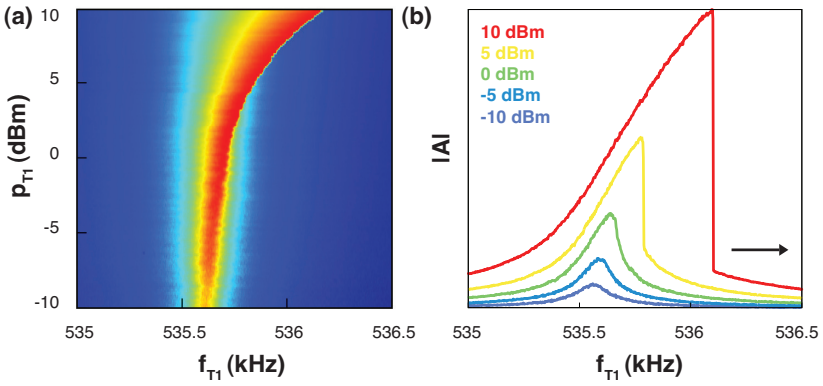

FIGURE 6.3: Nonlinear torsional mode. (a) Frequency responses of the first torsional mode, when the drive amplitude is increased. Beyond a power of 5 dBm, the response is bistable. Color scale indicates the amplitude normalized to the drive voltage. (b) Resonator amplitude traces at 5 selected drive powers. The nonlinear frequency response is visible at high drive powers. The frequency is swept from low to high.

Similar to the flexural-flexural modal interactions discussed in the previous section, the coupling between the first and second torsional modes is studied: we measure the thermal noise of the first mode while the drive power of the second torsional mode is varied. The resonance frequencies, obtained from DDHO fits to the thermal noise spectra of the first mode, are shown in Fig. 6.4(a). The resonance frequency increases with 500 Hz, while increasing the driving strength of the second mode to 10 dBm. We now perform a similar experiment as the one as shown in Fig. 6.2(b). Thus, the first torsional mode is used to detect the nonlinear vibrations of the second torsional mode. Fig. 6.4(b)) shows the nonlinear response, resembling the behavior of the first mode shown in Fig. 6.3(b).

Interesting behavior is observed when both torsional modes are driven in the nonlinear regime. In contrast to measurements in the previous section, the first mode is now also driven in the nonlinear regime. Fig. 6.5(a) shows the nonlinear frequency response of the first torsional mode, while stepping the drive frequency of the second torsional mode through its resonance. Fig. 6.5(b) shows individual traces, which reveal interesting behavior; in the lowest panel (i), there is no influence of the second mode and frequency stiffening of the first mode is observed cf. Fig. 6.3(b). When the amplitude of the second mode starts to increase as it ap-

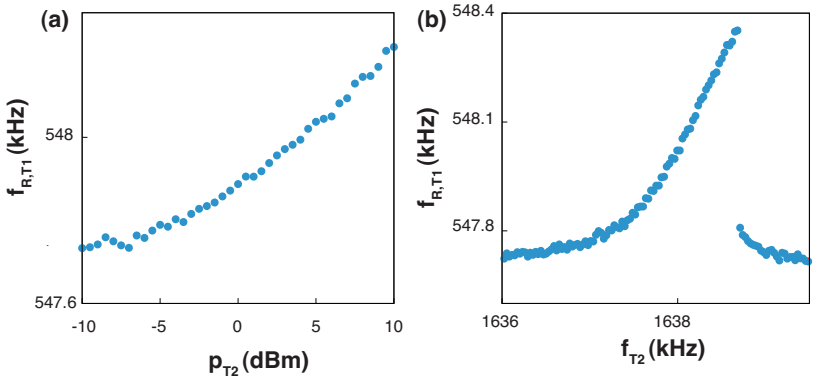

FIGURE 6.4: Torsional-torsional mode interactions. (a) The resonance frequency of the first torsional mode, when the drive power at the second torsional mode on resonance is varied. The resonance frequency of mode 1, $f_{R,T1}$, increases with the drive power of the second mode, p_{T2}. (b) The nonlinear response of the second mode is measured by using the first mode as a detector.

proaches its resonance, the response of mode 1 becomes more linear (panel ii). Here, the frequency stiffening and weakening nonlinearities are balanced yielding a linear response. At high amplitude of the second mode, frequency weakening of mode 1 (panel iii) is observed. When the amplitude of the second mode drops, frequency stiffening is restored (panel iv). This measurement not only demonstrates the coupling between the torsional modes, but also that the sign of the nonlinearity constant of a torsional mode depends on the amplitude of the motion of the other modes. By simultaneous driving another mode, the torsional frequency response can be tuned from a stiffening to a weakening characteristic.

6.3.3 FLEXURAL-TORSIONAL MODE INTERACTION

The coupling between the first flexural and first torsional mode is now studied experimentally. Fig. 6.6(a) shows the resonance frequency of the first torsional mode as a function of drive power of the first flexural mode. The resonance frequency increases with 100 Hz when the power in the flexural mode is increased to 10 dBm. Detection of the nonlinear flexural mode by measuring the resonance frequency of the torsional mode is shown in Fig. 6.6(b). The nonlinear interactions when both modes are driven in the nonlinear regime are shown in Fig. 6.6(c) and (d). The interaction is clearly visible in the frequency-frequency plots, where one frequency is swept and the frequency of the RF source is stepped across the nonlinear resonances of both modes.

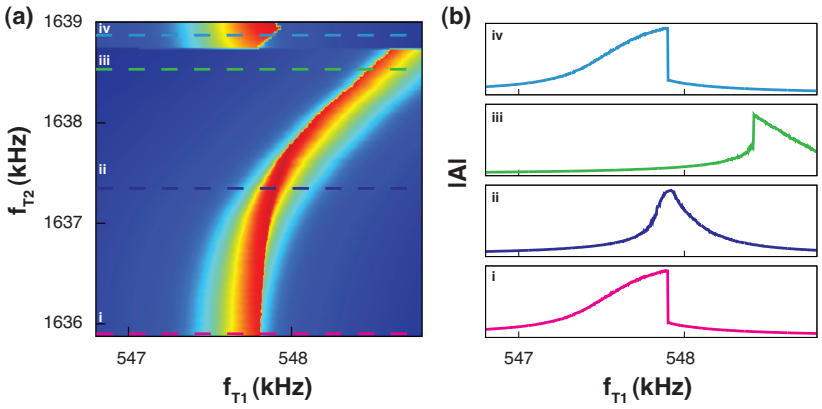

FIGURE 6.5: Tuning the torsional nonlinearity via modal interactions. (a) Frequency responses of the nonlinear first torsional mode, while the frequency of the second mode is swept through its nonlinear resonance. The frequency stiffening of the torsional mode changes into weakening when the second mode oscillates with high amplitudes. When the amplitude of the second mode jumps down, again frequency stiffening is observed. (b) Traces from (a) taken at the indicated frequencies. In panel (ii) the response is close to a linear one, due to balancing of the stiffening and weakening nonlinearities.

6.4 DISCUSSION AND CONCLUSION

In summary, we demonstrated the coupling between the flexural and torsional vibration modes in a microcantilever. This coupling is due to nonlinearities, which also give rise to a amplitude-dependent resonance frequency. The interactions between the different flexural modes, between different torsional modes and between the flexural and torsional modes are demonstrated in detailed experiments. We also demonstrate the nonlinear frequency stiffening of torsional modes driven at high amplitudes.

Several applications are proposed for the modal interactions. A specific resonance mode can be shifted to a higher frequency by simultaneously driving another mode. For strongly driven modes, the cubic spring constant (nonlinearity) can be modified from positive to negative, tuning the response from stiffening to weakening. By balancing two excitation strengths, a nonlinear response can be tuned to a linear one. By modal interactions, one mode can be used to detect the motion of another mode of the same cantilever. Besides these applications, the modal interactions have consequences for multi-mode schemes, such as the scanning probe microscopy and mass sensors based on microcantilevers [14, 22–24].

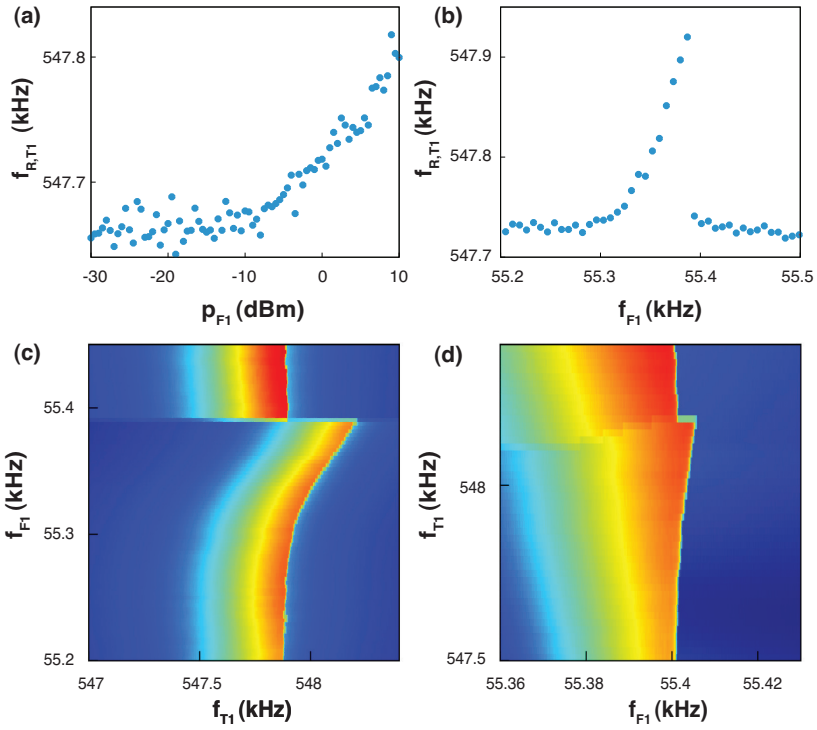

FIGURE 6.6: Flexural-torsional interaction. (a) Resonance frequency shift of the first torsional mode, when the drive power of the first flexural mode is increased. The resonance frequencies are obtained from thermal noise spectra. (b) The nonlinear resonance response of the first flexural mode reflected in the resonance frequency of the torsional mode (from thermal noise spectra). (c) and (d) Nonlinear dynamics when the flexural as the torsional mode are both excited in the nonlinear regime.

REFERENCES

[1] H. J. R. Westra, H. S. J. van der Zant, and W. J. Venstra, *Modal interactions of flexural and torsional vibrations in a microcantilever*, Ultramicroscopy **120**, 41 (2012).

[2] G. Binnig, C. F. Quate, and C. Gerber, *Atomic Force Microscope*, Phys. Rev. Lett. **56**, 930 (1986).

[3] L. Huang and C. Su, *A torsional resonance mode AFM for in-plane tip surface*

interactions, Ultramicroscopy **100**, 277 (2004), ISSN 0304-3991.

[4] J. M. Neumeister and W. A. Ducker, *Lateral, normal, and longitudinal spring constants of atomic force microscopy cantilevers*, Review of Scientific Instruments **65**, 2527 (1994), ISSN 0034-6748.

[5] D. Pires, J. L. Hedrick, A. De Silva, J. Frommer, B. Gotsmann, H. Wolf, M. Despont, U. Duerig, and A. W. Knoll, *Nanoscale Three-Dimensional Patterning of Molecular Resists by Scanning Probes*, Science **328**, 732 (2010).

[6] M. Dong, S. Husale, and O. Sahin, *Determination of protein structural flexibility by microsecond force spectroscopy*, Nature Nanotechnol **4**, 514 (2009).

[7] R. Hillenbrand, M. Stark, and R. Guckenberger, *Higher-harmonics generation in tapping-mode atomic-force microscopy: Insights into the tip–sample interaction*, Applied Physics Letters **76**, 3478 (2000).

[8] S. Rützel, S. I. Lee, and A. Raman, *Nonlinear dynamics of atomicâĂŞforceâĂŞmicroscope probes driven in LennardâĂŞJones potentials*, Proceedings of the Royal Society of London. Series A: Mathematical, Physical and Engineering Sciences **459**, 1925 (2003).

[9] W. J. Venstra, H. J. R. Westra, and H. S. J. van der Zant, *Mechanical stiffening, bistability, and bit operations in a microcantilever*, Appl. Phy. Lett. **97**, 193107 (2010).

[10] H. J. R. Westra, M. Poot, H. S. J. van der Zant, and W. J. Venstra, *Nonlinear modal interactions in clamped-clamped mechanical resonators*, Phys. Rev. Lett. **105**, 117205 (2010).

[11] A. Gaidarzhy, J. Dorignac, G. Zolfagharkhani, M. Imboden, and P. Mohanty, *Energy measurement in nonlinearly coupled nanomechanical modes*, Applied Physics Letters **98**, 264106 (pages 3) (2011).

[12] W. J. Venstra, H. J. R. Westra, and H. S. J. van der Zant, *Q-factor control of a microcantilever by mechanical sideband excitation*, Appl. Phys. Lett. **99**, 151904 (2011).

[13] R. Garcia and E. Herruzo, *The emergence of multifrequency force microscopy*, Nature Nanotechnol **7**, 217 (2012).

[14] A. Raman, S. Trigueros, A. Cartagena, A. P. Z. Stevenson, M. Susilo, E. Nauman, and S. Antoranz Contera, *Mapping nanomechanical properties of live cells using multi-harmonic atomic force microscopy*, Nature Nanotech. **6**, 809 (2011).

[15] E. Sapountzakis and V. Tsipiras, *Nonlinear nonuniform torsional vibrations of bars by the boundary element method*, Journal of Sound and Vibration **329**, 1853 (2010), ISSN 0022-460X.

[16] K. B. Gavan, E. W. J. M. van der Drift, W. J. Venstra, M. R. Zuidam, and H. S. J. van der Zant, *Effect of undercut on the resonant behaviour of silicon nitride cantilevers*, Journal of Micromechanics and Microengeneering **19**, 035003 (2009).

[17] M. R. M. Crespo da Silva and C. C. Glynn, *Nonlinear Flexural-Flexural-Torsional Dynamics of Inextensional Beams. I. Equations of motion*, J. Struct. Mech. **6**, 437 (1978).

[18] M. R. M. Crespo da Silva and C. C. Glynn, *Nonlinear Flexural-Flexural-Torsional Dynamics of Inextensional Beams. II. Forced Motions*, J. Struct. Mech. **6**, 449 (1978).

[19] R. Lifshitz and M. Cross, *Nonlinear dynamics of nanomechanical and micromechanical resonators*, Rev. Nonlinear Dyn. Complexity **1**, 1 (2008).

[20] A. Nayfeh, C. Chin, and S. Nayfeh, *Nonlinear normal modes of a cantilever beam*, Journal of vibration and acoustics **117**, 477 (1995).

[21] M. Lohndorf, J. Moreland, and P. Kabos, *Ferromagnetic resonance detection with a torsion-mode atomic-force microscope*, Applied Physics Letters **76**, 1176 (2000).

[22] M. Li, H. X. Tang, and M. L. Roukes, *Ultra-sensitive NEMS-based cantilevers for sensing, scanned probe and very high-frequency applications*, Nature Nanotech. **2**, 114 (2007).

[23] R. Raiteri, M. Grattarola, H.-J. Butt, and P. Skládal, *Micromechanical cantilever-based biosensors*, Sensors and Actuators B **79**, 115 (2001), ISSN 0925-4005.

[24] S. Dohn, W. Svendsen, A. Boisen, and O. Hansen, *Mass and position determination of attached particles on cantilever based mass sensors*, Review of Scientific Instruments **78**, 103303 (pages 3) (2007).

7

Q FACTOR CONTROL BY SIDEBAND EXCITATION

We demonstrate the coupling between the fundamental and second flexural modes of a microcantilever. A mechanical analogue of cavity-optomechanics is then employed, where the mechanical cavity is formed by the second vibrational mode of the same cantilever, coupled to the fundamental mode via the geometric nonlinearity. By exciting the cantilever at the sum and difference frequencies between fundamental and second flexural mode, the thermal motion of the fundamental mode of the cantilever is damped and amplified. This concept makes it possible to enhance or suppress the Q factor over a wide range.

Parts of this chapter have been published in Appl. Phys. Lett. **99**, 151904 (2011) [1].

7.1 INTRODUCTION

CANTILEVERS have numerous scientific and technological applications and are used in various instruments. In sensing applications, the sensitivity is related to the Q factor, and this has motivated researchers to increase the Q factor of mechanical resonators, in particular, in dissipative environments. Among the techniques that have been employed are applying residual stress [2], parametric pumping [3], self-oscillation by internal [4] and external [5] feedback mechanisms. When increasing the Q factor in these ways, energy is pumped into the mechanical mode and the resonator heats up. The opposite effect leads to cooling of the resonator and attenuation of its motion [6]. By pumping energy out of the mechanical resonator into a high quality-factor optical or microwave cavity, several groups have shown reduction of the effective temperature of the vibrational mode from room temperature to millikelvin temperatures [7–15]. Such cooling schemes are now employed to bring down the mode temperature to below the an average phonon occupation number of one, providing a promising route to study the quantum behavior of a mechanical resonator [16–18].

In analogy to cavity optomechanics, where an optical or a microwave cavity is used to extract energy from the resonator, we employ a mechanical cavity to damp the mechanical mode. Here, the fundamental flexural mode of the cantilever is the mode of interest, and the mechanical cavity is formed by the second flexural mode of the same cantilever, which is geometrically coupled to the fundamental mode. In this paper, we demonstrate the presence of this coupling by strongly driving the cantilever on resonance, while monitoring its broadband frequency spectrum. Sidebands appear in the spectrum, which are located at the sum and difference frequencies of fundamental and second mode of the cantilever. Driving the cantilever at these sidebands results in positive or negative additional damping, which is demonstrated in this Chapter.

7.2 FABRICATION AND CHARACTERIZATION

Cantilevers are fabricated from low pressure chemical vapor deposited silicon nitride by electron beam lithography and isotropic reactive ion etching in a O_2/CHF_3 plasma [19]. The dimensions are length × width × height = 39 μm × 8 μm × 70 nm. An optical deflection technique, similar to the one employed in atomic force microscopy, is used to detect the cantilever motion. Figures 7.1(a) and 7.1(b) show the cantilever and the setup. The cantilever is mounted on a piezo crystal and placed in a vacuum chamber at a pressure of $\sim 10^{-5}$ mbar. Two spectrum analyzers are used to simultaneously measure the thermal motion of the fundamental ($i = 1$) and second ($i = 2$) flexural mode. Figure 7.1(b) shows the power spectra without driving the piezo. The resonance frequencies and Q factors are determined by fit-

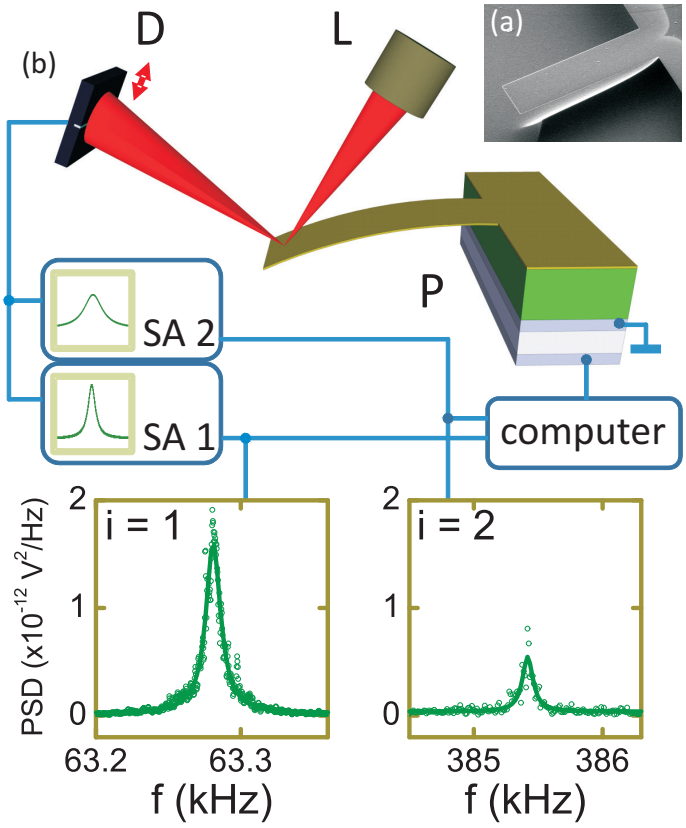

FIGURE 7.1: (a) Scanning electron micrograph of the silicon nitride cantilever. (b) Diagram of the measurement circuit showing photodiode (D), laser (L), piezo (P) and the spectrum analyzers to measure the fundamental (SA 1) and the second (SA 2) flexural mode. The thermal noise spectra are shown at the fundamental (i = 1) and second (i = 2) flexural mode of the cantilever.

ting Lorentzian functions (solid lines), and we find f_1 = 63.2 kHz and f_2 = 385.4 kHz and f_3 = 1.068 MHz (not shown). The ratio's f_2/f_1 = 6.1 and f_3/f_1 = 16.9 are close to the expected modal frequencies α_{21} =6.3 and α_{31} = 17.5 representing the spectrum of a homogeneous cantilevered Euler-Bernoulli beam. For the fundamental and second resonance modes, the corresponding Q factors are Q_1 = 5184 and Q_2 = 3922. The frequency difference, $f_2 - f_1$ = 322 kHz, exceeds the bandwidth of the modes, f_1/Q_1 = 12 Hz and f_2/Q_2 = 98 Hz, by four orders of magnitude.

To demonstrate the coupling between the fundamental and second flexural modes of the cantilever, we drive the cantilever on resonance, while measuring its broadband spectrum. Figure 7.2(a) shows this spectrum as a function of the drive strength. When the amplitude of the second mode increases, mechanical sidebands become visible in the spectrum. These sidebands occur at $f_2 \pm f_1$, and clearly indicate the presence of mechanical coupling between the two modes. Traces for weak and strong driving are extracted from 7.2(a) in Fig. 7.2(b), to show the shape and relative amplitudes of the sidebands. As the spacing between the sidebands is much larger than the linewidth of the mode, we operate in the resolved sideband regime [7].

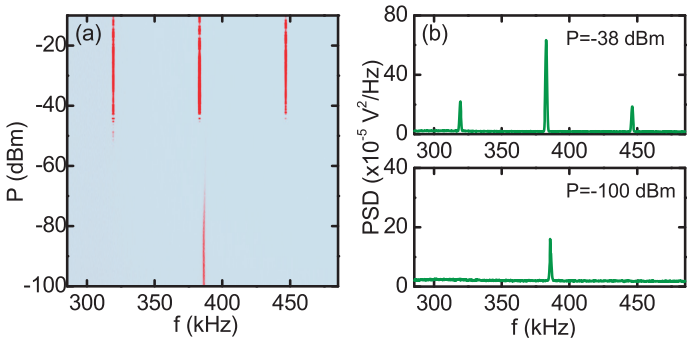

FIGURE 7.2: (a) Noise spectrum while driving the second flexural at increasing amplitudes. At strong driving, sidebands emerge in the spectra at the sum and difference frequencies of the fundamental and second flexural mode. Color scale represents the power spectral density. (b) The cross-sections of panel (a) at weak (bottom) and strong (top) driving show the shape and intensity of the sidebands.

The mechanism that couples the vibrational modes in a cantilever can be qualitatively understood as follows. A nonzero amplitude of one flexural mode of the cantilever changes the shape of the cantilever [20]. This geometric change has a small but measurable effect on the resonance frequency of all the other vibrational modes. The effect of the cantilever amplitude on its own resonance frequency was recently analyzed in detail [21]; for the first few modes any nonzero amplitude stiffens the frequency response, and this gives rise to frequency pulling. Recently, we also presented a detailed study on the coupling mechanism between the vibrational modes in clamped-clamped resonators [22]. Here, the coupling between the modes is fully described by the displacement-induced tension. A similar analysis can be carried out for the coupling between vibration modes of a cantilever beam. The only difference is that in the inextensional cantilever the modes are coupled by the geometric nonlinearity, whereas for the (extensional) clamped-

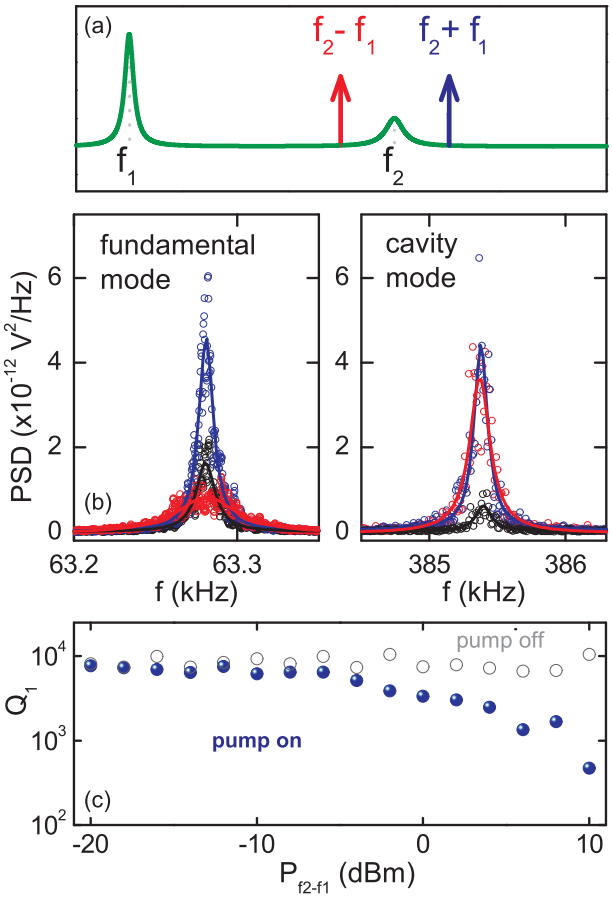

FIGURE 7.3: (a) Damping and amplification of the fundamental mode by pumping the sidebands of the second flexural mode. The sum and difference frequencies are indicated by the arrows. By exciting the cantilever on the red sideband the fundamental mode is suppressed, and its motion is amplified by exciting on the blue sideband. (b) Noise spectra of the fundamental mode (left) and the cavity mode (right). The black curves represent the thermal noise spectra without excitation. The red curves are obtained by pumping the red sideband, resulting in positive damping of the cantilever. The blue curves are measured while pumping the blue sideband, which results in negative damping (amplification). (c) The Q factor of the fundamental mode as a function of pump power on the red sideband (closed dots). For each power a control experiment is carried out without excitation, indicated by the open circles.

clamped resonator the modes are coupled by the displacement-induced tension. For a cantilever, the modal amplitudes u_i are calculated by solving the (dimensionless) coupled equations [23]

$$\ddot{u}_i + \eta_i \dot{u}_i + \omega_i^2 u_i + \sum_{j=1}^{n}\sum_{k=1}^{n}\sum_{l=1}^{n}\left(\alpha_{ijkl} u_j u_k u_l + \beta_{ijkl} u_j (u_k u_l)'\right)' = f_i \cos(\Omega_i t), \quad (7.1)$$

where η_i represents a damping constant, ω_i the resonance frequency, Ω_i the drive frequency and f_i the excitation strength of mode i. The dots and primes denote derivative to time and coordinate, s, respectively. The coupling coefficients α_{ijkl} and β_{ijkl} are calculated by integrating the cantilever modeshapes ξ_i as follows:

$$\alpha_{ijkl} = \int_0^1 \xi_i \{\xi_j' (\xi_k' \xi_l'')'\}' \mathrm{d}s \quad (7.2)$$

$$\beta_{ijkl} = \int_0^1 \xi_i \left(\xi_j' \int_1^s \int_0^{s_2} \xi_k' \xi_l' \mathrm{d}s_1 \mathrm{d}s_2\right)' \mathrm{d}s. \quad (7.3)$$

Taking only the fundamental and the second mode into consideration, Eq. 7.1 yields two coupled nonlinear differential equations with constant coefficients, which can be solved numerically.

7.3 Q FACTOR CONTROL

The coupling between the vibrational modes can be used to transfer energy by employing a process similar to sideband cooling in cavity-optomechanics, where the cavity is used extract energy from the mechanical mode. The mechanical resonator is embedded in an optical [7–11] or microwave cavity [12–14]. In analogy to those experiments and given the presence of the mechanical mode-coupling, the damping of one mechanical mode by another mode of the same resonator can be envisioned. Using the coupling mechanism described in the previous section, any change in the position of the mode under consideration (the fundamental flexural mode in the experiments that follow) changes the stiffness of the mode that acts as the cavity (the second flexural mode). The energy change in the cavity mode is retarded by the cavity relaxation time, equal to $\sim Q_2/f_2$ for our mechanical cavity. Due to the delayed response of the cavity mode, a force is exerted by the cavity mode on the fundamental mode. This velocity-proportional force can either amplify or attenuate the motion of the fundamental mode [24]. In case of red-detuned driving, the damping force on the fundamental mode is increased. When the driving is blue-detuned, the motion of both the cavity mode and the fundamental mode is amplified. The schemes are illustrated in Fig. 7.3(a), where the two Lorentzian shaped curves represent the two flexural modes of the cantilever, and

the driving frequencies corresponding to blue and red detuning are indicated by the arrows. The damping rate is maximized by driving at the sum and difference frequencies, and is increased by decreasing the linewidth of the cavity mode.

The effect of sideband excitation on the damping of the cantilever is demonstrated by measuring the thermal noise spectra of the fundamental and second flexural resonance modes, while driving the piezo sinusoidally at their sum and difference frequencies. Figure 7.3(b) shows the spectrum without driving (indicated by the black open circles). When the cantilever is driven at the blue-detuned sideband, its amplitude increases as shown by the blue curve. The blue and red curves in the power spectral density plots of Fig. 7.3(b) correspond to driving at the blue and red-detuned sidebands of the cavity mode shown in Fig. 7.3(a). By fitting Lorentzian functions to the data, we obtain the temperature and the Q factors of the fundamental mode while driving the sidebands. When the cantilever is driven at the red sideband, the Q factor of the fundamental mode decreases from 4599 to 1421. No changes in the temperature of the mode are observed, which indicates that the energy extracted via the modal interactions leaks back into the mode via other transport mechanisms, which are absent in e.g. optomechanical cooling schemes. When driving at the blue sideband, the Q factor increases to 5849. For the cavity mode, by red-detuned driving the Q factor decreases from 2776 to 2108, while for blue-detuned driving it increases to 3185. Here we do observe a change in temperature, by a factor of 3.6 for the red and 6.3 for the blue-detuned driving.

By increasing the drive strength at the red-detuned sideband the amplitude of the cantilever motion is further attenuated, as is shown in Fig. 7.3(c). Here, the Q factor of the fundamental mode is shown as a function of the applied driving power at $f_2 - f_1$. A 20-fold reduction of the Q factor is achieved compared to the Q factor without driving the sideband. This clearly demonstrates that driving at the mechanical sidebands can be used to modify the damping characteristics of a micromechanical resonator to great extent. This scheme can be used to modify the Q factor in cantilever-based instrumentation, where we note that the changes in damping obtained in these experiments are of the same order as the viscous damping in air, so that stronger excitation is needed to obtain a significant change in the damping.

7.4 CONCLUSION

In conclusion, we demonstrate the coupling between the flexural modes of a microcantilever. This coupling is marked by mechanical sidebands in the frequency spectrum, which are located at the sum and difference frequencies. Driving the cantilever at these mechanical sidebands results in additional damping of the resonator, which can be either negative or positive in sign. This is demonstrated

for the fundamental and the second flexural mode. Furthermore, using a second mode of the same resonator as a cavity provides a means to cooling experiments based on modal interactions. In present sideband-cooling experiments, coupling a mechanical resonator to an optical or microwave cavity can pose significant experimental challenges. The coupling described in this work is present by nature, and its strength can be tuned by engineering stress and geometry. More explicitly, in carbon nanotube resonators with extremely high Q factors [25] at low temperatures, coupling between the vibrational modes as described in Ref. [22] may provide a route to cool mechanical modes to the quantum ground state.

REFERENCES

[1] W. J. Venstra, H. J. R. Westra, and H. S. J. van der Zant, *Q-factor control of a microcantilever by mechanical sideband excitation*, Appl. Phys. Lett. **99**, 151904 (2011).

[2] S. S. Verbridge, H. G. Craighead, and J. M. Parpia, *A megahertz nanomechanical resonator with room temperature quality factor over a million*, Appl. Phys. Lett. **92**, 013112 (2008).

[3] I. Mahboob and H. Yamaguchi, *Parametrically pumped ultrahigh Q electromechanical resonator*, Appl. Phys. Lett. **92**, 253109 (2009).

[4] P. G. Steeneken, K. Le Phan, M. J. Goossens, G. E. J. Koops, G. J. A. M. Brom, C. van der Avoort, and J. T. M. van Beek, *Piezoresistive heat engine and refrigerator*, Nature Phys. **7**, 354 (2011).

[5] X. L. Feng, C. J. White, A. Hajimiri, and M. L. Roukes, *A self-sustaining ultrahigh-frequency nanoelectromechanical oscillator*, Nature Nanotech. **3**, 342 (2008).

[6] D. Rugar and P. Grütter, *Mechanical parametric amplification and thermomechanical noise squeezing*, Phys. Rev. Lett. **67**, 699 (1991).

[7] T. Kippenberg and K. Vahala, *Cavity optomechanics: back-action at the mesoscale*, Science **321**, 1172 (2008).

[8] O. Arcizet, P.-F. Cohadon, T. Briant, M. Pinard, and A. Heidmann, *Radiation-pressure cooling and optomechanical instability of a micromirror*, Nature **444**, 71 (2006).

[9] S. Gigan, H. R. Bohm, M. Paternostro, F. Blaser, G. Langer, J. B. Hertzberg, K. C. Schwab, D. Bauerle, M. Aspelmeyer, and A. Zeilinger, *Self-cooling of a micromirror by radiation pressure*, Nature **444**, 67 (2006).

[10] A. Schliesser, O. Arcizet, R. Riviere, G. Anetsberger, and T. J. Kippenberg, *Resolved-sideband cooling and position measurement of a micromechanical oscillator close to the Heisenberg uncertainty limit*, Nature Phys. **5**, 509 (2009).

[11] Y.-S. Park and H. Wang, *Resolved-sideband and cryogenic cooling of an optomechanical resonator*, Nature Phys. **5**, 489 (2009).

[12] K. R. Brown, J. Britton, R. J. Epstein, J. Chiaverini, D. Leibfried, and D. J. Wineland, *Passive Cooling of a Micromechanical Oscillator with a Resonant Electric Circuit*, Phys. Rev. Lett. **99**, 137205 (2007).

[13] C. A. Regal, J. D. Teufel, and K. W. Lehnert, *Measuring nanomechanical motion with a microwave cavity interferometer*, Nature Phys. **4**, 555 (2008).

[14] T. Rocheleau, T. Ndukum, C. Macklin, J. B. Hertzberg, A. A. Clerk, and K. C. Schwab, *Preparation and detection of a mechanical resonator near the ground state of motion*, Nature **463**, 72 (2010).

[15] M. Poot, S. Etaki, H. Yamaguchi, and H. S. J. van der Zant, *Discrete-time quadrature feedback cooling of a radio-frequency mechanical resonator*, Appl. Phys. Lett. **99**, 013113 (2011).

[16] A. D. O'Connell, M. Hofheinz, M. Ansmann, R. C. Bialczak, M. Lenander, E. Lucero, M. Neeley, D. Sank, H. Wang, M. Weides, et al., *Quantum ground state and single-phonon control of a mechanical resonator*, Nature **464**, 697 (2010).

[17] J. D. Teufel, T. Donner, D. Li, J. W. Harlow, M. S. Allman, K. Cicak, A. J. Sirois, J. D. Whittaker, K. W. Lehnert, and R. W. Simmonds, *Sideband cooling of micromechanical motion to the quantum ground state*, Nature **475**, 359 (2011).

[18] J. Chan, T. P. Mayer Alegre, A. H. Safavi-Naeini, J. T. Hill, A. Krause, S. Gröblacher, M. Aspelmeyer, and O. Painter, *Laser cooling of a nanomechanical oscillator into its quantum ground state*, Nature **479**, 89 (2011).

[19] K. Babaei Gavan, E. W. J. M. van der Drift, W. J. Venstra, M. R. Zuiddam, and H. S. J. van der Zant, *Effect of undercut on the resonant behaviour of silicon nitride cantilevers*, J. Micromech. Microeng. **19**, 035003 (2009).

[20] M. R. M. Crespo da Silva and C. C. Glynn, *Nonlinear Flexural-Flexural-Torsional Dynamics of Inextensional Beams. I. Equations of motion*, J. Struct. Mech. **6**, 437 (1978).

[21] W. J. Venstra, H. J. R. Westra, and H. S. J. van der Zant, *Mechanical stiffening, bistability, and bit operations in a microcantilever*, Appl. Phy. Lett. **97**, 193107 (2010).

[22] H. J. R. Westra, M. Poot, H. S. J. van der Zant, and W. J. Venstra, *Nonlinear modal interactions in clamped-clamped mechanical resonators*, Phys. Rev. Lett. **105**, 117205 (2010).

[23] M. C. M. Crespo da Silvaand C. L. Zaretzky, *Non-linear modal coupling in planar and non-planar responses of inextensional beams*, Int. J. Non-Linear Mech. **25**, 227 (1990).

[24] A. Schliesser, O. A. R. Rivière, G. Anetsberg, and T. J. Kippenberg, *Resolved-sideband cooling of a micromechanical resonator*, Nature Phys. **4**, 415 (2008).

[25] A. K. Hüttel, G. A. Steele, B. Witkamp, M. Poot, L. P. Kouwenhoven, and H. S. J. van der Zant, *Carbon Nanotubes as Ultrahigh Quality Factor Mechanical Resonators*, Nano Lett. **9**, 2547 (2009).

8

INTERACTION BETWEEN A DIRECTLY- AND PARAMETRICALLY-DRIVEN MODE

The interactions between parametrically- and directly-driven vibration modes of a clamped-clamped beam resonator are studied. An integrated piezoelectric transducer is used for direct and parametric excitation. First, the parametric amplification and oscillation of a single mode are analyzed by the power and phase dependence below and above the threshold for parametric oscillation. Then, the motion of a parametrically-driven mode is detected by the induced change in resonance frequency in another mode of the same resonator. The resonance frequency shift is the result of the nonlinear coupling between the modes by the displacement-induced tension in the beam. These nonlinear modal interactions result in the quadratic relation between the resonance frequency of one mode and the amplitude of another mode. The amplitude of a parametrically-oscillating mode depends on the square root of the pump frequency. Combining these dependencies yields a linear relation between the resonance frequency of the directly-driven mode and the frequency of the parametrically-oscillating mode.

Parts of this chapter have been published in Phys. Rev. B **84**, 134305 (2011) [1].

8.1 INTRODUCTION

PARAMETRIC amplification and oscillations occur when in a resonant system, one of the system parameters (e.g. spring constant, effective mass) is modulated. The principle is used in low-noise electronic amplifiers [2, 3] and to increase the broadband gain in fiber optics [4–6]. In mechanical resonators, parametric oscillations are typically obtained by modulation of the spring constant [7–10]. Applications of parametric resonances in nano- and micro electromechanics [11] (NEMS and MEMS) include quality (Q-)factor enhancement [12, 13] and bit storage and bit flips using the bistable phase in a parametric oscillator [14, 15]. Parametric amplification can also be used for noise-squeezing in a coupled qubit-resonator system [16] and was recently observed in carbon nanotube resonators [17].

Another interesting phenomenon in NEMS is the interaction between different vibration modes. Motivated by the trend towards large scale integration of resonators, researchers study the interactions between several resonators [18]. Recently, nonlinear modal interactions between two flexural modes in a clamped-clamped beam resonator [19–21] and a cantilever [22] have been reported: it has been shown that the resonance frequency of one mode depends quadratically on the amplitude of another mode.

Here, we explore the modal interactions between a directly and a parametrically driven mode, yielding a *linear* dependence of the resonance frequency of the directly driven mode on the pump frequency of the parametrically driven mode. In Sec. 8.2, the experimental conditions are provided. The following section reports on a detailed analysis of the piezoelectrical parametric amplification of a single mode. Section 8.4 discusses the modal interactions between a directly driven and a parametrically pumped mode, and this is the central result of this work.

8.2 DEVICE DETAILS

The resonators are clamped-clamped beams fabricated from 500 nm thick low-stress silicon nitride (SiN). A stack of platinum (Pt), aluminum nitride (AlN) and Pt (100-400-100 nm thick) is sputtered on top, to form an integrated piezoelectric transducer. Figure 8.1(a) shows a scanning electron micrograph of the device, the white arrow indicates the transducer. The resonators are freely suspended by a through-the-wafer etch. Two lengths are used: L = 500 and 750 μm. The width of both resonators is 45 μm. Details of the fabrication procedure are described in Ref. [23]. An ac voltage on the piezo produces a force on the resonator and at the same time modulates its spring constant. Both the force and the spring constant depend linearly on the voltage. The voltage on the piezo, V_{out}, is composed of two frequencies, one to directly excite the resonator and one to parametrically pump

it, i.e. $V_{\text{out}} = V_{\text{direct}} \cos(\Omega t) + V_{\text{pump}} \cos(2\Omega t + \phi)$, where Ω is the drive frequency and ϕ the phase difference between the two voltages.

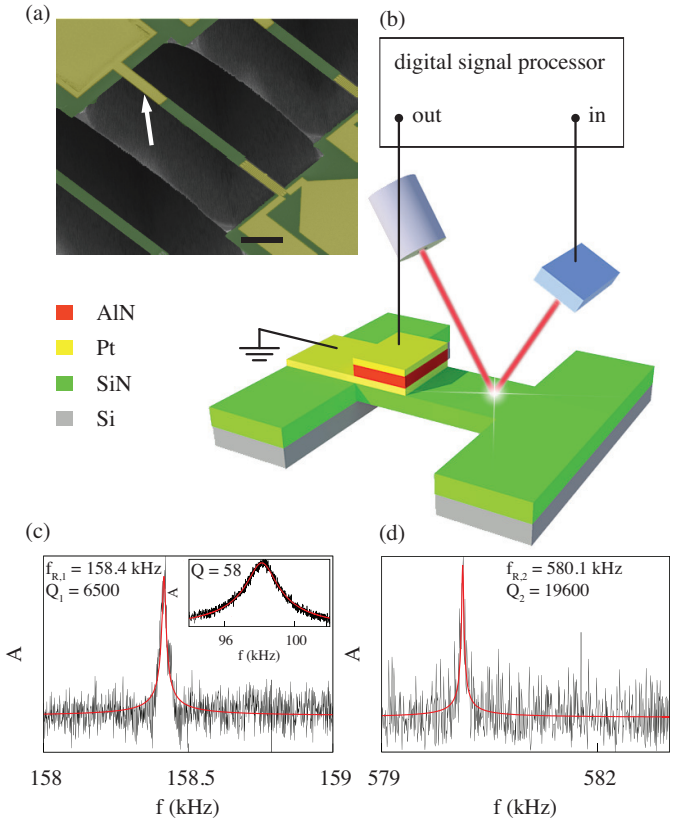

FIGURE 8.1: Measurement setup. (a) False-colored scanning electron micrograph of a SiN beam with the piezo actuator (white arrow) on top (scale bar is 20 μm). (b) An optical deflection setup is used to detect motion in air and vacuum. The piezo-active AlN layer is depicted in red. The piezo actuator and photo diode are connected to a digital signal processor. (c,d) Typical frequency responses of the first (c) and second (d) mode (amplitude A) in vacuum. The inset in (c) shows the frequency response in air, of the resonator with length 750 μm, with a resonance frequency of 98 kHz. The response of a damped-driven harmonic oscillator is fitted through the responses to obtain Q factors and resonance frequencies.

The motion of the resonator is measured using an optical deflection setup, as depicted in Fig. 8.1(b). Frequency spectrum and network analyzer measurements

are implemented in a digital signal processor. Measurements are conducted in vacuum at a pressure of 10^{-4} mbar and at atmospheric pressure. For direct driving, the frequency responses at the first mode and second mode in vacuum are shown in Fig. 8.1(c) and 8.1(d), with $Q_1 = 6500$ and $Q_2 = 19600$ [1].

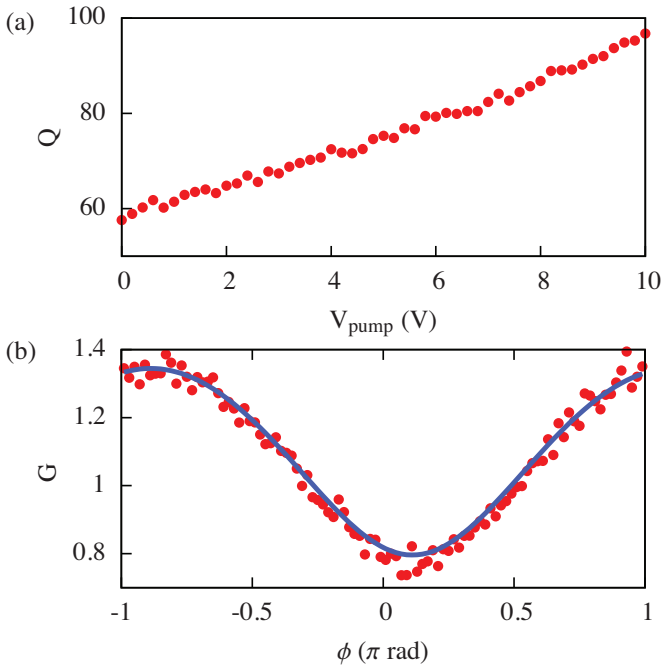

FIGURE 8.2: Characterization of the parametric amplification in air. (a) The Q factor enhancement is proportional to the parametric pump voltage. (b) Measured gain-phase relation; the blue line represents Eq. 2, with fit parameter $k_p/k_t = 0.26$.

8

8.3 PARAMETRIC AMPLIFICATION OF A SINGLE MODE

The time-dependent part of the equation of motion of the piezoelectric resonator including parametric modulation of the spring constant is described by

$$m\ddot{u} + \frac{m\omega_R}{Q}\dot{u} + [m\omega_R^2 + k_p \sin(2\Omega t + \phi)]u + \alpha u^3 = F\cos(\Omega t). \tag{8.1}$$

[1] During the experiments, the drift of the resonance frequency is within 3 %.

Here, $u(t)$ is the amplitude of the mode, m is the effective mass and F the direct drive force, and ω_R is the resonance frequency. The dots denote taking the derivative to time. The spring constant is modulated at twice the drive frequency Ω with modulation strength k_p. α accounts for the Duffing nonlinearity with $\alpha > 0$ for clamped-clamped beams [24]. The parametric gain G is defined by the ratio between the amplitude of the motion with and without parametric drive, and can be calculated from Eq. 8.1 [25, 26]:

$$G(\phi) = \sqrt{\frac{\cos^2(\phi/2)}{(1+k_p/k_t)^2} + \frac{\sin^2(\phi/2)}{(1-k_p/k_t)^2}}. \tag{8.2}$$

This equation holds for small amplitude vibrations, where the nonlinearity can be neglected. Depending on ϕ, the motion is amplified ($G > 1$) or attenuated ($G < 1$). Above the threshold parametric pump, $k_p > k_t$ with $k_t = 2m\omega_R^2/Q$, the resonator is parametrically oscillating.

Parametric behavior is demonstrated for a resonator with length 750 μm vibrating in air, with $f_{R,1} = 98$ kHz and $Q_1 = 58$ [frequency response in the inset of Fig 8.1c]. To amplify the motion, the resonator is driven parametrically at $2f_{R,1}$ with $\phi = -0.75\pi$. Figure 2(a) shows the Q factor of the resonator as a function of the parametric pump voltage. The Q factor increases by a factor of 1.7 when the parametric pump is 10 V. Furthermore, the phase dependence of the gain at 10 V parametric pump is plotted in Fig. 8.2(b). The gain varies periodically with the phase difference with a period of 2π. The minimum gain is smaller than one, indicating destructive interference by an out-of-phase parametric signal. Eq. 8.2 fits the measured data well with $k_p = 0.26\,k_t$. In these experiments the parametric driving is below the parametric threshold k_t. A further increase of the pump voltage is not possible as this would damage the piezo-stack. To study parametric oscillation, further experiments are conducted in vacuum. Here the Q factor improves by two orders of magnitude [Fig. 8.1(c)], enabling post-threshold driving.

Figure 8.3 summarizes the measurements of the parametric oscillations performed in vacuum. A 500 μm long resonator is used, for which the frequency response is plotted in Fig. 8.1(c). Frequency spectra are measured for three parametric pump voltages in Fig. 8.3(a). At 80 mV no sign of oscillation is observed (lower panel), and the onset of parametric oscillation is found around 85 mV as shown in the middle panel. A further increase of the pump voltage (upper panel) results in a larger oscillation amplitude. Here, the nonlinear term in Eq. 8.1 results in an amplitude-dependent resonance frequency. Figure 8.3(b) shows network analyzer measurements of the resonator amplitude (color scale) as a function of the pump voltage. The resonator is driven directly and parametrically with $\phi = -0.65\pi$. A direct drive signal, weak enough to operate the resonator in the

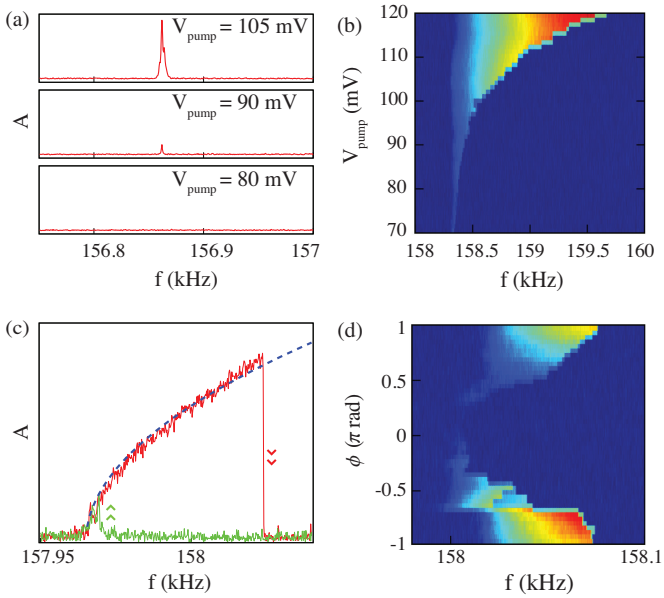

FIGURE 8.3: Parametric oscillations of the first flexural mode in vacuum. (a) Frequency spectra at three pump voltages, the parametric oscillation becomes visible when $V_{\text{pump}} > 85$ mV. (b) Parametric tongue, showing frequency responses when the resonator is driven directly ($V_{\text{direct}} = 5$ mV) and parametrically past the instability threshold. Color indicates the amplitude of oscillation. (c) The hysteresis between the forward (red) and reverse sweep (green) when driving parametrically ($V_{\text{pump}} = 95$ mV). The blue dashed line shows the square root dependence of the amplitude (A) on the frequency f. (d) The phase dependence of the parametric oscillations at $V_{\text{pump}} = 95$ mV. The color indicates the amplitude of oscillation.

8

linear regime when $V_{\text{pump}} = 0$, is applied to initiate the motion. The motion of the weakly driven resonator is coherently amplified by the parametric excitation and the amplitude increases with V_{pump}. The observed frequency stiffening is expected for a cubic spring constant $\alpha > 0$. The oscillation sustains over a few kHz when the frequency is swept forward. The amplitude shows a hysteretic response when the frequency is swept back, see Fig. 8.3(c). The amplitude of the oscillation depends on the square root of the frequency (dashed blue line) [25]. To study the relation between the parametric oscillation amplitude and the phase ϕ, the resonator is parametrically excited above the threshold. Figure 8.3(d) shows the amplitude of the oscillation when the direct drive and frequency is swept while varying the phase difference. Depending on the phase between the direct initiator

drive and the parametric excitation, constructive or destructive interference occurs which results in amplification or attenuation of the motion induced by the initiator signal. The maximum parametric amplification is found at a phase difference of $-\pi$ and π. The experiments described above clearly demonstrate the parametric behavior.

8.4 COUPLING BETWEEN PARAMETRIC AND DIRECT DRIVEN MODES

We now investigate the interactions between the different vibrational modes of the same mechanical resonator, when one of the modes is parametrically oscillating. This requires to monitor the response of one mode while another mode is parametrically excited. In particular, the modal interactions between the first and second mode are considered. First, we study the effect of the parametric oscillations of the first mode, characterized in the previous section, on the resonance frequency of the second mode. Figure 8.4(a) shows frequency responses of the second mode, when the first mode is parametrically pumped around its resonance frequency. The first mode is only parametrically pumped and no direct drive at the resonance frequency is applied. Below the resonance frequency of the first mode, no change in resonance frequency of the second mode is observed. Pumping at twice the resonance frequency, the first mode starts to oscillate parametrically. This oscillation induces a significant shift in resonance frequency of the second mode. By parametrically exciting the first mode, the resonance frequency of the second mode is tuned over more than 200 times the resonator linewidth. There is a linear relation of $f_{\mathrm{R},2}$ on $f_{\mathrm{pump},1}$ with sensitivity $f_{\mathrm{R},2}/f_{\mathrm{pump},1} = 1.4$ Hz/Hz.

The change in resonance frequency is explained as follows: the oscillation of the first mode increases the tension in the beam. This tension tunes the resonance frequency of the second mode to a higher value. A linear dependence between the two frequencies is expected, as in clamped-clamped beams the resonance frequency of one mode depends quadratically on the amplitude of the other mode [19], i.e. $f_{\mathrm{R},i} \sim |A_j|^2$ for modes i and j. The amplitude of the parametric oscillation depends on the square root of the pump frequency $|A_j| \sim \sqrt{f_{\mathrm{pump,j}}}$ [25], as experimentally verified in Fig. 8.3(c). Combining these two dependencies, one expects $f_{\mathrm{R},i} \sim f_{\mathrm{pump},j}$. This linear dependence is clearly observed in the measurements, see Fig. 8.4(a).

We have also studied the influence of the parametrically excited second mode on the resonance frequency of the first mode, i.e., the first mode is now probing the second mode, which is parametrically oscillating. Again, a linear dependence of the resonance frequency on the parametric pump frequency is found, as is shown

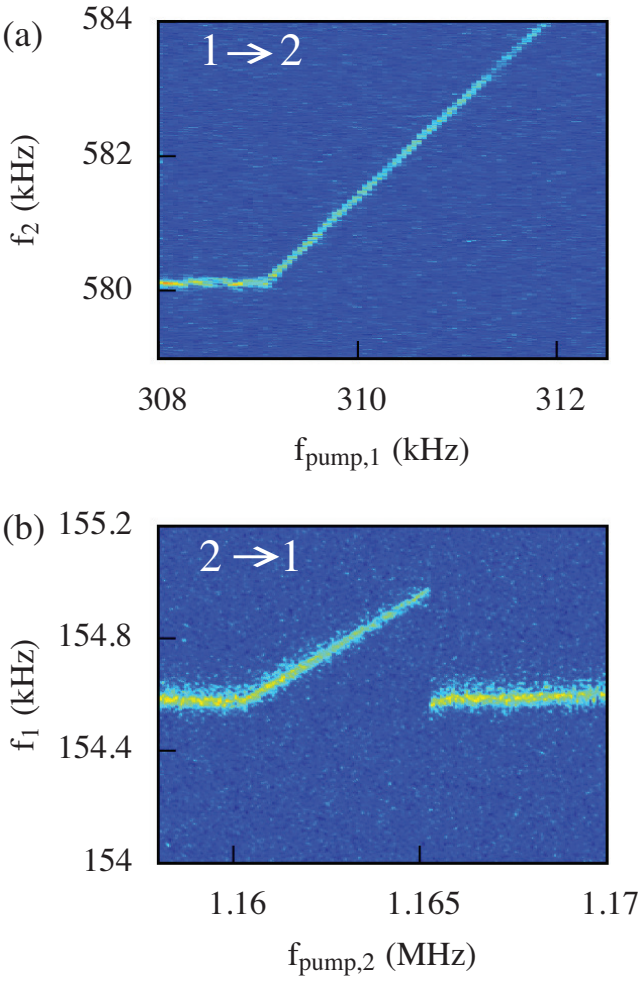

FIGURE 8.4: Interactions between a directly and parametrically driven mode. (a) Frequency responses of the second mode while varying pump frequency of the first mode. Color scale indicates the amplitude of the second mode. The linear dependence of $f_{R,1}$ on $f_{pump,2}$ is observed as explained in the text. (b) Reversed experiment; frequency responses of the first mode for varying the pump frequency of the second mode.

in Fig. 8.4(b). In this case, the sensitivity $f_{R,1}/f_{pump,2}$ = 79 mHz/Hz. As the pump frequency $f_{pump,2}$ is increased above 1.165 MHz the parametric oscillation disappears, and the resonance frequency of the first mode jumps back to its original value. At this point, the nonlinearity causes the oscillation of the second mode to jump to the low amplitude state, which is reflected by the sharp transition of the resonance frequency of the first mode. The large difference in sensitivity with the reversed experiment in Fig. 8.4(a) indicates that parametric pumping of the second mode is less effective to change the resonance frequency of the first mode than vice versa. This can be understood since the first mode has the largest oscillation amplitude and can provide the largest tension in the beam.

8.5 CONCLUSION

The interactions between a directly and a parametrically oscillating mode of the same mechanical resonator are studied. The parametric amplification and oscillations of a clamped-clamped resonator with an integrated piezoelectric transducer are investigated in detail. The dependence of the oscillation amplitude on pump frequency and phase difference are in agreement with theory. In this work, we demonstrate that the parametric oscillation of one mode induces a change in the resonance frequency of the other vibrational modes. This frequency change is proportional to the pump frequency, as is shown for the first and second mode. The sensitivity of the resonance shift of the second mode on the pump frequency of the first mode is found to be 1.4 Hz/Hz. When the experiment is reversed, i.e. the oscillating second mode is detected by a shift in resonance frequency of the first mode, the sensitivity is 79 mHz/Hz.

REFERENCES

[1] H. J. R. Westra, D. M. Karabacak, S. H. Brongersma, M. Crego-Calama, H. S. J. van der Zant, and W. J. Venstra, *Interactions between directly- and parametrically-driven vibration modes in a micromechanical resonator*, Phys. Rev. B **84**, 134305 (2011).

[2] B. Yurke, P. G. Kaminsky, R. E. Miller, E. A. Whittaker, A. D. Smith, A. H. Silver, and R. W. Simon, *Observation of 4.2-K equilibrium-noise squeezing via a Josephson-Parametric amplifier*, Phys. Rev. Lett. **60**, 9 (1988).

[3] V. Radeka and R. L. Chase, *A parametric radiation detector amplifier*, IEEE Trans. Nucl. Sci. **13**, 477 (1966).

[4] Y. Zhang, H. Wang, X. Li, J. Jing, C. Xie, and K. Peng, *Experimental generation*

of bright two-mode quadrature squeezed light from a narrow-band nondegenerate optical parametric amplifier, Phys. Rev. A **62**, 023816 (2000).

[5] M. E. Marhic, N. Kagi, T. K. Chiang, and L. G. Kazovsky, *Broadband fiber optical parametric amplifiers*, Optics Lett. **21**, 573 (1996).

[6] A. A. Savchenkov, A. B. Matsko, M. Mohageg, D. V. Strekalov, and L. Maleki, *Parametric oscillations in a whispering gallery resonator*, Optics Lett. **32**, 157 (2007).

[7] R. Lifshitz and M. Cross, *Response of parametrically driven nonlinear coupled oscillators with application to micromechanical and nanomechanical resonator arrays*, Phys. Rev. B **67**, 134302 (2003).

[8] R. B. Karabalin, R. Lifshitz, M. C. Cross, M. H. Matheny, S. C. Masmanidis, and M. L. Roukes, *Signal Amplification by Sensitive Control of Bifurcation Topology*, Phys. Rev. Lett. **106**, 094102 (2011).

[9] K. L. Turner, S. A. Miller, P. G. Hartwell, N. C. MacDonald, S. H. Strogatz, and S. G. Adams, *Five parametric resonances in a a microelectromechanical system*, Nature **396**, 149 (1998).

[10] M. Zalalutdinov, K. L. Aubin, M. Pandey, A. T. Zehnder, R. H. Rand, H. G. Craighead, and J. M. Parpia, *Frequency entrainment for micromechanical oscillator*, Appl. Phys. Lett. **83**, 3281 (2003).

[11] K. L. Ekinci and M. L. Roukes, *Nanoectromechanical systems*, Rev. Sci. Instrum. **76**, 061101 (2005).

[12] I. Mahboob and H. Yamaguchi, *Parametrically pumped ultrahigh Q electromechanical resonator*, Appl. Phys. Lett. **92**, 253109 (2008).

[13] J. Tamayo, *Study of the noise of micomechanical oscillators under quality factor enhancement via driving force control*, J. Appl. Phys. **97**, 044903 (2005).

[14] I. Mahboob and H. Yamaguchi, *Bit storage and bit flip operations in an electromechanical oscillator*, Nature Nanotech. **3**, 275 (2008).

[15] I. Mahboob, E. Flurin, K. Nishiguchi, A. Fujiwara, and H. Yamaguchi, *Interconnect-free parallel logic circuits in a single mechanical resonators*, Nat. Commun. **2**, 198 (2011).

[16] J. Suh, M. D. LaHaye, P. M. Echternach, K. C. Schwab, and M. L. Roukes, *Parametric amplification and back-action noise squeezing by a qubit-coupled nanoresonator*, Nano Lett. **10**, 3990 (2010).

[17] A. Eichler, J. Chaste, J. Moser, and A. Bachtold, *Parametric Amplification and Self-Oscillation in a Nanotube Mechanical Resonator*, Nano Lett. **7**, 2699 (2011).

[18] R. B. Karabalin, M. C. Cross, and M. L. Roukes, *Nonlinear dynamics and chaos in two coupled nanomechanical resonators*, Phys. Rev. B **79**, 165309 (2009).

[19] H. J. R. Westra, M. Poot, H. S. J. van der Zant, and W. J. Venstra, *Nonlinear modal interactions in clamped-clamped mechanical resonators*, Phys. Rev. Lett. **105**, 117205 (2010).

[20] T. Dunn, J.-S. Wenzler, and P. Mohanty, *Anharmonic modal coupling in a bulk micromechanical resonator*, Appl. Phys. Lett. **97**, 123109 (2010).

[21] I. Mahboob, Q. Wilmart, K. Nishiguchi, A. Fujiwara, and H. Yamaguchi, *Wideband idler generation in a GaAs electromechanical resonator*, Phys. Rev. B **84**, 113411 (2011).

[22] W. J. Venstra, H. J. R. Westra, and H. S. J. van der Zant, *Q-factor control of a microcantilever by mechanical sideband excitation*, Appl. Phys. Lett. **99**, 151904 (2011).

[23] D. M. Karabacak, S. H. Brongersma, and M. Crego-Calama, *Enhanced sensitivity volatile detection with low power integrated micromechanical resonators*, Lab Chip **10**, 1976 (2010).

[24] W. Zhang, R. Baskaran, and K. L. Turner, *Effect of cubic nonlinearity on autoparametrically amplified resonant MEMS mass sensor*, Sens. and Actuators A **102**, 139 (2002).

[25] R. Lifshitz and M. C. Cross, *Nonlinear dynamics of nanomechanical and micromechanical resonators* (Wiley, Meinheim, 2008), vol. 1, chap. 1, pp. 1–52.

[26] D. Rugar and P. Grütter, *Mechanical parametric amplification and thermomechanical noise squeezing*, Phys. Rev. Lett. **67**, 699 (1991).

A

THEORY OF CANTILEVER MODAL INTERACTIONS

In this appendix the nonlinear equations of motion of the modes in a cantilever are described. We start with the general equations of motion, which include the coupling between the torsional and flexural modes. Then, we consider flexural modes along one axis. We conclude with the equation of motion of two coupled flexural modes, relevant to the experiment in Chapter 6. We start with the equations derived by Crespo da Silva [1, 2], who described the motion in two flexural directions v and w and the torsional angle θ:

A

$$
\begin{aligned}
m v_{tt} + \gamma^v v_t + \frac{\partial^2}{\partial s^2}(D_\zeta v_{ss}) = \frac{\partial}{\partial s}\Big\{ & - D_\xi w_{ss}(\theta_s + v_{ss} w_s) + w_s Q_\theta \\
& - v_s \frac{\partial}{\partial s}\Big[D_\zeta (v_s v_{ss} + w_s w_{ss})\Big] + (D_\eta - D_\zeta) w_s v_{ss} w_{ss} \\
& + \Big[\Big(D_\eta - D_\zeta\Big)\frac{\partial}{\partial s}\Big(\theta w_{ss} - \theta^2 v_{ss}\Big)\Big] + J_\xi w_{st}(\theta_t + v_{st} w_s) \\
& + J_\zeta v_{st}\frac{\partial}{\partial t}\Big(v_s v_{st} + w_{st} w_s\Big) - \frac{\partial}{\partial t}\Big[(J_\eta - J_\zeta)(\theta w_{st} \\
& - \theta^2 v_{st} + w_s v_{st} w_{st}) - J_\zeta v_{st}\Big] - \frac{v_s}{2}\int_L^s \mathrm{d}s'\, m \int_0^{s'} \mathrm{d}s''\, \frac{\partial^2}{\partial t^2}\Big(v_s^2 + w_s^2\Big)\Big\} \\
& + q\cos(\Omega t), \qquad \text{(A.1)}
\end{aligned}
$$

$$
\begin{aligned}
m w_{tt} + \gamma^q w_t + \frac{\partial^2}{\partial s^2}(D_\eta w_{ss}) = \frac{\partial}{\partial s}\Big\{ & D_\xi v_{ss}(\theta_s + v_{ss} w_s) \\
& - w_s \frac{\partial}{\partial s}\Big[D_\eta (v_s v_{ss} + w_s w_{ss})\Big] + \Big[\Big(D_\eta - D_\zeta\Big)\frac{\partial}{\partial s}\Big(\theta v_{ss} + \theta^2 w_{ss}\Big)\Big] \\
& - J_\xi v_{st}(\theta_t + v_{st} w_s) + w_s \frac{\partial}{\partial t}(J_\eta w_s w_{st} + J_\zeta v_s v_{st}) \\
& - \frac{\partial}{\partial t}\Big[(J_\eta - J_\zeta)(\theta v_{st} + \theta^2 w_{st}) - J_\eta w_{st}\Big] \\
& - \frac{w_s}{2}\int_L^s \mathrm{d}s'\, m \int_0^{s'} \mathrm{d}s''\, \frac{\partial^2}{\partial t^2}\Big(v_s^2 + w_s^2\Big)\Big\}, \qquad \text{(A.2)}
\end{aligned}
$$

$$
\begin{aligned}
& J_\xi \frac{\partial}{\partial t}\Big(\theta_t + v_{st} w_s\Big) - \frac{\partial}{\partial s}\Big[D_\xi(\theta_s + v_{ss} w_s)\Big] + (D_\eta - D_\zeta)\Big[(v_{ss}^2 - w_{ss}^2)\theta - v_{ss} w_{ss}\Big] \\
& \quad - (J_\eta - J_\zeta)\Big[(v_{st}^2 - w_{st}^2)\theta - v_{st} w_{st}\Big] = Q_\theta. \qquad \text{(A.3)}
\end{aligned}
$$

Here, the subscripts s and t denote differentiating to position and time respectively. ξ, η and ζ represent the principal axes of the beam's cross section. γ and Q_θ represents the damping, $D_{\eta,\zeta}$ are the flexural stiffnesses of the beam and D_ξ is the torsional stiffness. The moments of inertia are given by $J_{\eta,\zeta,\xi}$. The driving force is q with driving frequency Ω.

Now, we consider only vibrations in one direction, so the Eq. A.2 and all terms with w in Eqs. A.1 and A.3 are disregarded. For the torsional mode, the nonlinear effect of torsion warping is taken into account [3], where we assume that the ends of the beam are axially immovable. The coupled differential equations (in non-dimensional form, notation from Ref. [4]) are now given by

$$
\begin{aligned}
&v_{tt} + \gamma^v v_t + \beta_y v_{ssss} = \frac{\partial}{\partial s}\Big\{ - v_s \frac{\partial}{\partial s}\Big(\beta_y v_s v_{ss}\Big) - \frac{\partial}{\partial s}\Big[(1-\beta_y)\theta^2 v_{ss}\Big] \\
&\quad + J_\zeta v_s \frac{\partial}{\partial t}\Big(v_s v_{st}\Big) - \frac{\partial}{\partial t}\Big[\Big(J_\zeta - J_\eta\Big)\theta^2 v_{st} + J_\zeta v_{st}\Big] \\
&\quad - \frac{v_s}{2}\int_1^s \mathrm{d}s' \, m \int_0^{s'} \mathrm{d}s'' \, \frac{\partial^2}{\partial t^2}\Big(v_s^2\Big)\Big\} + q\cos(\Omega t), \qquad \text{(A.4)} \\
&J_\xi \theta_{tt} - J_\xi \gamma^\theta \theta_t + \Big(\beta_\theta + \frac{I_t}{AD_\eta L^2}\tilde{N}\Big)\theta_{ss} - \frac{\rho C_s D_\eta}{\sqrt{m} L^4}\theta_{sstt} + \frac{EC_s}{L^4}\theta_{ssss} - \beta_z \theta_s^2 \theta_{ss} \\
&\quad - (1-\beta_y) v_{ss}^2 \theta + (J_\eta - J_\zeta) v_{st}^2 \theta = 0. \qquad \text{(A.5)}
\end{aligned}
$$

β_y and β_θ are the ratios between two stiffnesses ($\beta_y = D_\zeta / D_\eta$ and $\beta_\theta = D_\xi / D_\eta$) and A is the cross sectional area. The torsion nonlinearity is written as $\beta_z = \frac{3}{2L^3} E I_n$. The torsion constant I_t, the warping constant C_S and the time-dependent tensile axial load $\tilde{N}$ are given by

$$
\begin{aligned}
I_t &= \int_S \Big(y^2 + z_y^2 \frac{\partial \phi_S^P}{\partial z} - z \frac{\partial \phi_S^P}{\partial y}\Big)\mathrm{d}S, \\
C_S &= \int_S (\phi_S^P)^2 \mathrm{d}S, \\
\tilde{N} &= \frac{1}{2}\frac{EI_p}{l}\int_0^l (\theta_x')^2 \mathrm{d}x. \qquad \text{(A.6)}
\end{aligned}
$$

Here, S is the solid angle and ϕ_S^P is the primary warping function. A more detailed description of the nonlinearity in the torsional mode is found in Ref. [3].

To demonstrate the origin of the nonlinear interactions observed in the main text, we now simplify the coupled equations Eq. A.4 and A.5 by applying the Galerkin procedure. The solutions are then written as a linear combination of the linear mode shapes of the cantilever with coefficients, which correspond to the time-dependent vibration, $v = \sum_i F_i^v(s) v_i(t)$ and $\theta = \sum_i F_i^\theta \theta_i(t)$, where i represents the mode number. The mode shapes of the flexural and torsional modes of the cantilever will be discussed. Introducing the operator $\mathscr{L}$, the linear part of Eq. A.2 is written as

$$
\mathscr{L}[F^v] = \beta_y \frac{\partial^4 F^v}{\partial t^4} + J_\zeta \omega^2 F^v = \omega^2 F^v \qquad \text{(A.7)}
$$

The resonance frequency is denoted as ω. The eigenfunctions can be calculated together with the boundary conditions for a single-clamped cantilever $F^v(0) = F_s^v =$

A

$F_s^v s(1) = F_{sss}^v = 0$ as

$$F = [\cosh(k_1 s) - \cos(k_2 s) - K(\sinh(k_1 s) - k_1/k_2 \sin(k_2 s)],$$
$$K = \frac{k_1^2 \cosh(k_1) + k_2^2 \cos(k_2)}{k_1^1 \sinh(k_1) + k_1 k_2 \sin(k_2)}, \tag{A.8}$$

The values of $k_{1,2}$ are given by

$$k_{1,2} = \sqrt{\mp \frac{J\zeta \omega_B^2}{2\beta_y} + \sqrt{\left(\frac{J\zeta \omega_B^2}{2\beta_y}\right)^2 + \frac{\omega_B^2}{\beta_y}}}. \tag{A.9}$$

The values of k_1 and k_2 depend on the mode number i and can be calculated via the generating function

$$k_1^4 + k_2^4 + 2k_1^2 k_2^2 \cosh(k_1)\cos(k_2) + k_1 k_2 (k_2 - k_1)^2 \sinh(k_1) sin(k_2) = 0 \tag{A.10}$$

The dimensional resonance frequency of the flexural mode is given by

$$\omega_{B,i} = \kappa_i (h/L^2)\sqrt{D_\zeta / J_\zeta}, \tag{A.11}$$

where κ_i is 1.875, 4.695 and 7.855 for $i = 1$, 2 and 3. The beam shape of the first two flexural modes are shown in the inset of Fig. 6.1.

The torsional mode shapes can be calculated by considering the operator $\mathscr{M}$ with eigenvalues ω_T

$$\mathscr{M}[G] = \frac{\beta_\xi}{J_\xi}\frac{\partial^2 F^\theta}{\partial t^2} = \omega_T^2 G, \tag{A.12}$$

and the corresponding boundary conditions of $F^\theta(0) = F_s^\theta(1) = 0$. Inserting the boundary conditions in Eq. A.12, gives the equation for the torsional mode shapes: $G = \sin[(2i-1)\pi/2s]$. The resonance frequency of the torsion mode is given by $\omega_T = (2i-1)(\pi/2)\sqrt{\beta_\xi / J_\xi}$.

The Galerkin procedure is applied to Eq. A.4 and A.5: i.e. the solutions are written as a linear combination of the eigenmodes. We assume that the flexural mode is only excited around the resonance frequency, accumulating in the equations

$$v_{tt}^i + \gamma^v v_t^i + \omega_F^2 v^i = \sum_j \sum_k \sum_l \left(v^j \left[\alpha_{1,ijkl} \theta^k \theta^l + \alpha_{2,ijkl} v^k v^l + \alpha_{3,ijkl} (v^k v^l)_{tt} \right] \right) + f^i \cos(\Omega t),$$
$$\theta_{tt}^i + \gamma^\theta + \omega_T^2 \theta^i = \sum_j \sum_k \sum_l \left(\theta^j \left[\alpha_{4,ijkl} v^k v^l + \alpha_{5,ijkl} \theta^k \theta^l \right] \right). \tag{A.13}$$

$ijkl$	α_1	α_2	α_3	α_4	α_5
1111	3.2134406	40.440663	4.5967725	14.719963	-0.019637282
2222	317.75980	13418.093	144.72550	45.800677	-12.216122
1211	-25.807810	-102.31961	-3.5959704	-2.1072118	-0.055456733
1121	5.1993367	65.862059	-3.5959704	-45.970529	-0.055456733
1122	10.839314	172.73779	25.174152	74.665735	-1.4684083
1221	-20.397232	228.01790	6.1173662	22.425710	-0.15672902
1212	-20.397232	2083.8457	6.1173662	22.425710	-1.4684083
2111	-25.807803	-102.31961	-3.5959704	-2.1072118	-0.057760141
2211	395.65715	172.73767	25.174152	11.080629	-0.16315647
2121	-20.397243	228.01790	6.1173661	22.425710	-0.16315647
2112	-20.397243	2083.8456	6.1173661	22.425710	-1.52915110

TABLE A.1: The values of the integrals in the coefficients α for the interactions between the first and second flexural and torsional modes.

The above equations show that the nonlinearity is the origin of the modal interactions. Note that for $j = k = l$, the nonlinear equation describing one mode of the cantilever is found. A quadratic coupling is present between two different vibrational modes (for example $k = l$) also follows directly from the cubic nonlinearities. This quadratic coupling is clearly observed in the experiments. In Eq. A.13, the terms linear in θ are assumed to only modify the resonance frequency ω_T. The coupling (Galerkin) coefficients α are given by the following equations:

$$
\begin{aligned}
\alpha_{1,ijkl} &= -(1-\beta_y)\int_0^1 F^i (F^j_{ss} G^k G^l)_{ss} \mathrm{d}s, \\
\alpha_{2,ijkl} &= -\beta_y \int_0^1 F^i [F^j_s (F^k_s F^l_{ss})_s]_s \mathrm{d}s, \\
\alpha_{3,ijkl} &= -\frac{1}{2}\int_0^1 F^i \Big(F^j_s \int_1^{s''} \int_0^{s'} F^k_s F^l_s \mathrm{d}s \mathrm{d}s' \Big)_{s''} \mathrm{d}s'', \\
\alpha_{4,ijkl} &= \frac{-(1-\beta_y)}{J\xi} \int_0^1 G^i G^j (F^k F^l)_{ss} \mathrm{d}s, \\
\alpha_{5,ijkl} &= \beta_z \int_0^1 G^i (G^j_s G^k_s) G^l_{ss} \mathrm{d}s.
\end{aligned}
\tag{A.14}
$$

Considering the interactions only between the lowest two modes of the torsional and the flexural mode, the values of the integrals in the coefficients α are given in Table A.1.

A

To give an example, we work out Eq. A.13 for the fundamental and second flexural mode of a cantilever. We denote the amplitudes with $v^1 = a$ and $v^2 = b$) and the coupled equations are given by

$$\begin{aligned} a_{tt} + \gamma_1 a_t + \omega_F^2 a &= \alpha_{2,1111} a^3 + \alpha_{2,1222} b^3 + (\alpha_{2,1112} + \alpha_{2,1121} + \alpha_{2,1211}) a^2 b \\ &+ (\alpha_{2,1212} + \alpha_{2,1221} + \alpha_{2,1122}) b^2 a + \alpha_{3,1111} 2a(a^2)_{tt} + \alpha_{3,1222} 2b(b^2)_{tt} \\ &+ (\alpha_{3,1112} + \alpha_{3,1121}) a(ab)_{tt} + (\alpha_{3,1221} + \alpha_{3,1212}) b(ab)_{tt} + \alpha_{3,1211} b(a^2)_{tt} \\ &+ \alpha_{3,1122} a(b^2)_{tt} + f_1 \cos(\Omega t), \end{aligned} \tag{A.15}$$

$$\begin{aligned} b_{tt} + \gamma_2 b_t + \omega_F^2 b &= \alpha_{2,2111} a^3 + \alpha_{2,2222} b^3 + (\alpha_{2,2112} + \alpha_{2,2121} + \alpha_{2,2211}) a^2 b \\ &+ (\alpha_{2,2212} + \alpha_{2,2221} + \alpha_{2,2122}) b^2 a + \alpha_{3,2111} 2a(a^2)_{tt} + \alpha_{3,2222} 2b(b^2)_{tt} \\ &+ (\alpha_{3,2112} + \alpha_{3,2121}) a(ab)_{tt} + (\alpha_{3,2221} + \alpha_{3,2212}) b(ab)_{tt} + \alpha_{3,2211} b(a^2)_{tt} \\ &+ \alpha_{3,2122} a(b^2)_{tt} + f_2 \cos(\Omega t). \end{aligned} \tag{A.16}$$

REFERENCES

[1] M. R. M. Crespo da Silva and C. C. Glynn, *Nonlinear Flexural-Flexural-Torsional Dynamics of Inextensional Beams. I. Equations of motion*, J. Struct. Mech. **6**, 437 (1978).

[2] M. R. M. Crespo da Silva and C. C. Glynn, *Nonlinear Flexural-Flexural-Torsional Dynamics of Inextensional Beams. II. Forced Motions*, J. Struct. Mech. **6**, 449 (1978).

[3] E. Sapountzakis and V. Tsipiras, *Nonlinear nonuniform torsional vibrations of bars by the boundary element method*, Journal of Sound and Vibration **329**, 1853 (2010), ISSN 0022-460X.

[4] M. R. M. Crespo da Silva, *Nonlinear flexural-flexural-torsional interactions in beams including the effect of torsional dynamics. II: Combination resonance*, Nonlinear Dynamics **5**, 161 (1994).

SUMMARY

In this Thesis, nonlinear dynamics and nonlinear interactions are studied from a micromechanical point of view. Single and doubly clamped beams are used as model systems where nonlinearity plays an important role. The nonlinearity also gives rise to rich dynamic behavior with phenomena like bifurcations, stochastic switching and amplitude-dependent resonance frequencies.

The theoretical background of micromechanical systems involving the relevant nonlinearities for beams clamped on one (cantilever) or two sides (clamped-clamped beam) are discussed in chapter 2. First, the linear response of a mechanical resonator is discussed. Then, the linear equations are extended with nonlinear terms accounting for geometric and inertial effects. Specifically, the origin of the Duffing nonlinearity in the equation of motion of a clamped-clamped beam is shown. It is shown that the nonlinearity couples the flexural vibration modes of a beam.

Microcantilevers are widely used in mass sensing and force microscopy. At small resonance amplitudes, cantilever motion is described by a harmonic oscillator model, while at high amplitudes, the motions is limited by nonlinearities. In chapter 3, the intrinsic mechanical nonlinearity in microcantilevers is studied. It is shown that although the origin is different, the nonlinearity resembles a Duffing nonlinearity resulting in hysteresis and bistable amplitudes. This bistability is then used to implement a mechanical memory.

The bistability of microcantilevers can also be used to study the switching characteristics when noise is applied. Chapter 4 shows the experimental implementation of this stochastic switching of microcantilever motion. It is shown that upon increasing the noise intensity, the switching rate rises exponentially as expected from Kramer's law. However, at higher noise intensities, the switching rate saturates and eventually even decreases, which suggests that the noise influences the dynamical parameters of the system.

In chapter 5, we investigate in detail the coupling between the flexural vibration modes of a clamped-clamped beam. The coupling arises from the displacement-induced tension. A theoretical model based on the nonlinearity is developed, which is experimentally verified by driving two modes of the beam at high amplitudes and reading out their motion at the two frequencies. The experiments show that the resonance frequency of one flexural mode depends on the amplitude of an-

other flexural mode and the theory is in excellent agreement with the experiments.

The nonlinearity not only couples the flexural modes in a clamped-clamped beam, but we show in chapter 6 that also the cantilever modes are coupled. Here, the mechanism causing the nonlinearity is different, as there is no displacement-induced tension. The microcantilever is driven using a piezo actuator and its motion is read out using an optical setup. At high vibration amplitudes, the resonance frequency of one mode depends on the amplitude of the other modes. The torsional modes also show nonlinear behavior as evidenced by a frequency stiffening of the response.

The modal interactions in a microcantilever can also be used in a all-mechanical analogue of a cavity-optomechanics, where one mode is used as a cavity mode, which influences the probe mode. In chapter 7, we show that by exciting at the sum and difference frequencies of the two modes, the Q factor of the probe mode could be suppressed over a wide range.

In chapter 8, the interaction between a directly- and parameterically-driven resonance mode is studied. Parametric driving means that the spring constant of the beams is modulated at twice the resonance frequency. Clamped-clamped beams with an integrated piezo-actuator on top, designed for applications as gas sensors, are used in the experiments. First, the parametric amplification and oscillation of the beam is studied, then the motion of a parametrically-driven mode is detected by a change in resonance frequency of the directly-driven mode. There is a linear dependence of the oscillation frequency of the parametrically-driven mode and the resonance frequency of the directly-driven mode. A potential application as a linear frequency converter is suggested.

SAMENVATTING

In dit proefschrift worden niet-lineaire dynamica en niet-lineaire interacties bestudeerd vanaf een micro-mechanisch standpunt. Enkel en dubbel ingeklemde balken worden gebruikt als model systemen waar de niet-lineariteit een belangrijke rol speelt. De niet-lineariteit leidt tot rijk dynamisch gedrag met fenomenen zoals vertakkingen, stochastische schakelingen en amplitude-afhankelijke resonantie frequenties.

De theoretische achtergrond van micromechanische systemen met betrekking tot de relevante niet-lineariteiten voor eenzijdig (cantilever) en tweezijdig ingeklemde balken wordt gegeven in hoofdstuk 2. Eerst wordt de lineaire respons van een mechanische resonator bediscussieerd. Daarna worden de lineaire vergelijkingen uitgebreid niet-lineaire termen die rekening houden met geometrische en inertiële effecten. Meer specifiek wordt de oorsprong van de Duffing niet-lineariteit in de bewegingsvergelijking van een dubbel ingeklemde balk aangetoond. Er wordt aangetoond dat de niet-lineariteit de buig-trillingsmodi van een balk koppelt met elkaar.

Microcantilevers worden breed gebruikt in massa sensoren en kracht microscopie. Bij kleine resonantie amplitudes wordt de cantilever beweging beschreven door een harmonische oscillator, terwijl bij hoge amplitudes de beweging word beperkt door niet-lineariteiten. In hoofdstuk 3 wordt de intrinsieke mechanische niet-lineariteit in microcantilevers bestudeerd. Er wordt aangetoond dat, hoewel de oorsprong anders is, de niet-lineariteit lijkt op een een Duffing niet-lineariteit wat resulteert in hysterese en bistabiele amplitudes. De bistabiliteit wordt dan gebruikt om een mechanisch geheugen te implementeren.

De bistabiliteit van microcantilevers kan ook gebruikt worden om de schakel karakteristieken te bestuderen als er ruis wordt aangeboden. Hoofdstuk 4 laat de experimentele implementatie van dit stochastische schakelen van de beweging van een microcantilever zien. Er wordt aangetoond dat als de ruis intensiteit wordt opgeschroefd, de schakelsnelheid exponentieel toeneemt zoals verwacht wordt volgens de wet van Kramer. Echter, voor hogere intensiteiten verzadigd de schakelsnelheid en neemt uiteindelijk af. Dit suggereert dat de ruis de dynamische parameters van het systeem beïnvloedt.

In hoofdstuk 5 laten we in detail de koppeling tussen de buig-trillingsmodi van een dubbel-ingeklemde balk zien. De koppeling komt voort uit de uitwijking geïn-

duceerde spanning. Een theoretisch model gebaseerd op de niet-lineariteit is ontwikkeld, welke experimenteel geverifieerd is door twee modi van de balk op hoge amplitudes aan te drijven en hun beweging uit te lezen op meerdere frequenties. De experimenten laten zien dat de resonantie frequentie van een buig-modus afhangt van de amplitude van een andere buig-modus en de theorie komt zeer goed overeen met de experimenten.

De niet-lineariteit koppelt niet alleen de buig-modi in een dubbel-ingeklemde balk, maar we laten in hoofdstuk 6 zien dat de niet-lineariteit ook de cantilever modi koppelt. Hier is het mechanisme dat de niet-lineariteit koppelt anders, omdat er geen uitwijking-geïnduceerde spanning is. De microcantilever wordt aangedreven met een piezo-actuator en de beweging wordt uitgelezen met behulp van een optische opstelling. Bij hoge trillings-amplitudes hangt de resonantie frequentie af van de amplitude van een ander modus. De torsie modi laten ook niet-lineair gedrag zien wat blijkt uit een frequentie verstijving van de response.

De interactie tussen de modi in een microcantilever kan ook gebruikt worden in een mechanische analoog van cavity-optomechanica. waar een modus gebruikt wordt als een cavity modus welke de onderzoeks-modus beïnvloedt. In hoofdstuk 7 laten we zien door op de som en verschil frequenties van de twee modi aan te drijven, de Q factor van de onderzoeks-modus over een groot gebied onderdrukt kan worden.

In het laatste hoofdstuk 8 bestuderen we de interactie tussen een direct een een parametrisch aangedreven resonantie modus. Parametrisch aandrijven betekent dat de veerconstante van de balk wordt gemoduleerd met twee keer de resonantie frequentie. Dubbel-ingeklemde balken met een geïntegreerde piezo-actuator bovenop worden gebruikt in de experimenten. Deze zijn ontworpen voor toepassingen als gas-sensoren. Eerst wordt de parametrische versterking en oscillatie van de balk bestudeerd. Daarna is de beweging van de parameterisch aangedreven modus gedetecteerd door een verandering in de resonantie frequentie van de direct aangedreven modus. Er is een lineaire afhankelijkheid van de oscillatie frequentie van de parametrisch aangedreven modus en de resonantie frequentie van de direct aangedreven modus. Als toepassing wordt een lineaire frequentie omzetter voorgesteld.

CURRICULUM VITÆ

Hidde WESTRA

09-09-1983 Born in Assen, the Netherlands.

EDUCATION

1987–1995 Primary School
Jan Ligthart school, Borne

1995–2001 Secondary School (Gymnasium)
Bataafse Kamp, Hengelo

2001–2005 BSc. in Applied Physics
Delft University of Technology

2005–2008 MSc. in Applied Physics
Delft University of Technology
Thesis: Modeling vibrational modes in molecular quantum dots
Supervisor: Prof. H. S. J. van der Zant

2008-2012 PhD in Applied Physics
Delft University of Technology
Thesis: Nonlinear beam mechanics
Promotor: Prof. H. S. J. van der Zant

LIST OF PUBLICATIONS

11. W. J. Venstra, **H. J. R. Westra**, and H. S. J. van der Zant *Stochastic switching of cantilever motion*, *submitted*

10. **H. J. R. Westra**, H. S. J. van der Zant, and W. J. Venstra, *Modal interactions of flexural and torsional vibrations in a microcantilever*, Ultramicroscopy **120**, 41–47 (2012)

9. W. J. Venstra, **H. J. R. Westra**, and H. S. J. van der Zant *Q-factor control of a microcantilever by mechanical sideband excitation*, Appl. Phys. Lett. **99**, 151904 (2011)

8. **H. J. R. Westra**, D. M. Karabacak, S. H. Brongersma, M. Crego-Calama, H. S. J. van der Zant, and W. J. Venstra *Interactions between directly- and parametrically-driven vibration modes in a micromechanical resonator*, Phys. Rev. B **84**, 134305 (2011)

7. W. J. Venstra, **H. J. R. Westra**, and H. S. J. van der Zant *Dynamics of immersed clamped-clamped microresonators* Sensors, 2010 IEEE, 2005 (2010)

6. **H. J. R. Westra**, M. Poot, H. S. J. van der Zant, and W. J. Venstra, *Detecting the motion of a microresonator via mode-mode interaction* Sensors, 2010 IEEE, 1047 (2010)

5. W. J. Venstra, **H. J. R. Westra**, and H. S. J. van der Zant *Mechanical stiffening, bistability, and bit operations in a microcantilever* Appl. Phys. Lett. **97**, 193107 (2010)

4. **H. J. R. Westra**, M. Poot, H. S. J. van der Zant, and W. J. Venstra *Nonlinear modal interactions in clamped-clamped mechanical resonators*, Phys. Rev. Lett. **105**, 117205 (2010)

3. W. J. Venstra, **H. J. R. Westra**, K. Babaei Gavan, and H. S. J. van der Zant *Magnetomotive drive and detection of clamped-clamped mechanical resonators in water*, Appl. Phys. Lett. **95**, 263103 (2009)

2. K. Babaei Gavan, **H. J. R. Westra**, E. W. J. M. van der Drift, W. J. Venstra, and H. S. J. van der Zant *Size-dependent effective Young's modulus of silicon nitride cantilevers*, Appl. Phys. Lett. **94**, 233108 (2009).

1. K. Babaei Gavan, **H. J. R. Westra**, E. W. J. M. van der Drift, W. J. Venstra, and H. S. J. van der Zant *Impact of fabrication technology on flexural resonances of silicon nitride cantilevers*, Microelectron. Eng. **86**, 1216 (2009)

ACKNOWLEDGEMENTS

In these final pages of this Thesis, I want to acknowledge the people who helped me make this possible. Four years of hard work and the help of a lot of people resulted in this little booklet.

My first contact with Herre and his group was when I was looking for a masters project. This was in the days I still wanted to do theory and I ended up doing a project where I learned both sides of the group: the molecular electronics and the carbon nanotube mechanics. After I finished, I decided I wanted to continue in a PhD track, but this time I also wanted to do some experimental work and contacted Herre again. He had an open position in top-down NEMS, where I could both fabricate and measure my own devices and still do some theory. Herre, I want to thank you for letting me find my own path in this project. I also really appreciated the corrected manuscripts I found on early Monday mornings, while I only gave them to you the Friday before late in the afternoon.

In the beginning, I received a lot of help of Gijs, whose project I would continue and from him I learned how to perform the experiments. When Gijs graduated, I started to work more with Warner, which led to a collaboration, which would last my entire PhD. All the work described in this Thesis would not have been possible without you. I think our never-ending discussions, writing sessions and coffee breaks really attributed to the quality of the work. I admire your creativity and drive to really look way behind the comma. Especially, the conference trip to Hawaii we did together is something I will never forget.

I also want to thank Menno, my advisor during my masters project, but you also helped me a lot during my PhD. I think you are one of the smartest people I ever met. I am sure you will succeed in your academic career. From Eindhoven, I received support from the Holst Centre: they saved me a lot of time by fabricating devices and discussing my project. Thank you Devrez, Mercedes and Sywert. I would like to thank the clean room staff for helping me with the devices I fabricated myself, Patrick, Emile, Marco, thanks! I also want to thank the members of the theory group for useful discussions, in particular Giorgi, Francois, Ciprian and Yaroslav. I want to thank Masha and Ron for helping me improve the setup, for teaching me the noble art of wire-bonding and of course the coffee and tea breaks. For my computer related problems, I could always count on Jos. Thanks for letting me do my calculations on your precious machine. The administrative support I

received during the years came from Irma, Monique en Maria. Thank you for everything.

I had a great time in the MED group, but this would not have been the case if it wasn't for the people. I want to thank Benoit, Jos, Ronald en Carlos for letting office F394 a nice place to work in. From the early days, I remember Edgar and his practical jokes, but also Andreas the linux man, Christian the German, Bo and his membanes, Anne, Abdulaziz, Alexander and the colorful Diana.

And there was the party duo Samir and Ferry, with whom I still remember the nights in the city and visits to the Kurk. Samir, I think you are responsible for half of the data ever generated by the group. I admire your ability to change your biorhythm and measure every night for a month. I wish you all the best with finding your next goals. Ferry, thanks for showing me Boston, I really enjoyed my time there. You are finally turning into a real physicist.

During the past years, more people arrived in the group. One of the first were the tube-boys Ben and Harold. Thanks Harold for putting the science in perspective and your everlasting optimism. I also want to thank Michele for teaching me the italian gestures. As the group expanded, two new PI's joined our efforts. I want to wish Sander and Gary the very best with their little groups. All (former) members of MED have contributed to the relaxed working environment and special thanks to Andres (next tapas party I will definitely attend), Venkatesh, Mickael, Enrique, Anna, Sal, Vibhor, Ben B., Ricardo and all the students from the past years.

Als laatste wil ik mijn familie en vrienden bedanken. De mannen van CΠΥΤΗΝΚ voor de nodige ontspanning in de vorm van de biertjes op het terras, etentjes en wintersportvakanties; de dames en heren van 't Vatt voor de weekendjes weg; de mannen van Heren 10 en 6 van Hudito voor het balletje slaan op zondag en mijn huisgenoten Henk-Jan, Andries, Frank en Matthias. Verder wil ik mijn ouders Ineke en Willem, zusjes Anne-Maayke en Lisette, broertje Jelmer (top dat je me bij wil staan tijdens mijn verdediging) en Hanna bedanken voor de support. De laatste woorden zijn voor mijn vriendinnetje Charlotte, bedankt voor je steun!

Hidde Westra
Delft, October 2012